

NMDA RECEPTOR TRANSMEMBRANE DOMAIN:
STRUCTURE AND DIVALENT ION SELECTIVITY

A DISSERTATION SUBMITTED IN PARTIAL FULFILLMENT OF THE REQUIREMENTS

FOR THE DEGREE OF

DOCTOR OF PHILOSOPHY

IN

CHEMISTRY

BY

LEA VERAS

DEPARTMENT OF CHEMISTRY
CARNEGIE MELLON UNIVERSITY
PITTSBURGH, PA 15213



May 2014

Lea Veras: *NMDA Receptor Transmembrane Domain: Structure and Divalent Ion Selectivity,*

© May 2014

All rights reserved

ADVISED BY:

Maria Kurnikova

THESIS COMMITTEE MEMBERS:

Jon Johnson

David Yaron

Hyung Kim

Pei Tang

Dedicated to the person who taught me to always think beyond, my
grandfather vô Zé Maciel.

ABSTRACT

During a synaptic signal, NMDA receptors are the only ionotropic glutamate receptor subfamily that besides glutamate require glycine and membrane depolarization to allow ion permeation. The depolarization is necessary to release Mg^{2+} of the channel of NMDA receptors. Of the ions that permeate these ion channels, Ca^{2+} is of importance because it is essential for learning and memory. Furthermore, NMDA receptor dysfunction has been associated with several nervous system disorders, and thus understanding NMDA receptor functions and dysfunctions are relevant for rational drug design.

The mechanisms by which NMDA receptors select Ca^{2+} for permeation over all other physiological ions, while binding Mg^{2+} and restricting other ions' permeation, are not well understood. We hypothesize that the slightly different atomic properties of Mg^{2+} and Ca^{2+} result in different mechanisms for how each divalent ion moves across the channel.

To create a more complete picture of the permeation mechanism and prove our hypothesis, we performed a multi-level computational chemistry approach. Our research methods consisted of three main steps. The first step was to perform quantum chemical and molecular dynamic calculations to quantitatively predict ion interactions with solvents that mimic the heterogeneous environment of the protein. The second step consisted of modeling, refining, and equilibrating a homology model of the NMDA receptor transmembrane domain. The final step consisted of using the equilibrated transmembrane domain NMDA

receptor model to study the actual ionic environment in the protein and simulate the energy involved in the permeation process.

For the first step, we found that the solvents mimic the behavior of the residues in the core of our NMDA receptor model because in both set of systems Ca^{2+} is more permissive than Mg^{2+} to exchange ligands. As the conclusions in second and third steps, we also observed that the aspargines in the NMDAR model provide the ideal cage environment, that functions like branches and capture the each divalent ion. Hence, an equilibrated TMD NMDAR model was built, the presence of each divalent ion in the protein was simulated, and the permeation mechanism was better understood.

Procuvo nas coisas vagas

Ciência!

— Marisa Monte - A Alma e a Matéria

ACKNOWLEDGEMENTS

I was one of those persistent and curious kids, but I could not have come forward if it was not for my amazing parents who were extremely supportive of all my dreams. Thank you Fátima and José Carlos for everything. I would also like to thank my brother Elder Veras for being supportive to his nerdy sister and to our parents in Brazil when I could not. And I want to extend my deepest gratitude to Rafael Izbicki for all his encouragement and support as my partner in science, in grad school, and in life!

I would like to express my gratitude to my advisor, Maria Kurnikova, for her support and guidance throughout my research. I would also like to extend my appreciation to Jon Johnson for his support and advise.

I also want to thank Christian Legaspi, Emily Daniels Weiss, Hadi Abroshan, Jon Willcox, José Flores, Matheus Tanha, Mike Yonkunas, Nilesh Dhumal, Rafael Bassi Stern, Samaneh Mesbahi, and Serzhan Sakipov for all the comments that directly or indirectly contributed to this thesis.

The journey has just begun!

CONTENTS

1	INTRODUCTION	1
2	USING SOLVENT TO UNDERSTAND ION'S ENVIRONMENT	8
2.1	Introduction	8
2.2	Methodology	19
2.2.1	Water exchange Using Ab Initio Quantum Chemical Calculations	19
2.2.2	Solvation Free Energy Using Thermodynamic Integration	20
2.2.3	Rate of Solvent Exchange in Molecular Dynamic Simulations	22
2.2.4	Transition Energy of Exchange of Water in the Solvation Shell of Mg^{2+}	23
2.3	Results and Discussion	26
2.3.1	Divalent Ion Water Exchange Energies Accurately Calculated	26
2.3.2	Solvation Free Energy Of Divalent Ions in Water and Amides Solvents	29
2.3.3	Rate of Exchange	34
2.4	Conclusion	37
3	MODELING NMDA RECEPTORS	39
3.1	Introduction	39
3.2	Methodology	48

3.2.1	Modeling the Transmembrane Domain	48
3.2.2	Equilibration and Production Run	50
3.3	Results and Discussion	55
3.3.1	TMD NMDAR Model in Vacuum	55
3.3.2	TMD NMDAR Model in Membrane and Water	57
3.4	Conclusion	66
4	SIMULATING DIVALENT ION INTERACTIONS IN TRANSMEMBRANE DOMAIN OF NMDAR	70
4.1	Introduction	70
4.2	Methodology	71
4.2.1	Number of Oxygen Ligands	71
4.2.2	Free Energy of Ca^{2+} in the Binding Site Compared to Mg^{2+}	72
4.2.3	Permeation of Each Divalent Ion: Exchange Between Wa- ter and Protein Residues	72
4.3	Results and Discussion	74
4.3.1	Water and ASN exchange in the Protein Environment . .	74
4.3.2	Free Energy Cycle	76
4.4	Conclusion	82
5	CONCLUSIONS AND FUTURE WORK	84
5.1	Future Work	87
	Appendix A GAUSSIAN QUADRATURE POINTS AND WEIGHTS	88
	Appendix B COMMAND LINES AND SCRIPTS	90
B.1	Gaussian and Antechamber	90
B.2	AMBER: Sample of a Restraint Input File	91
	BIBLIOGRAPHY	93

LIST OF FIGURES

Figure 1.1	Schematic representation of a synaptic signal in a healthy brain tissue	3
Figure 1.2	Schematic overview of the thesis	7
Figure 2.1	The ion interactions change from the outside to the core of the protein	9
Figure 2.2	Oxygen donor interactions with a divalent positively charged ion M^{2+}	10
Figure 2.3	Ion-water coordinated complex	11
Figure 2.4	A pictorial representation of associative and dissociative mechanisms	13
Figure 2.5	The interaction between an ion and amide is a simple model for the interaction of the same ion in the channel .	15
Figure 2.6	Amide solvent charges used in the simulations	20
Figure 2.7	Scenarios used to calculate the solvation free energy . . .	21
Figure 2.8	Results from the Ca^{2+} -water <i>ab initio</i> quantum calculations	26
Figure 2.9	Energy of the water exchange reaction. Results from the Mg^{2+} -water <i>ab initio</i> quantum calculations	27
Figure 2.10	Combined Mg^{2+} and Ca^{2+} <i>ab initio</i> calculation results . .	28
Figure 2.11	Solvation free energy calculated for different number of λ s	30
Figure 2.12	Free energy changes between water, NMA, and DMF . .	31
Figure 2.13	$\langle \frac{\partial V}{\partial \lambda} \rangle_{\lambda}$ at each time step in DMF with each of the five- λ s .	33

Figure 2.14	Cumulative exchange of water molecules in the first solvation shell of Ca^{2+}	35
Figure 2.15	Potential of mean force of the exchange of a water molecule from the first solvation shell of Mg^{2+}	36
Figure 2.16	Radial distribution function of oxygen from water, NMA, and DMF	36
Figure 3.1	Schematic representation of the NMDAR transmembrane domain subunits	40
Figure 3.2	Alignment of NaK channel, AMPAR (GluA), and NMDAR (GluN1 and GluN2A) transmembrane domains . .	41
Figure 3.3	The overall NMDAR model color coded according to how the model overlaps NaK and AMPAR templates . .	42
Figure 3.4	NaK and NMDAR equivalent helices	43
Figure 3.5	The addition of the M4s to the modelled M1 –M2 –M3 structure provides a full transmembrane domain model .	45
Figure 3.6	A pictorial representation of the restrained distances and angles	51
Figure 3.7	Alignment of the residues present in our TMD NMDAR model	52
Figure 3.8	A wheel and cartoon representation of the conserved SYTANLAAF motif mutated to A+7T	53
Figure 3.9	The NMDAR model placed in the membrane and water	54
Figure 3.10	NMDAR RMSF for the equilibration in vacuum	56
Figure 3.11	RMSD for 1.2 ns of equilibration of the homology NMDAR model in vacuum	57
Figure 3.12	Total RMSD	58

Figure 3.13	NMDAR RMSF for the production run in the membrane and water	59
Figure 3.14	Average RMSD per residue for 250 ns of the simulations	60
Figure 3.15	RMSDs for α -carbons of the helices in the simulation in which Ca^{2+} was in the core of the NMDAR model	61
Figure 3.16	RMSDs for α -carbons of the helices in the simulation in which Mg^{2+} was in the core of the NMDAR model	62
Figure 3.17	Helicity ratio for each set of 250 ns of simulations	63
Figure 3.18	Pore at 150 ns of simulation	65
Figure 3.19	Water in the cavity of the simulated TMD NMDAR model.	66
Figure 3.20	Distances measured from an oxygen in the serines GluN2A(S632) to a carbon in the cycle in the tryptophans GluN1(W608) and GluN1(W611)	67
Figure 3.21	Distances measured during 250 ns of simulations from the oxygen side chain in the serines GluN2A(S632) to a carbon in the cycle in the tryptophans GluN1(W608) and GluN1(W611)	68
Figure 4.1	Representation of the calculated umbrellas for chosen reaction coordinate	73
Figure 4.2	Total number of oxygen ligands around Ca^{2+} for the time of the simulation	74
Figure 4.3	Each oxygen ligand around Ca^{2+} for the time of the simulation	75
Figure 4.4	Free energy cycle	78
Figure 4.5	$\langle \frac{\partial V}{\partial \lambda} \rangle_{\lambda}$ at each time step for the exchange between Ca^{2+} and Mg^{2+} in a binding site of the TMD NMDAR model .	79

Figure 4.6	Ensemble average $\langle \frac{\partial V}{\partial \lambda} \rangle_{\lambda}$ versus λ -values to calculate free energy results using thermodynamic integration	80
Figure 4.7	Potential of mean force for each divalent ion being placed along the permeation reaction coordinate	81

LIST OF TABLES

Table 2.1	Normalized Energies in kcal/mol for <i>ab initio</i> Ca ²⁺ -water quantum chemical calculations.	24
Table 2.2	Normalized Energies in kcal/mol for <i>ab initio</i> Mg ²⁺ -water quantum chemical calculations. The system had seven water molecules and Mg ²⁺	25
Table 2.3	Energy (kcal/mol) for each number of λ -values for the solvation of each ion in water, for each set of simulations	31
Table 2.4	Solvation free energies in kcal/mol of each divalent ion in NMA. These results are represented in 2.11b	32
Table 2.5	Solvation free energies in kcal/mol calculated using thermodynamic integration with five λ -values	34
Table 2.6	Divalent ion properties in bulk solvent	37
Table 3.1	Percentage of similarity and identity between NaK channel, AMPAR (GluA), and NMDAR (GluN1 and GluN2A) for the residues showed in Figure 3.2	44
Table 4.1	Number of oxygen ligands in the solvation shell of Ca ²⁺ in 250 ns of simulation	76
Table 4.2	Free energy (in kcal/mol) calculated from Mg ²⁺ to Ca ²⁺ using three λ -values	76
Table 4.3	Free energy (in kcal/mol) calculated from Ca ²⁺ to Mg ²⁺ using three λ -values	77

Table 4.4	Free energy (in kcal/mol) calculated from Mg^{2+} to Ca^{2+} using five λ -values	77
Table A.1	Sets of λ and weights in the gaussian quadrature method	89

ACRONYMS

AMPA α -amino-3-hydroxy-5-methylisoxazole-propionate

AMPA AMPA receptor

ATD Amino Terminal Domain

CNS Central Nervous System

DMF N,N-dimethyl-acetanamide

GluA AMPAR subunit

GluN_{1, 2A-D, 3A-B} NMDAR subunits 1, 2A-D and 3A-B

GluR Glutamate receptor

Harlem HAmiltonians to Research LargE Molecules

HF Hartree Fock

iGluR Ionotropic glutamate receptor

LBD Ligand Binding Domain

MD Molecular Dynamics

NMA N-methyl-acetanamide

NMDA N-methyl-D-aspartate

NMDAR NMDA receptor

TI Termodynamic Integration

TMD Transmembrane Domain

US Umbrella Sampling

INTRODUCTION

Our brain function is carried out by an intricate network of excitable cells that communicate via electrical and chemical signals. *Neurons* are the brain's excitable cells, and the molecules that carry chemical signals between neurons are called *neurotransmitters*. *Synapses* are connecting regions that permit a neuron to pass a neurotransmitter to another excitable cell. The region in the cell that releases neurotransmitters is the *presynaptic membrane*, while the region that receives these signaling molecules is the *postsynaptic membrane*. In the postsynaptic membrane, neurotransmitters bind to proteins called *synaptic receptors*, which initiate a set of physiological responses. In other words, neurotransmitters are synaptic receptor's agonists.

The predominant neurotransmitter in our central nervous system is glutamate (Cowan et al., 2001; Curtis et al., 1960, 1959). During a synaptic signal, glutamate activates synaptic receptors named ionotropic glutamate receptors (iGluRs)* (Abraham and Williams, 2003; Malenka and Nicoll, 1999). These synaptic receptors can be classified into subfamilies according to their affinities for non-physiological agonists, such as α -Amino-3-hydroxy-5-methyl-4-isoxazolepropionic acid (AMPA) and N-methyl-D-aspartate (NMDA), and thus

* A list of the acronyms can be found on pp. xv

are called AMPA receptor (AMPA) and NMDAR receptor (NMDAR), respectively. Both AMPAR and NMDAR are permeable to Na^+ and K^+ . NMDARs are permeable to Ca^{2+} while most of AMPAR types are impermeable to it. Moreover NMDAR and AMPAR are both impermeable to Mg^{2+} . Ion selectivity is extremely important for brain functioning and each ion has its own role as will be discussed in the next sections.

NMDARs are Ligand-Gated and Voltage-Dependent Receptors

When no active signal passes from neuron to neuron, the postsynaptic membrane is at its resting potential, typically around -75 mV. This resting potential changes on the order of a mV when a synaptic signal stimulates the presynaptic neuron to release glutamate. The membrane potential changes because, in a healthy brain, glutamate molecules bind to iGluRs and induce an inward ionic current through AMPARs, leading to a slightly positive depolarization of the membrane. At the same time, most of NMDARs are blocked by Mg^{2+} (Dingledine et al. (1999); Traynelis et al. (2010) - see Fig. 1.1).

When there is a sufficiently strong or frequent stimulus that leads to more inward Na^+ current through AMPARs, the membrane may be positively depolarized in a few more mV, like to -50 mV. When this depolarization happens, NMDARs release Mg^{2+} , which results in Ca^{2+} influx through NMDARs while they have bound agonists (Hille, 2001; Nowak et al., 1984). This Ca^{2+} influx can lead to either increases or decreases in synaptic efficacy through multiple mechanisms that are essential for many forms of learning and memory (Abraham and Williams, 2003; Cooke and Bliss, 2006; Dingledine et al., 1999; Traynelis et al., 2010).

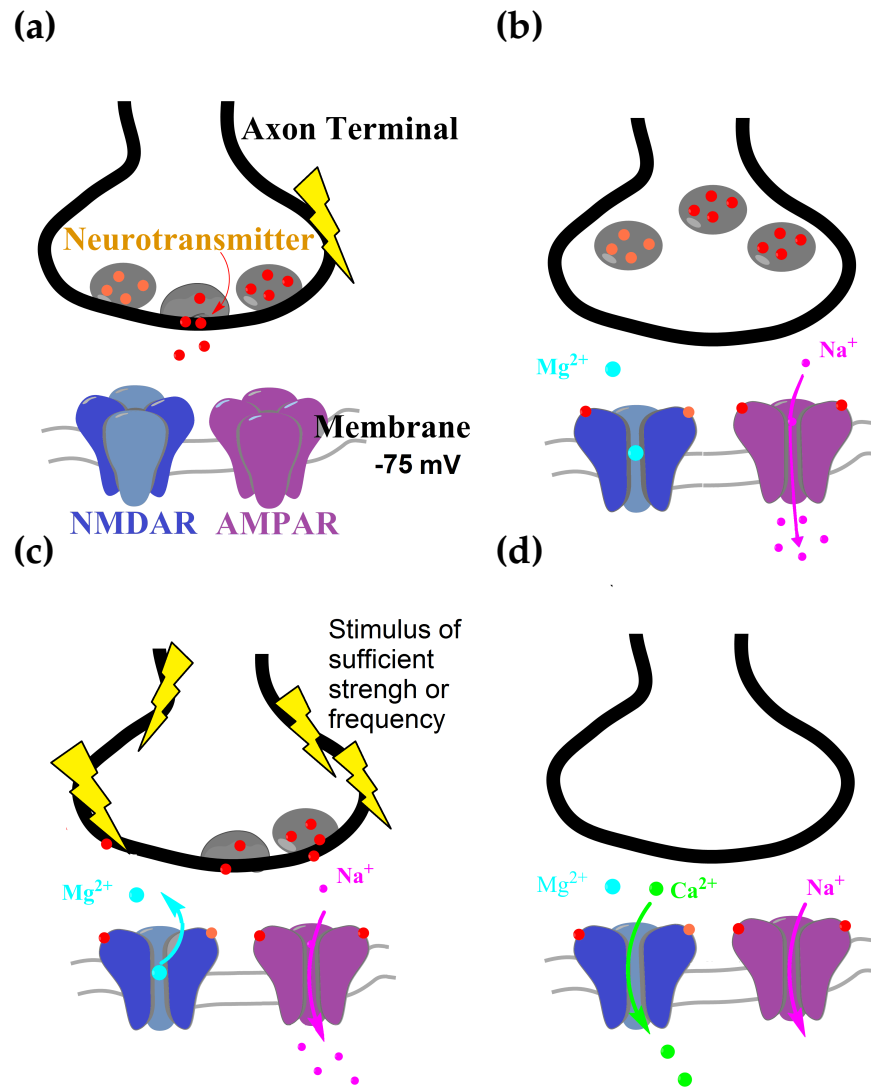


Figure 1.1: Schematic representation of a synaptic signal in a healthy brain tissue. (a) Neurotransmitters, like glutamates represented as red dots, are released from the pre-synaptic axon terminal and bind to the receptors after a synaptic signal. Before the stimulation, the post-synaptic membrane is at resting potential. An NMDAR is represented as the heteromeric blue ion channel, and an AMPAR is represented as the homomeric purple ion channel. The lightning strikes represent a synapse signal. (b) Low-frequency transmission activates an inward Na^+ current through AMPAR, while NMDAR is mostly blocked by Mg^{2+} (not all the ions and molecules present in a synapse are represented in this figure). Despite the presence of glutamate and glycine (agonists), NMDARs still conduct poorly. (c) When there is a pre-synaptic stimulus of sufficient strength or frequency, AMPAR inward current leads to the membrane being depolarized positively to -50 mV, and then NMDARs release Mg^{2+} . (d) Ca^{2+} influx through NMDAR at postsynaptic sites after Mg^{2+} is released.

NMDARs are Targets of Therapeutic Interest

NMDAR dysfunction has been associated with many nervous system disorders such as schizophrenia, depression, bipolar disorder, post-traumatic stress disorder, cerebral ischemia, and epilepsy, as well as Alzheimer's, Parkinson's and Huntington's disease (Javitt, 2004; Kullmann et al., 2000; Paoletti and Neyton, 2007; Paul and Skolnick, 2003). According to the latest issue of the *Heart Disease and Stroke Statistics* journal (Go et al., 2013), there is a fatality approximately every four minutes due to a stroke, and about 87% of the strokes are ischemic. (Doyle et al., 2008; Go et al., 2013). During cerebral ischemia and in neurodegenerative disorders, excessive glutamate release causes over-activation of NMDARs which results in an acute influx of Ca^{2+} and eventually neuron death[†] (Dingledine et al., 1999; Janardhan and Qureshi, 2004; Káradóttir et al., 2005; Traynelis et al., 2010).

One possible technique to control cerebral ischemia is to block the acute influx of Ca^{2+} . Therefore NMDARs blockers, also called antagonists, have a therapeutic potential. However, the NMDAR blockers tested in human clinical trials in stroke and traumatic brain injury have failed to show neuroprotective efficacy (Kemp and McKernan, 2002). In addition, NMDAR antagonists have also produced adverse side effects such as agitation, hallucination, increased blood pressure, and catatonia (Albensi et al., 2004; Hardingham, 2009; Hoyte et al., 2004; Janardhan and Qureshi, 2004; Káradóttir et al., 2005; Kemp and McKernan, 2002; Kiss et al., 2012; Micu et al., 2006; Paoletti and Neyton, 2007; Salter and Fern, 2005). Understanding NMDAR function is critical to drug design efforts to provide an effective drug without adverse side effects (Dingledine et al., 1999; Traynelis et al., 2010).

[†] These are hypotheses for neurodegenerative diseases.

NMDAR Divalent Ion Selectivity Mechanism is a Brainteaser

NMDAR channels allow permeation of Ca^{2+} , while Mg^{2+} binds in the core of the channel and restricts permeation of all other physiological ions (Dingledine et al., 1999; Traynelis et al., 2010). The mechanisms by which NMDARs differentiate these two similar divalent ions are not well understood.

Our goal in this work is to create a realistic atomic level model of the NMDAR region that directly controls divalent ion permeation and use this model to understand, reproduce, and predict selectivity properties of the real system. One can better understand this mechanism at the atomic level by studying the energetic and kinetic behaviors of ion transfer between water and the channel (Kollman, 1993). Hypothetically, a higher positive free energy of an ion solvated in water compared to the association of the same ion inside the protein indicates that the ion would likely never go into the channel because it is energetically unfavorable. On the other hand, a higher positive ion-channel free energy association compared to water indicates a strong ion-channel association, and therefore the ion would likely never leave the channel. For the NMDAR, our initial hypothesis is that a slightly negative free energy value is expected for both ions to maintain the reversibility of association with the channel. Moreover, our hypothesis is that the slow substitution of ligands is which keeps Mg^{2+} in the channel, causing blockage of the NMDAR channel due to kinetic effects, and not due to strong binding energy at the binding site. Furthermore Mg^{2+} release also involve voltage change detection.

Our General Research Approach Combines Multi-Level Computational Methods

Many preliminary steps were taken to calculate the free energies involved in the permeation and selectivity mechanism, each of which required a differ-

ent computational chemistry approach. Such approaches are instrumental in understanding the selectivity mechanism, by allowing the calculation of properties such as solvation free energies, rate of exchange, transition state energy etc. With the support of experimental data, these methods have led to a better understanding of the mechanism. More details of each of the methods that were used are explained in the next chapters.

In this thesis, Chapter 2 discusses how different solvents were used to mimic the protein environment. Chapter 3 demonstrates how the NMDAR channel model was constructed and refined using experimental data, homology modeling, and extensive molecular dynamics simulations. In Chapter 4, this refined model is used in combination with umbrella sampling and thermodynamic integration to compute free energy transitions between ions and for each ion from the binding site to water in the protein cavity. Finally, Chapter 5 summarizes our findings and suggests future research. See Fig. 1.2 for an schematic overview of the research design and general approach.

In short, we used theoretical methods to gain insight into the molecular mechanisms of Ca^{2+} permeation and Mg^{2+} block of NMDARs. The goals were to build a NMDAR model, to use this model to understand the divalent ion selectivity processes, and to learn about NMDAR's function. Most importantly, we are contributing to understanding of a mechanism of immense physiological and pathological importance.

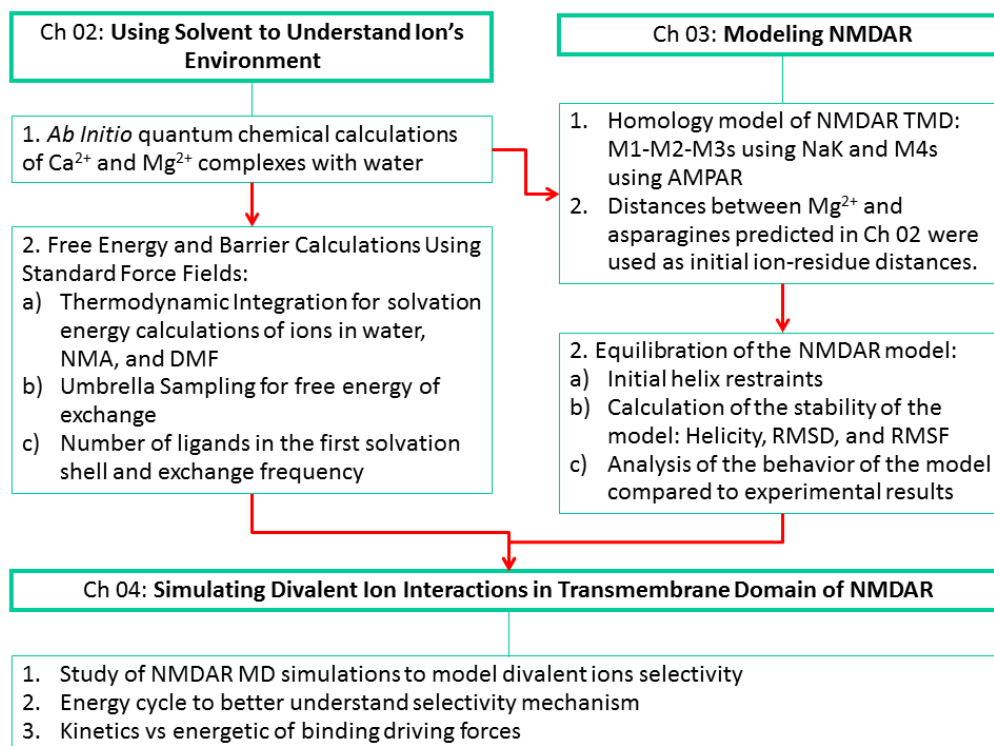


Figure 1.2: Schematic overview of the thesis.

2

USING SOLVENT TO UNDERSTAND ION'S ENVIRONMENT

2.1 INTRODUCTION

The protein NMDAR forms a channel in the neuron membrane that is blocked by Mg^{2+} , but allows an ion with similar chemical properties, Ca^{2+} , to permeate. The first step toward understanding how the channel differentiates between similar ions is to study the ions' environment and how the ions' interactions change while traversing the channel. There are several levels of calculations that could be applied to this study. Unfortunately the more sophisticated simulation methods, such as *ab initio* quantum methods, cannot be applied to the full protein due to their prohibitive computational cost. Therefore before studying the actual ionic environment in the protein, we needed a simple yet reliable model that mimics ligands for divalent ions inside the protein. Here we chose solution systems as this simpler models to mimic the protein environment for divalent ions. The details of how we constructed these simplified models are the subject of this chapter.

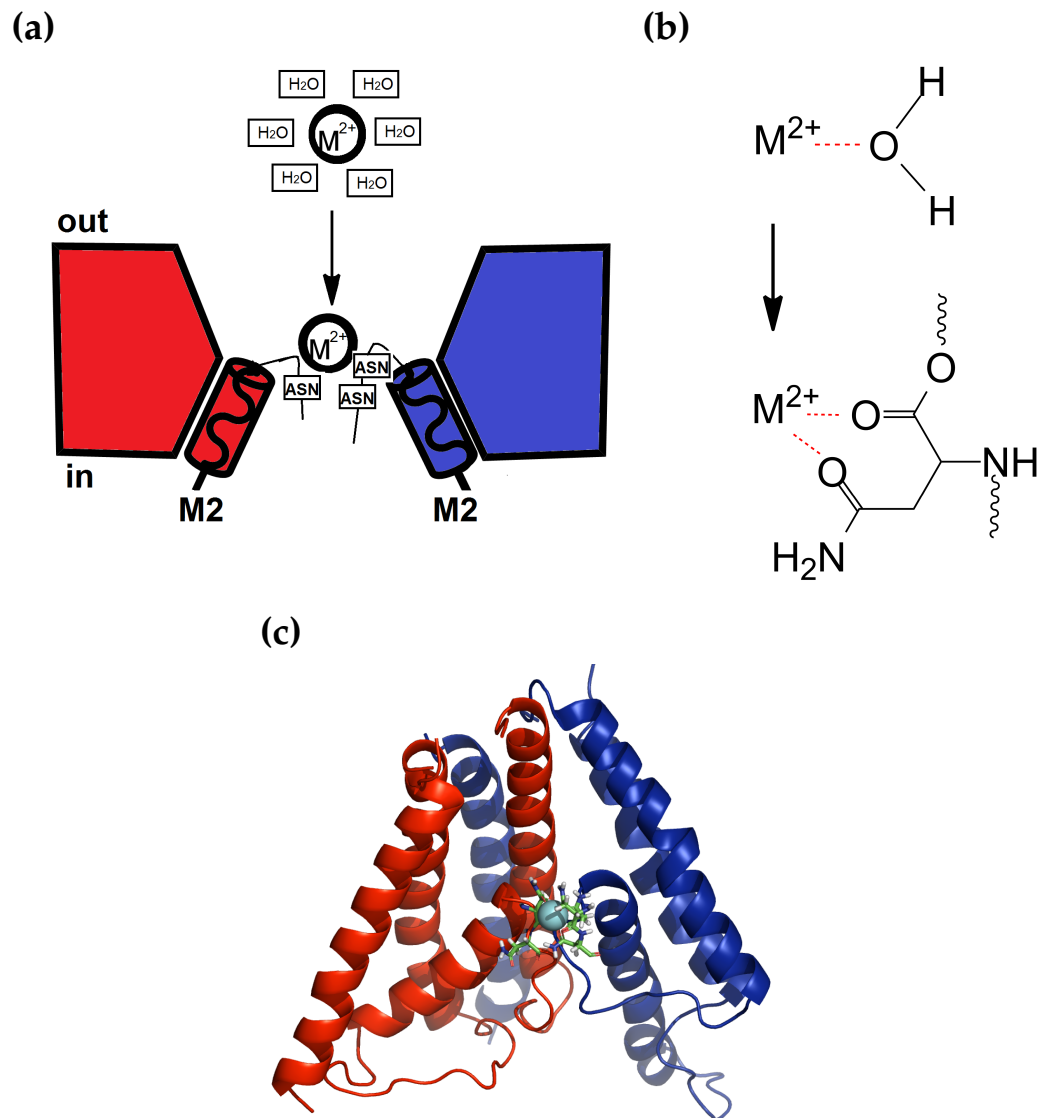


Figure 2.1: The ion interactions change from the outside to the core of the protein. (a) On the top of the figure, a generic divalent positively charged ion M^{2+} is surrounded by water molecules that are going to be substituted by asparagines. In this figure, two of the four subunits are represented in red and blue. The narrowest part of the NMDAR is the portion being depicted, and ASNs are asparagines that surround the ion in this narrow part of the channel. (b) The same substitution is represented as an exchange reaction of one water molecule to one asparagine. When an asparagine coordinates a divalent ion, there are two possible oxygen-donor interactions. (c) The model of two subunits is showed in which the asparagines are represented as sticks.

Ions Interchange Oxygen Interactions While Crossing the Channel

When an ion permeates from the solution into the channel, its environment changes from water to protein residues. The core of the protein transmembrane domain is where the interchange happens, and thus is the focus of our study. In this region, only one permeant ion can be found at a time (Zarei and Dani, 1994), and the residues that closely interact with the ion are believed to be six asparagines from a protein region called M2 (Kuner et al. (1996); Wollmuth et al. (1998a) – see also Fig. 2.1) . Therefore, as an ion moves toward the neuron cytoplasm, oxygen atoms from water molecules that directly interact with this ion are replaced by the asparagine oxygen atoms in the narrowest part of the NMDAR pore .

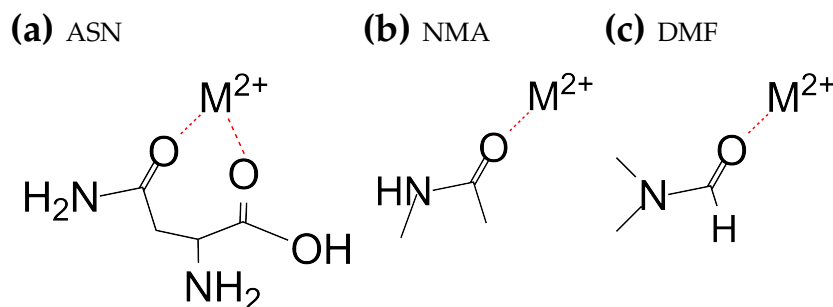


Figure 2.2: Oxygen donor interactions with a divalent positively charged ion M^{2+} . The possible interactions are represented as dotted red lines. (a) The asparagine (ASN) is a protein residue. (b) N,N-dimethyl-formamide (DMF). (c) N-methyl-acetamide (NMA)

In this chapter, we study this replacement of ion-oxygen interaction in various oxygen donor solutions. The solvents that we used to mimic the asparagine effect on divalent ions are amide solvents because ion-asparagine interactions resemble ion-amide interactions (Fig. 2.2). Therefore, we used this smaller systems to have a preliminary understanding of the bigger protein system. Furthermore, we studied ion-solvent systems because we believe that the majority

of the ion-protein interaction will be captured in this toy model system. Ion's properties in solutions and how the interactions change as they pass through a channel have been discussed in the literature in other ion channels such as potassium channels (Bostick and Brooks, 2007; Corry, 2006; Thomas et al., 2007; Varma and Rempe, 2007; Yu et al., 2009), as well as in other classical ion permeation studies (Mullins, 1959).

Solvent Exchange Reaction is Key to Understanding Ion Interaction

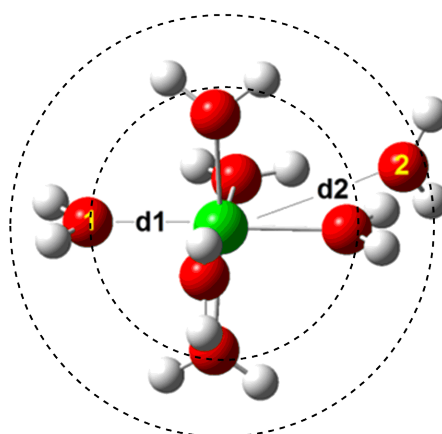


Figure 2.3: Ion-water coordinated complex. Six water molecules are in the first solvation shell, represented within the inner dashed circle. One water molecule of the second solvation shell is represented within the inner and the outer dashed circle. The radius of the first and second coordination shell are d_1 and d_2 , respectively.

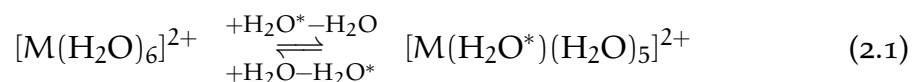
When an ion is in solution, the closest solvent molecules that surround this solute species form the *first solvation shell*, also called *coordination shell* (Fig. 2.3). The number of molecules in this shell is called *coordination number*, which depends on the nature of the solvent and the solute molecules. The solvation shell may have a broader definition than the typical definition in solution, as any chemical species that surrounds a solute is considered to act as a solvent.

For example, the asparagines may act as a solvent in the core of NMDAR for Ca^{2+} and Mg^{2+} .

In solution, the Ca^{2+} coordination numbers for oxygen donor ligands range from six to nine (Katz et al., 1996), but for Mg^{2+} , octahedral six-coordination is found to be most prevalent (Bock and Glusker, 1993; Bock et al., 1994; Katz et al., 1996; Pavlov et al., 1998). The coordination flexibility of Ca^{2+} compared to Mg^{2+} gives important insights about the permeability of each ion in the NMDAR pore because it provides grounds for selectivity by the channel.

A reaction in which a molecule that is part of the coordination shell leaves and is replaced by another molecule is called *solvent exchange reaction*. The examination of the exchange of a water molecule in the first solvation shell can be used to approximate the difficulty in exchanging water for another oxygen donor, e.g. the asparagines.

The simplest investigation of an ion-oxygen coordination exchange reaction that can be measured in an experiment is the ion-water ligand exchange reaction, in which one water molecule in the first solvation shell is substituted by another from the second shell. The shared number of water molecules in the first solvation shell for both ions is six, in which the Ca^{2+} coordination can be higher and the Mg^{2+} can be lower. Hence, the minimal common system to investigate the exchange of one water molecule by another in the coordination shell of Ca^{2+} and Mg^{2+} is a system that consists of seven water molecules and one ion (Aakesson et al., 1994; Helm and Merbach, 2005), represented by the following reaction:



where * differentiates the approaching from the leaving water molecule, and M is the metal with a 2+ charge .

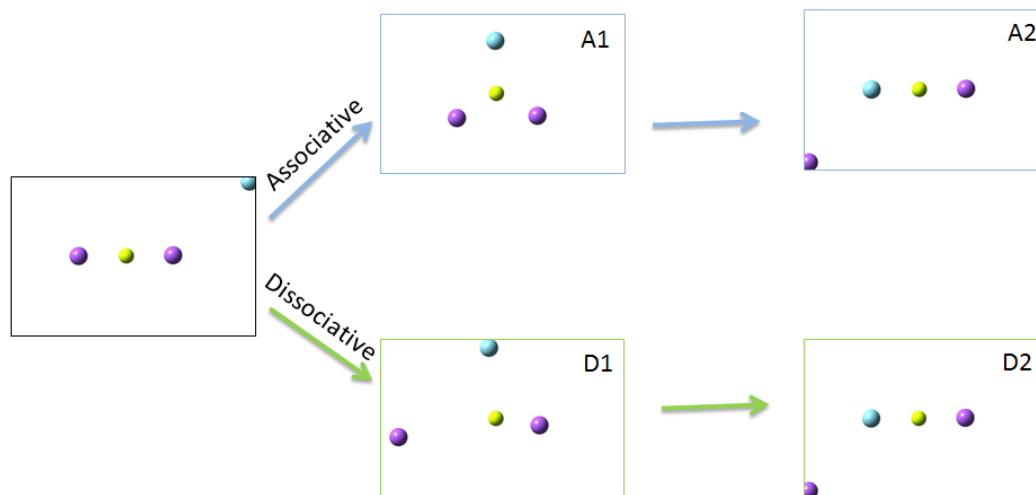


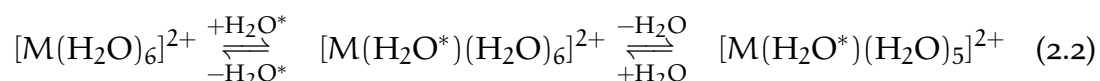
Figure 2.4: A pictorial representation of associative (A) and dissociative (D) mechanisms. A₁ and D₁ represent the intermediates, while A₂ and D₂ represent the final systems. The approaching entity is represented in blue. In the intermediate system A₁, the approaching molecule and the leaving one are part of the first solvation shell, while in D₁ the leaving molecule needs to leave the first solvation shell before the approaching one associates. Both final systems are the same.

This exchange can happen via an associative or dissociative mechanism. The *associative mechanism* occurs when the approaching ligand coexists in the complex system with the leaving ligand. In a *dissociative mechanism*, the leaving molecule dissociates as the new ligand approaches it (Fig. 2.4).

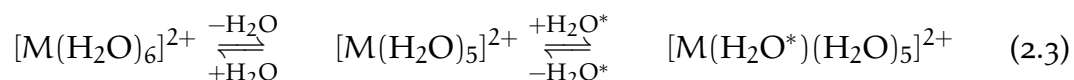
The transitional complex system with the lowest energy besides the final one is called an *intermediate complex*. Each mechanism can be related to a different coordination number of the intermediate complex: in an associative mechanism, an intermediate of increased coordination number with respect to the initial structure can be detected, while in a dissociative mechanism there is a

reduction in the coordination number for the intermediate state (Langford and Gray, 1965).

When explicitly including the intermediate complex in our minimal water exchange reaction (Eq. 2.1), we have the following equation for an associative mechanism:



And for a dissociative mechanism:



Here, the mechanisms by which Ca^{2+} and Mg^{2+} exchange a water molecule are investigated on a quantum level of calculation. Various experimental and computational oxygen-donor interactions with Ca^{2+} and Mg^{2+} investigations have been done (Akesson et al., 1994; Dudev et al., 1999; Gilson, 1995; Helm and Merbach, 1999, 2005; Ikeda et al., 2007; Lightstone et al., 2001; Rao et al., 2008; Schwenk et al., 2004) and their findings support our discussions in this chapter.

In summary, the water exchange energy calculated using quantum mechanics describes how each ion interacts with the oxygens around them. We now shift our focus to the exchange at water with asparagine-like interactions in condensed matter.

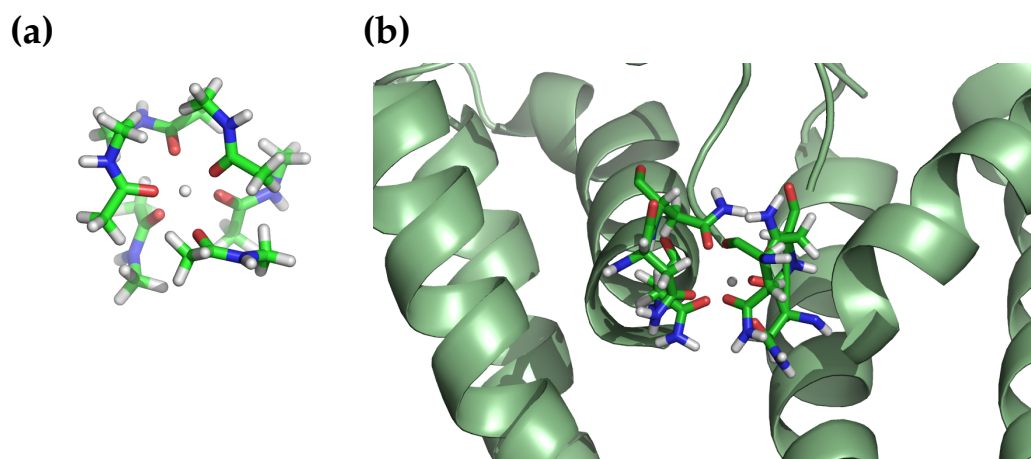


Figure 2.5: The interaction between an ion and amide is a simple model for the interaction of the same ion in the channel. (a) Amides surrounding an ion. The image shows a coordination of six oxygen atoms per ion. (b) The same ion is in the channel, where the asparagines are shown as sticks and the remaining aminoacids as cartoons. Here the same six oxygen-ion coordination number is represented in the channel.

Amide-Ion Systems Mimic Asparagine-Ion Interactions

Amides are protein-like solvents that have ion-oxygen interactions similar to ion-asparagine interactions, and thus can approximate the effect of asparagines in our system. The study of the energy differences and barriers of each ion in water and each ion in amides gives a quantitative approximation of the interaction changes across the channel (Fig. 2.5). *N*-methyl-acetamide (NMA) and *N,N*-dimethylformamide (DMF) are the amides that we used to represent the asparagine interactions (Fig. 2.2).

Computational Tools Provide a Better Understanding of our Studied Systems

Since quantum-level calculations are computationally expensive, they cannot be easily applied to big systems (Becker et al., 2001; Leach, 2001). A way of simplifying calculations involving big systems consists of ignoring electronic

motion, where we consider the interactions within parts of a system as represented by simple functions, e.g. Hooke's law. The collection of the parameters that are used in these functions, as well as the functions themselves, are called *empirical force fields*. These force fields are the standard tool used to simulate large systems like proteins in a membrane. The force fields that have been widely used for biological simulations are the fixed charge force fields such as AMBER (Cornell et al., 1995), CHARMM (MacKerel Jr. et al., 1998), and OPLS (Jorgensen and Tirado-Rives, 1988) force fields. When the force field is used to predict how the system changes with time, the simulation is called *molecular dynamics* (MD).

Various time averages of properties can be calculated using MD methods. An example is *solvation free energy*. This is the energy necessary to solvate a solute, i.e., to transfer a solute from a fixed position in the solvent ideal gas phase or vacuum into a fixed position in the liquid solvent phase (Marcus, 1998). The solvation free energy describes the thermodynamic stability of an ion in a solution, and thus may be used to understand the interactions involving each ion.

The solvation free energy can be calculated using *Thermodynamic integration* (TI) (Chipot and Pohorille, 2007; Leach, 2001). TI is used to compute a free energy difference (ΔG) between two systems by running a set of individual equilibrium MD simulations in which an initial system is gradually transformed into a final system, e.g. from ion-free solvent to an ion in solvent. The essence of free energy calculations is to record and analyze fluctuations in energies of the initial and final systems as the simulation progresses using the following equation:

$$V(\lambda) = (1 - \lambda)V_0 + \lambda V_1 \quad (2.4)$$

where λ is a coupling parameter used to interpolate between the initial (with a potential energy V_0 , in which $\lambda = 0$) and the final (with a potential energy V_1 , in which $\lambda = 1$) systems and V is the final potential energy of each combined system.

The difference in free energy is computed by:

$$\Delta G = \int_0^1 \left\langle \frac{\partial V}{\partial \lambda} \right\rangle_{\lambda} d\lambda \quad (2.5)$$

where $\langle \frac{\partial V}{\partial \lambda} \rangle_{\lambda}$ is the ensemble average of $\frac{\partial V}{\partial \lambda}$ for each λ -value. Here, gaussian quadrature is used to calculate the above integral:

$$\Delta G = \sum_i w_i \left\langle \frac{\partial V}{\partial \lambda} \right\rangle_i \quad (2.6)$$

where w_i are the weights chosen according to the λ quadrature points. See Appendix A for the λ values and their respective weights.

Thus, in the bulk solvent environment, TI is an appropriate tool to estimate the solvation energy for both Ca^{2+} and Mg^{2+} in water and amides.

Another suitable tool used for checking the solvent-ion interactions is the study of the *radial distribution function* (RDF). The RDF calculates radial probabilities of a given type of atom or molecule at a certain distance around an atom of interest. We can also calculate the rate at which the molecules from the first solvation shell exchange with the other solvent molecules; this is done by using the frequency at which the molecules in the coordination shell exchange with the bulk solvent in a standard MD simulation.

Potential of mean force $A(\xi)$ is the free energy along a certain coordinate direction ξ . This free energy can be calculated using the following function:

$$A(\xi) = -k_B T \ln P(\xi) \quad (2.7)$$

where $P(\xi)$ is the probability of the conformation correspondent to each point along the coordinate ξ , obtained by evaluating the empirical frequencies in the simulation. This kind of calculation assumes that every possible state will be sampled.

In simulations where there is a high barrier along the coordinate ξ , it is very likely that a standard MD will rarely or never sample some of the states, resulting in wrong empirical probability values, and therefore unreliable $A(\xi)$. In these situations, it is necessary to use techniques that will enforce the system to simulate regions that would otherwise be poorly sampled. For example, a harmonic potential can be added along ξ to enforce certain \vec{r}_{eq} positions to be sampled:

$$V'(\vec{r}) = \frac{1}{2}k(\vec{r} - \vec{r}_{eq})^2 \quad (2.8)$$

where \vec{r} is a vector position within the coordinate reaction ξ and V' is the added potential energy. This technique, called *umbrella sampling* (US), is used to obtain accurate relative free energy differences between macrostates (Souaille and Roux, 2001; Torrie and Valleau, 1977). Once all the coordinates are sampled, one needs to unbias the probabilities, otherwise the free energy will still be inaccurate because of the extra potentials added to the system.

In this work, this is done by applying the weighted histogram analysis method (WHAM), in which weights are given to the probabilities of the bias that min-

imizes the statistical error (Becker et al., 2001; Chipot and Pohorille, 2007; Kumar et al., 1992; Leach, 2001; Souaille and Roux, 2001; Tuckerman, 2008). As a result, a free energy profile is calculated. This profile might have an energy barrier ΔG^\ddagger between states (or conformations). The rate to change from one state to another may be calculated using:

$$k = A \exp(-\Delta G^\ddagger/RT) \quad (2.9)$$

where A is the pre-exponential factor, R is the energy constant, T is the temperature.

In the next sections the methodologies we used for the solvent-ion interaction studies are presented.

2.2 METHODOLOGY

2.2.1 Water exchange Using *Ab Initio* Quantum Chemical Calculations

The water exchange reactions for Mg^{2+} and Ca^{2+} were investigated using *ab initio* quantum chemical calculations using Hartree-Fock and MP2 levels with different basis set (6-31G up to 6-31++G**) (Leach, 2001). The simulations, performed with GAUSSIAN (Frisch et al., 2003, 2009), were composed of a single ion and seven water molecules. Each system was optimized while keeping the distance (d_1) between the oxygen of one water molecules and the ion at a desired value. This distance was increased by 0.1 Å incrementally up to 5 Å, and the optimization was repeated for each system while maintaining d_1 fixed (Fig. 2.3). The distance between the ion and the oxygen of the approaching water molecule (d_2) was measured and the total energy was recorded.

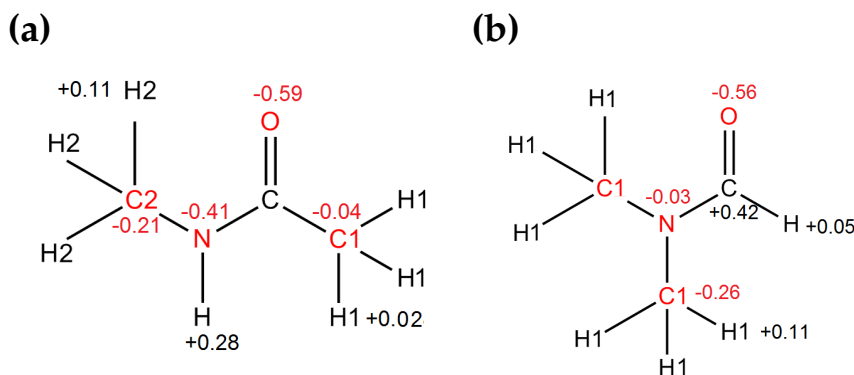


Figure 2.6: Amide solvent charges used in the simulations. Red atoms represent negative partial charges. Atoms with the same presented name have the same partial charge. (a) NMA. (b) DMF.

2.2.2 Solvation Free Energy Using Thermodynamic Integration

Condensed matter MD simulations for Mg^{2+} and Ca^{2+} in TIP3P water (Jorgensen et al., 1983), DMF, and NMA were carried out using HARLEM (Kurnikov, 1999) and AMBER packages (Case et al., 2012) under periodic boundary conditions. Partial charges and all other force field parameters were available for water and NMA in the software packages, but not for DMF, and thus parameters for DMF needed to be generated.

The parameter development process was aided by the ANTECHAMBER (Wang et al., 2001) component of the AMBER suite, using the well-established protocol by Cornell et al. (1995). Initial geometries were obtained by optimizing the DMF molecule at the Hartree-Fock level of theory with the 6-31G* basis set. Partial charges were then derived from the HF/6-31G* electrostatic potential grid using the restrained electrostatic potential method (RESP). The commands used to obtain the partial charges are listed in Appendix B.1. The optimized geometries and force field potentials match well with both empirical data and previous calculations. See Fig. 2.6 for NMA and DMF final partial charges.

After obtaining an appropriate set of parameters for the solvents, TI was used to compute the solvation free energy difference of Ca^{2+} and Mg^{2+} in water, NMA, and DMF. The ion parameters were obtained from [Aqvist \(1990\)](#).

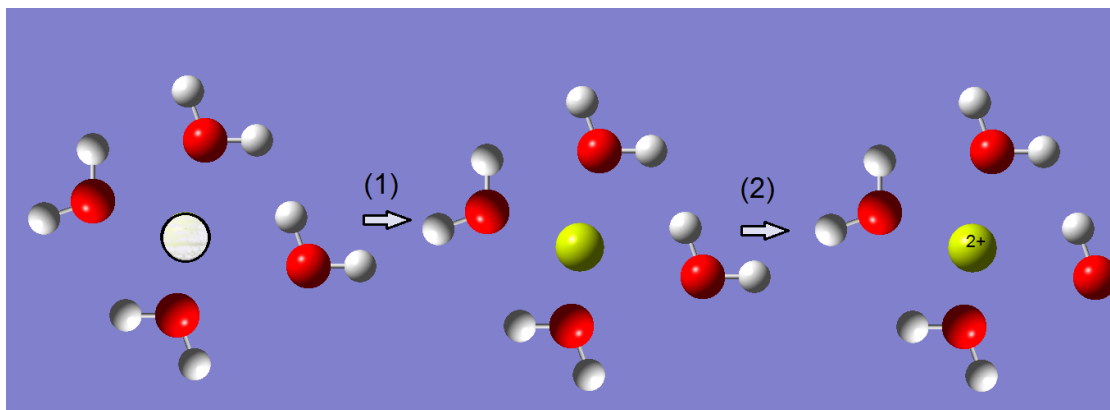


Figure 2.7: Scenarios used to calculate the solvation free energy. Here the solvent is water. The central atom is absent in the first system - it is equivalent to having the atom in an infinite position. The second system is an uncharged atom solvated by water. The third system is the solvated charged atom. We need two steps to calculate the solvation free energy for each divalent ion: (1) change the system from the solvent without solute to the solvated uncharged atom. (2) change the charge of the solvated atom from zero to $2+$.

Because of the strong interaction between ions and either water or amide, the solvation represents a very strong interaction change in the solvent system. To avoid a drastic change that causes either termination of the process or unreliable results, we split the calculations in two scenarios for each of the coupling parameter λ so as to have a smoother transition: the solvation of the neutral atom, and the transition from the neutral atom to the ion (Fig. 2.7). The simulations were performed for 5 up to 12 ns for solvation of each ion in each of the solvents.

The analysis was performed for the last 4 ns of simulation for each set. Hence for every set there is at least 1 ns of equilibration. For comparison, independent simulations were performed using three, five, seven, and nine λ -values

for water and up to seven for NMA. The λ -values were chosen to follow the quadrature method for numerical calculation of the integral (see Appendix A). For water, we used a box with approximate volume of $8 \times 10^3 \text{ \AA}^3$ with 195 water molecules; for the other solvents, the boxes were $3 \times 10^3 \text{ \AA}^3$, with 80 molecules. Langevin temperature control (Adelman and Doll, 1976), TIP3P water (Jorgensen et al., 1983), and AMBER force field (Cornell et al., 1995) were used. Particle Mesh Edwald (PME) (Darden et al., 1993) method was applied for the long range electrostatic potential interactions.

2.2.3 Rate of Solvent Exchange in Molecular Dynamic Simulations

To study the rate of exchange, simulations were done with the same solvent boxes used in the TI calculations, and also with bigger sized boxes, for comparison of results (with 160 solvent molecules for NMA and DMF and 300 for water). It is possible to use bigger boxes because straightforward MD simulations are not as expensive as MD simulations for TI calculations. RDFs of the solvent oxygens around the cation were calculated from the trajectories over 25 ns with a bin size of 0.1 \AA (from 0 \AA up to 8 \AA in total).

All MD simulations were carried out using AMBER package under periodic boundary conditions. Long-range electrostatic interactions were treated with PME (Darden et al., 1993) method. First the solvent boxes were equilibrated until each system acquired the experimental density. The simulations were performed using isothermal-isobaric ensemble at a pressure of 1 atm and temperature of 300 K using a Langevin thermostat (Adelman and Doll, 1976). Then we calculated the exchange of the first solvation shell of water, NMA, and DMF. This was done by counting how often each solvent molecule from first solvation shell exchanges with a molecule from the second solvation shell.

2.2.4 Transition Energy of Exchange of Water in the Solvation Shell of Mg^{2+}

Additionally, the transition energy and rate of exchange were calculated using umbrella sampling (Kästner, 2011; Torrie and Valleau, 1977) with the same solvents. The procedure used the same AMBER force field, Langevin thermostat control (Adelman and Doll, 1976). One of the water molecules had distance harmonically constrained in 1.6 Å. This constrained distance was increased by increments up to 8.0 Å and the simulation was repeated for each system for 10 ns. The distance between the constrained water molecule and Mg^{2+} was recorded. The harmonic force constant k as represented in Eq. 2.8 was 60 kcal.mol⁻¹Å⁻² for all restrained distances by increments of 0.25 Å, 20 kcal.mol⁻¹Å⁻² for distances between 5.2 Å and 6.0 Å by increments of 0.1 Å, and 150 kcal.mol⁻¹Å⁻² for distances between 1.5 Å and 3.2 Å by increments of 0.1 Å.

The PMF was obtained by a weighted sum over the extracted data, with a tolerance of 10⁻³. A fast and memory efficient implementation of the WHAM by Grossfield (2012) was used to perform these analyses.

Such PMF has to be corrected to include the 3D motion of the ligand that is exchanging. Thus we subtracted the entropic effect $S' = ST = 2RT\ln(\xi)$ (Allnér et al., 2012) from the PMF obtained with WHAM. We calculated the rate of exchange based on the free energy barrier by using Equation 2.9 with the pre-exponential factor of $1.3 \times 10^{13}\text{s}^{-1}$ (Allnér et al., 2012).

Table 2.1: Normalized Energies in kcal/mol for *ab initio* quantum chemical calculations. The system had seven water molecules and one Ca^{2+} .

d1 (Å)	d2 (Å)	Normalized Energies (kcal/mol)									
		HF					MP2				
		6-31G	6-31G*	6-31G**	6-31++G**	6-31G	6-31G*	6-31G**	6-31G	6-31G*	6-31G**
...
3.1	2.46	7.10	4.47	4.32	4.13	7.15	4.63	4.09	7.15	4.63	4.09
3.3	2.46	6.35	4.26	4.17	4.06	6.40	4.46	4.08	6.40	4.46	4.08
3.4	2.46	5.64	3.92	3.86	3.79	5.70	4.10	3.86	5.70	4.10	3.86
3.5	2.45	4.79	3.44	3.42	3.39	4.84	3.62	3.48	4.84	3.62	3.48
3.6	2.45	3.85	2.88	2.89	2.89	3.89	3.04	2.99	3.89	3.04	2.99
3.7	2.45	2.88	2.26	2.30	2.33	2.91	2.41	2.43	2.91	2.41	2.43
3.8	2.46	1.96	1.64	1.70	1.73	1.98	1.75	1.83	1.98	1.75	1.83
3.9	2.46	1.15	1.05	1.12	1.16	1.17	1.13	1.24	1.17	1.13	1.24
4.0	2.46	0.53	0.56	0.62	0.65	0.53	0.61	0.70	0.53	0.61	0.70
4.1	2.46	0.13	0.19	0.23	0.25	0.13	0.22	0.28	0.13	0.22	0.28
4.2	2.46	0.00	0.00	0.00	0.00	0.00	0.00	0.00	0.00	0.00	0.00
4.3	2.46	0.16	0.01	-0.04	-0.07	0.16	-0.01	-0.09	0.16	-0.01	-0.09
4.4	2.46	0.60	0.24	0.13	0.06	0.61	0.20	0.01	0.61	0.20	0.01
4.5	2.46	1.30	0.68	0.51	0.38	1.30	0.62	0.30	1.30	0.62	0.30
4.6	2.45	2.21	1.31	1.07	0.89	2.23	1.24	0.78	2.23	1.24	0.78
4.7	2.45	3.27	2.10	1.80	1.54	3.31	2.01	1.41	3.31	2.01	1.41
4.9	2.45	3.73	3.29	2.39	2.13	3.66	3.13	2.00	3.66	3.13	2.00
5.0	2.45	4.30	3.59	2.66	2.38	4.24	3.42	2.22	4.24	3.42	2.22

Table 2.2: Normalized Energies in kcal/mol for *ab initio* quantum chemical calculations. The system had seven water molecules and one Mg^{2+} .

		Normalized Energies (kcal/mol)												
		HF					MP2							
d1	d2	6-31G	6-31G*	6-31+G*	6-31+G**	6-31++G**	6-31G	6-31G*	6-31+G*	6-31+G**	6-31++G**	6-31G	6-31G*	6-31G**
2.0	3.97	0.61	0.78	0.78	0.83	0.83	0.61	0.78	0.78	0.83	0.83	0.61	0.78	0.82
2.1	3.98	0.00	0.00	0.00	0.00	0.00	0.00	0.00	0.00	0.00	0.00	0.00	0.00	0.00
2.3	3.96	1.60	1.18	1.07	0.99	0.99	1.60	1.18	1.07	0.99	1.00	1.61	1.17	1.17
2.5	3.95	4.32	3.63	3.41	3.24	3.24	4.32	3.63	3.41	3.24	3.26	4.34	3.65	3.65
2.6	3.94	5.60	4.84	4.57	4.37	4.37	5.60	4.84	4.57	4.37	4.38	5.62	4.91	4.91
2.8	3.95	7.42	6.72	6.41	6.18	6.18	7.42	6.72	6.41	6.18	6.20	7.46	7.04	7.04
2.9	3.96	7.72	7.22		6.71	6.71	7.72	7.22		6.71	6.73	7.78	7.74	7.74
3.0	3.97	7.49	7.34	7.03	6.90	6.90	7.49	7.34	7.03	6.90	6.93	7.57	7.93	7.93
3.2	3.97	5.94	6.63	6.38	6.40	6.40	5.94	6.63	6.38	6.40	6.43	6.03	7.19	7.19
3.3	3.97	4.98	6.05	5.82	5.89	5.89	4.98	6.05	5.82	5.89	5.93	5.07	6.54	6.54
3.4	3.97	4.09	5.46	5.25	5.35	5.35	4.09	5.46	5.25	5.35	5.39	4.16	5.86	5.86
3.5	3.97	1.08	3.89	4.02	4.23	4.23	1.08	3.89	4.02	4.23	4.27	1.12	4.15	4.15
3.6	3.96	-0.30	2.71	2.84	3.06	3.06	-0.30	2.71	2.84	3.06	3.11	-0.27	2.92	2.92
3.7	3.95	-1.27	1.76	1.89	2.09	2.09	-1.27	1.76	1.89	2.09	2.14	-1.25	1.95	1.95
3.8	3.94	-1.78	1.14	1.24	1.41	1.41	-1.78	1.14	1.24	1.41	1.47	-1.76	1.32	1.32
3.9	3.93	-1.84	0.88	0.92	1.07	1.07	-1.84	0.88	0.92	1.07	1.13	-1.82	1.03	1.03
4.2	3.90	0.30	2.07	1.89	1.87	1.87	0.30	2.07	1.89	1.87	1.94	0.33	2.18	2.18
4.3	3.90	1.50	2.98	2.72	2.62	2.62	1.50	2.98	2.72	2.62	2.69	1.58	3.08	3.08
4.4	3.91	2.42	4.05	3.68	3.51	3.51	2.42	4.05	3.68	3.51	3.59	2.57	4.13	4.13
4.5	3.92	3.24	5.00	4.38	4.24	4.24	3.24	5.00	4.38	4.24	4.32	3.26	5.09	5.09
4.6	3.92	4.09	5.75	4.97	4.79	4.79	4.09	5.75	4.97	4.79	4.88	4.08	5.81	5.81

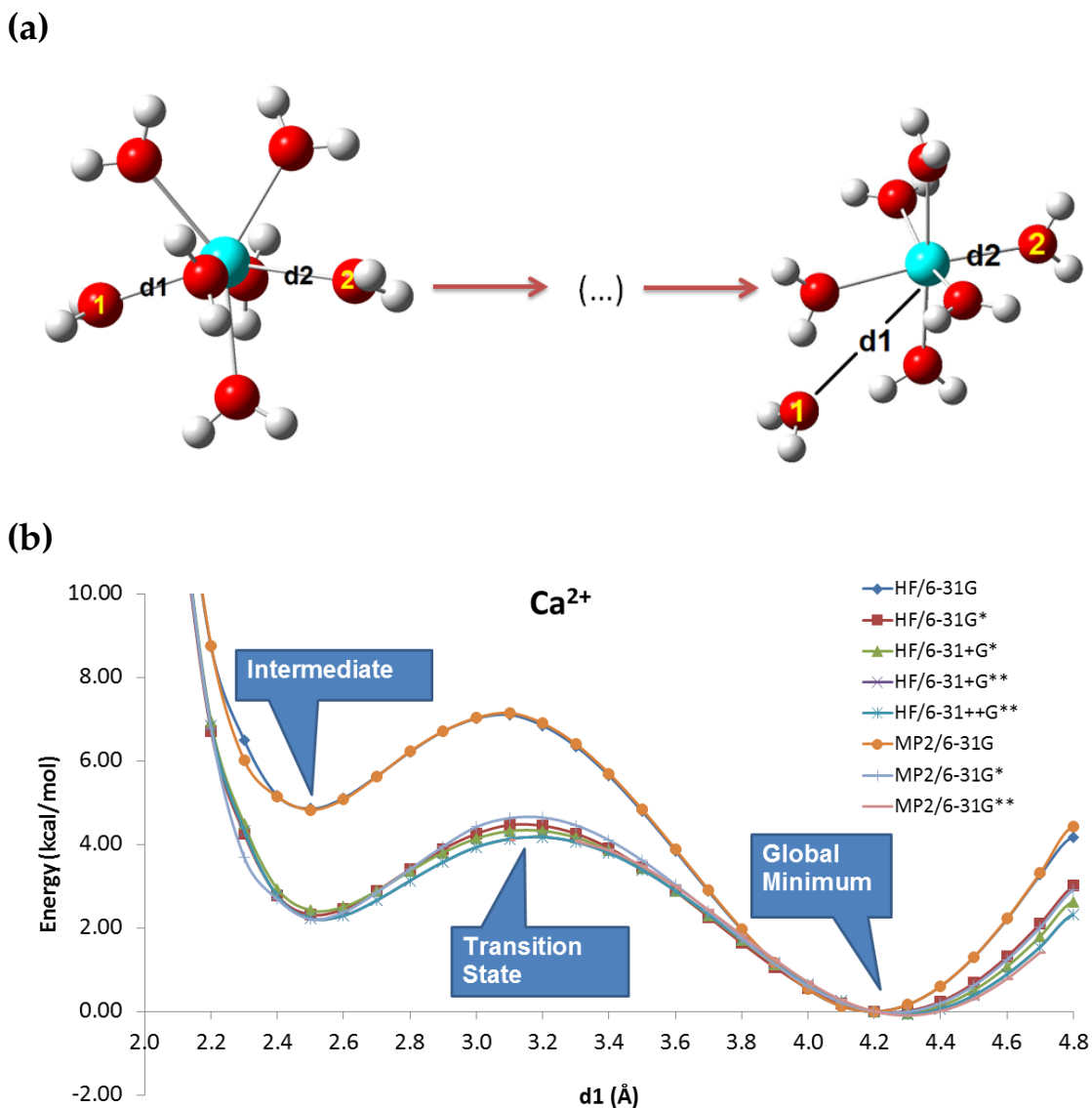


Figure 2.8: Results from the Ca^{2+} -water ab initio quantum calculations. (a) Schematic representation of Ca^{2+} -water exchange mechanism; d_1 is the fixed distance of the leaving water molecule and d_2 is the distance of the approaching water molecule. (b) The graph shows the energy with respect to the lower energy among all sets of energies after the optimization for each fixed d_1 .

2.3 RESULTS AND DISCUSSION

2.3.1 Divalent Ion Water Exchange Energies Accurately Calculated

Figures 2.8 and 2.9 and Tables 2.1 and 2.2 show the ab initio calculation results. The global minimum in each of the graphs occur at $d_1 = 4.2 \text{ \AA}$ for

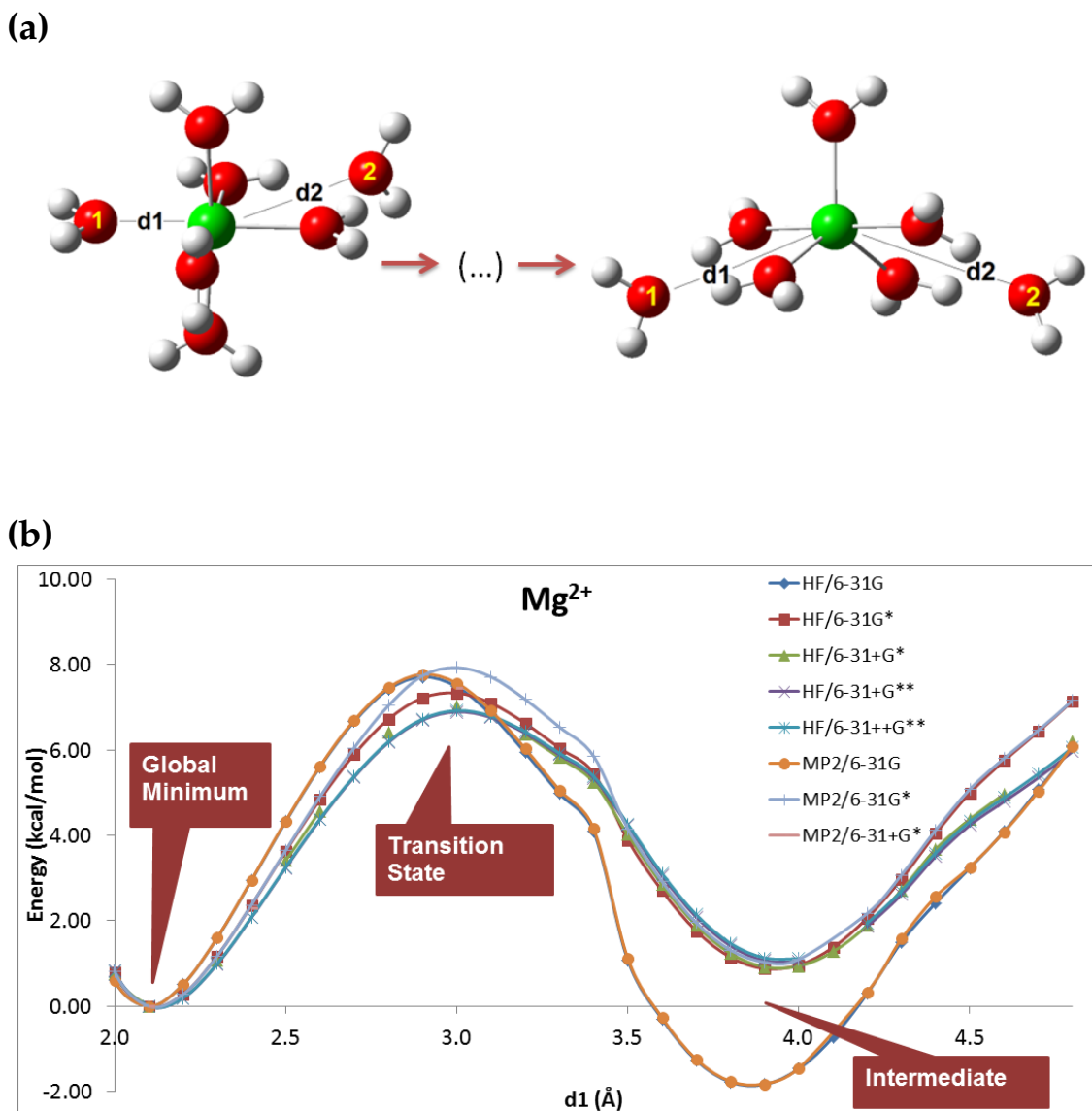


Figure 2.9: Energy of the water exchange reaction. Results from the Mg^{2+} -water ab initio quantum calculations. (a) Schematic representation of Mg^{2+} -water exchange mechanism; d_1 is the fixed distance of the leaving water molecule and d_2 is the distance of the approaching water molecule. (b) The graph shows the energy with respect to the lower energy among all sets of energies after the optimization for each fixed d_1 .

Ca^{2+} and at $d_1 = 2.1 \text{ \AA}$ for Mg^{2+} . These were the most stable system in each of our set of simulations. Visual inspection of each final optimized system at these fixed d_1 shows that the systems in this global minimum corresponded to

an ion with six water molecules in the coordination shell and the seventh water molecule was part of the second solvation shell.

The second most stable system in each set of simulations corresponds to the intermediate structure. For Ca^{2+} the intermediate is found at 2.5 Å and for Mg^{2+} at 3.9 Å. For Ca^{2+} , the local minimum corresponds all seven water molecules symmetrically surrounding the ion.

For Mg^{2+} , the local minimum occurs when five water molecules are symmetrically located at the first solvation shell. From the results in Fig. 2.9 notice that polarizability functions have an important effect on the position and on barrier energy value of the local and global minima. For the Mg^{2+} system, the absence of polarizability could lead a completely different structure being interpreted as the global minimum, in which the five water molecules in the coordination shell would be mistaken as the most stable structure.

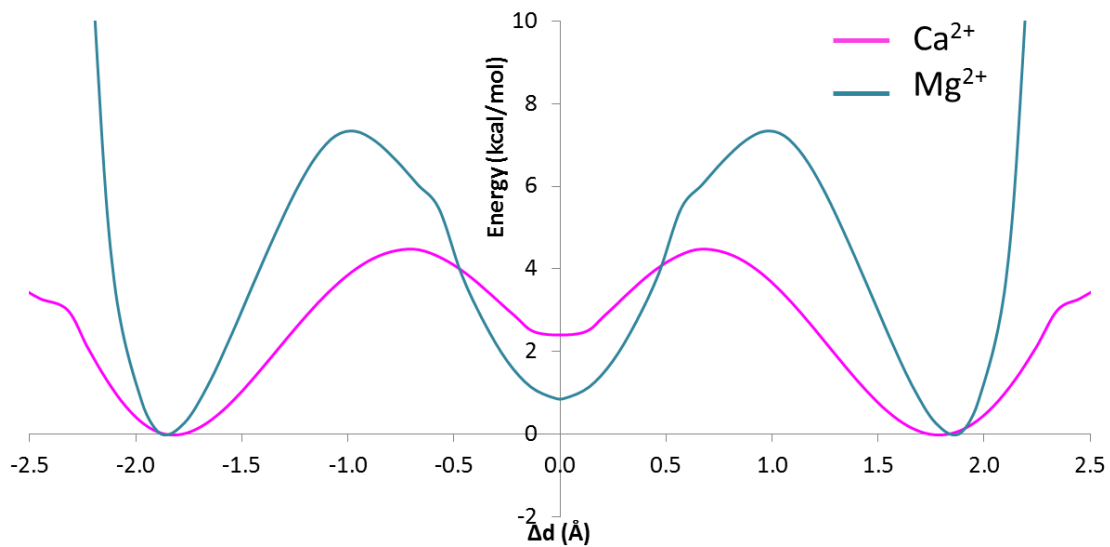


Figure 2.10: Combined Mg^{2+} and Ca^{2+} *ab initio* calculation results. Δd corresponds the difference between the distances relative to each ion of the approaching and the leaving water molecules.

To compare both graphs in the same x-axes, the energies were plotted against Δd , the difference between the fixed distance d_1 and the distance of the ap-

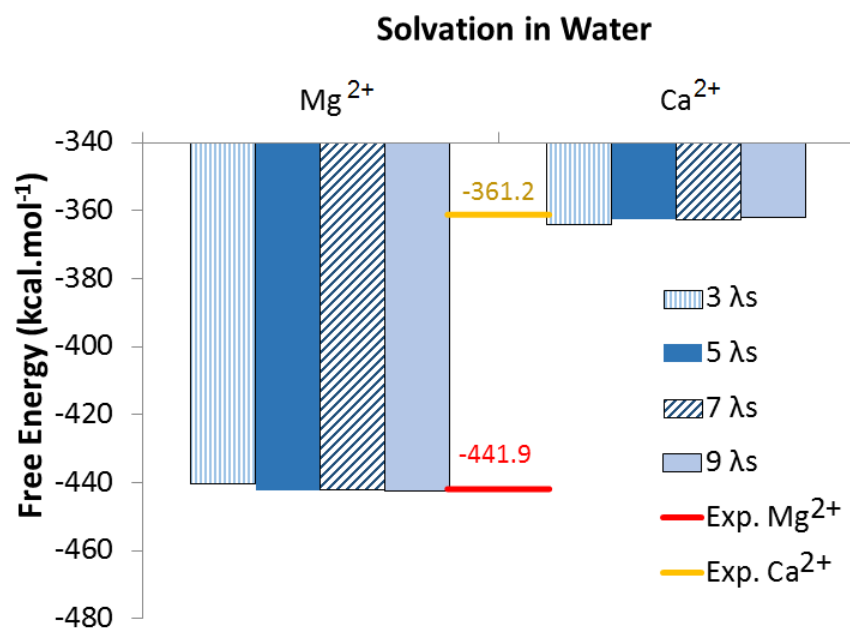
proaching water molecule d2. This shows that the energy of the intermediate state is slightly lower for Mg^{2+} than for Ca^{2+} (see position $\Delta d = 0$ in Figure 2.10). In the intermediate state of Mg^{2+} , there are fewer atoms in the coordination shell, and this leads to a lower local energy. However, the barrier to achieve this conformation from the most stable system is higher for a Mg^{2+} than for a Ca^{2+} system (for a visualization of the barrier see the vicinity of $\Delta d = 1 \text{ \AA}$ in Figure 2.10 and for the most stable system in each set see the vicinity of $\Delta d = 2 \text{ \AA}$ in the same figure). Notice that the water exchange barrier for Mg^{2+} is approximately 4 kcal.mol^{-1} bigger than that for Ca^{2+} .

Inspection of system's visual representation indicates the mechanism by which the water molecules exchange - dissociative for Mg^{2+} and associative for Ca^{2+} (Aakesson et al., 1994; Akesson et al., 1994; Brancato and Barone, 2011; Helm and Merbach, 1999, 2005). Therefore, for our systems, dissociative mechanism leads to an increased energy barrier, and associative mechanism leads to a smaller energy barrier.

2.3.2 Solvation Free Energy Of Divalent Ions in Water and Amides Solvents

The solvation free energy was calculated for Mg^{2+} and Ca^{2+} in different oxygen-donor solvents. Figure 2.11 shows the comparative results for different number of λ . When five λ -values or higher are used in the simulation, the calculated solvation free energy remains about the same compared to using other total number of λ -values (Table 2.3 and 2.4). The solvation free energies for each ion in amide is greater than in water. This indicates a higher stability of both ions in amides than in water (Fig. 2.12). The absolute experimental values for solvation free energy of Mg^{2+} and Ca^{2+} in water vary from $435.0 \text{ kcal.mol}^{-1}$ to $441.9 \text{ kcal.mol}^{-1}$ and $356.8 \text{ kcal.mol}^{-1}$ to $361.2 \text{ kcal.mol}^{-1}$ respectively

(a)



(b)

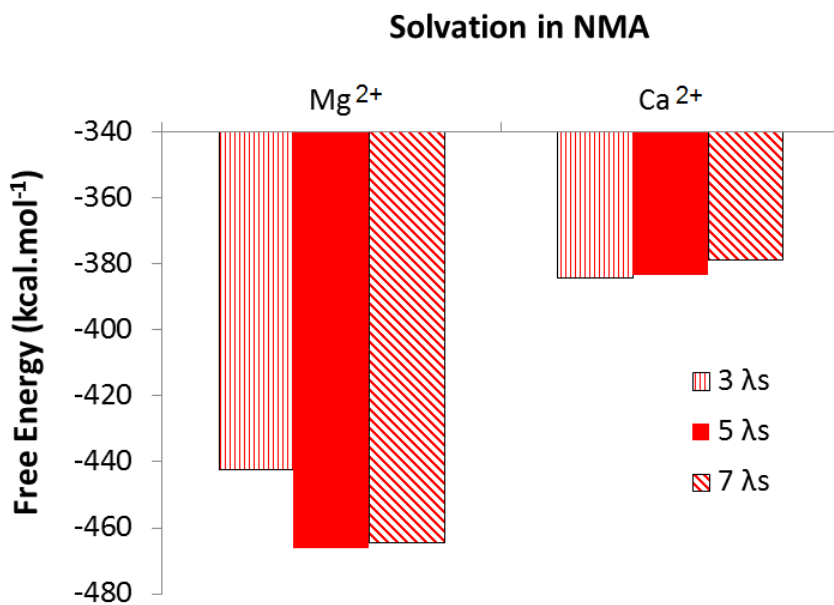


Figure 2.11: Solvation free energy calculated for different number of λ s. (a) The experimental solvation free energies for each divalent ion in water (Gomer and Tryson, 2008) is represented by the red line. (b) The solvation free energy of each divalent ion in NMA.

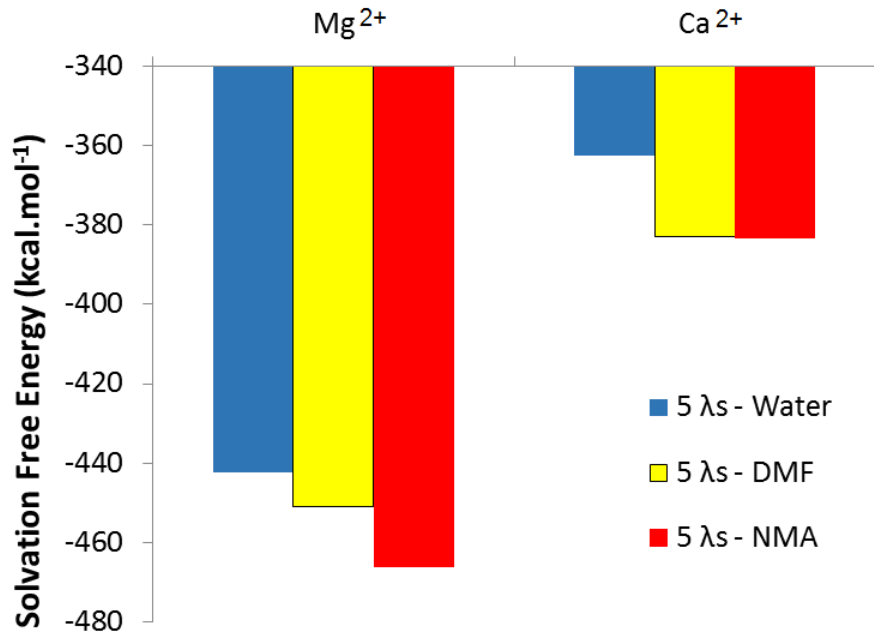


Figure 2.12: Free energy changes between water, NMA, and DMF using five λ s.

(Gomer and Tryson, 2008; Marcus, 1991; Schmid et al., 2000), giving an error smaller than of 1% and 1.7% respectively. AMBER is essentially parametrized for water interactions. Therefore a good agreement with the experimental values used for the parametrization of the force field shows that the simulation was successful.

Table 2.3: Energy (kcal/mol) for each number of λ -values for the solvation of each ion in water, for each set of simulations.

	3 λ s	5 λ s	7 λ s	9 λ s	Experimental
Solvation of Neutral Ca	-1.18	-0.94	-0.79	-0.60	
Ca \Rightarrow Ca ²⁺	-363.13	-361.49	-362.13	-361.41	
Solvation of Neutral Mg	-1.43	-1.24	-1.18	-0.98	
Mg \Rightarrow Mg ²⁺	-439.07	-441.01	-441.11	-441.56	
$\Delta G_{\text{Ca}^{2+}}^{\text{water}}$	-364.31	-362.43	-362.92	-362.01	-361.2 *
$\Delta G_{\text{Mg}^{2+}}^{\text{water}}$	-440.50	-442.25	-442.29	-442.55	-441.9*

* Gomer and Tryson (2008)

Table 2.4: Solvation free energies in kcal/mol of each divalent ion in NMA. These results are represented in 2.11b

	3 λ s	5 λ s	7 λ s
$\Delta G_{\text{Ca}^{2+}}^{\text{NMA}}$	-384.33	-383.31	-379.15
$\Delta G_{\text{Mg}^{2+}}^{\text{NMA}}$	-442.60	-466.28	-464.61

The smaller radius size of Mg^{2+} when compared to Ca^{2+} results in stronger electrostatic interactions with oxygen donors. This is confirmed by the calculated and experimental 80 kcal/mol difference in solvation free energies of these two ions in water. Different ion radii result in different steric conditions for interactions with the ion ligands. For NMA, the values obtained were -466.28 kcal/mol for Ca^{2+} and -383.31 kcal/mol for Mg^{2+} . For DMF, the values obtained were -450.10 kcal/mol for Ca^{2+} and -382.97 kcal/mol for Mg^{2+} . This results in a solvation free energy difference ($\Delta\Delta G$) of about 21 kcal/mol in solvation of Ca^{2+} and Mg^{2+} from water to NMA and about 24 kcal/mol and 8 kcal/mol for Ca^{2+} and Mg^{2+} from water to DMF, respectively. The difference in energy between ions in each solvent gives more insights than their magnitudes, because it provides grounds for stability conclusions. Thus the more negative energy in amides than in water shows a higher stability of each ion in these solvents that mimic the asparagines in our actual NMDAR model. The energy $\langle \frac{\partial V}{\partial \lambda} \rangle_{\lambda}$ was plotted against each time step for each λ . The running average window, calculated for every 100ps for each λ , was also plotted to confirm whether the calculations converged and to evaluate the results. This average removes high frequency fluctuations and emphasizes a longer time-scale run. The simulation is considered to have converged if the running average reaches a constant value, or it has a small fluctuation. For an example of a typical graph in which the energies converged, Figure 2.13 shows the time versus energy for

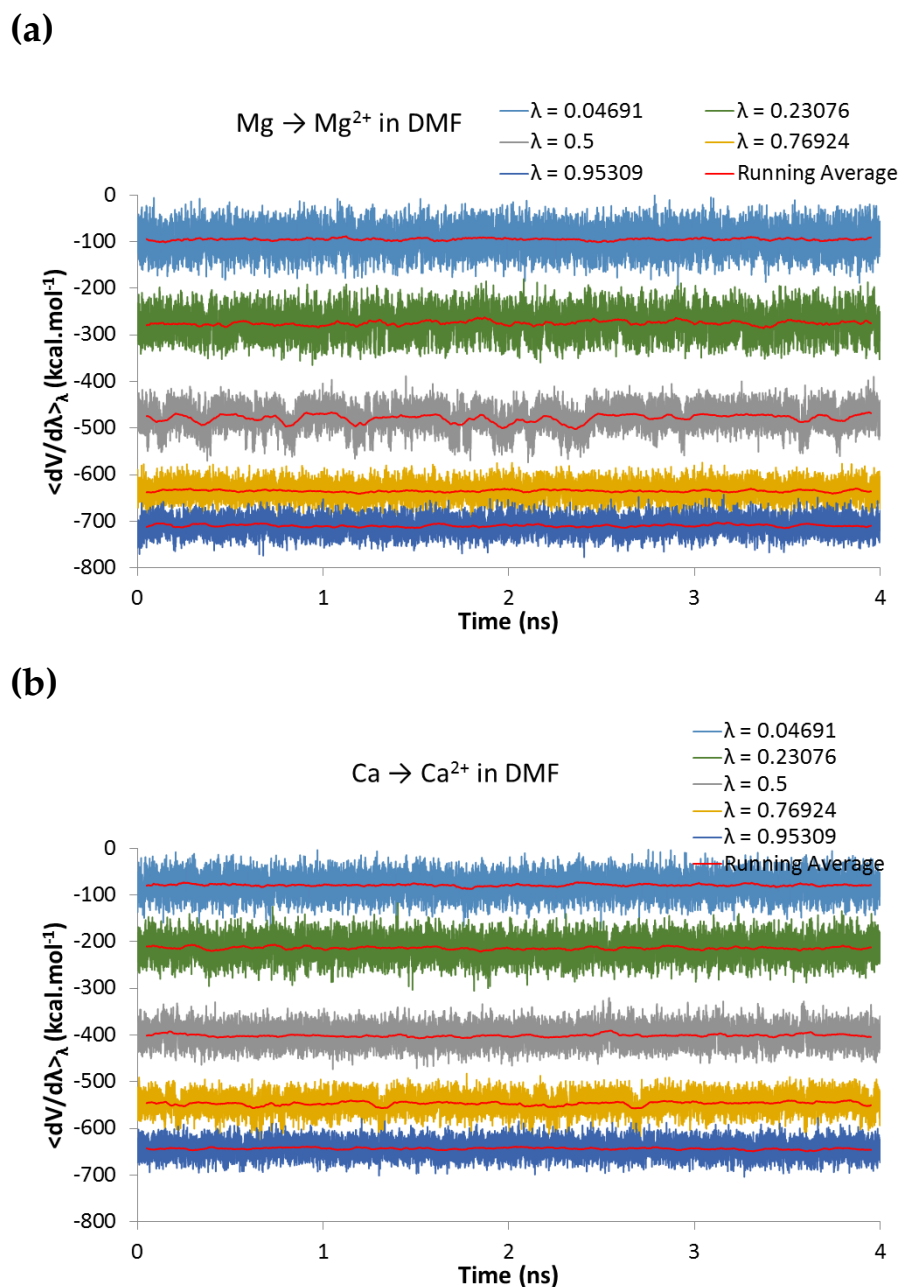


Figure 2.13: $\langle \frac{\partial V}{\partial \lambda} \rangle_\lambda$ at each time step in DMF with each of the five- λ s. The simulation was carried for 10 ns but only the last 4 ns are shown here. The red line shows a rolling window average where the window size is 100 ps. This means at each point we take a 100 ps window around it and compute the average of $\langle \frac{\partial V}{\partial \lambda} \rangle_\lambda$ of all the points within the window (a) $\langle \frac{\partial V}{\partial \lambda} \rangle_\lambda$ at each time step for Mg²⁺ in DMF for five λ -values. (b) $\langle \frac{\partial V}{\partial \lambda} \rangle_\lambda$ at each time step for Ca²⁺ in DMF for five λ -values.

each of the five λ s used in the DMF simulations. The results obtained with NMA and water also converged.

One deviation when comparing ion in the protein and ion in solution is that the molecules in solution are free to move, but in the channel the asparagines are less mobile. Mg^{2+} almost always has six ligands in its first solvation shell, while Ca^{2+} is much more permissive: six, seven, or eight Ca^{2+} -ligand complexes are common (Helm and Merbach, 2005). In the ion exchange between water and asparagines, Ca^{2+} can interact with more sites, and can therefore exchange from water to the protein with more freedom than Mg^{2+} . This was clear in the simulation of the protein itself, which is discussed in Chapter 4.

Table 2.5: Solvation free energies in kcal/mol calculated using thermodynamic integration with five λ -values. These values are represented in Figure 2.12.

	Water	NMA	DMF
$\Delta G_{\text{Ca}^{2+}}^{\text{solvent}}$	-362.43	-383.31	-382.97
$\Delta G_{\text{Mg}^{2+}}^{\text{solvent}}$	-442.25	-466.28	-450.10
$\Delta\Delta G_{\text{Ca}^{2+}}^{\text{water}\rightarrow\text{amide}}$		-20.88	-24.03
$\Delta\Delta G_{\text{Mg}^{2+}}^{\text{water}\rightarrow\text{amide}}$		-20.54	-7.85

2.3.3 Rate of Exchange

The analysis of straightforward MD simulations of each ion in different solvents complete the discussion about ligand exchange. Figure 2.16 shows the RDF results in which the distance that corresponds to the peak of the solvent- Mg^{2+} graphs are approximately at 2.0 Å and for solvent- Ca^{2+} are approximately at 2.2 Å. The position of the solvents when there is a peak in the RDF graph represents the distance of the molecules in the first solvation shell. The

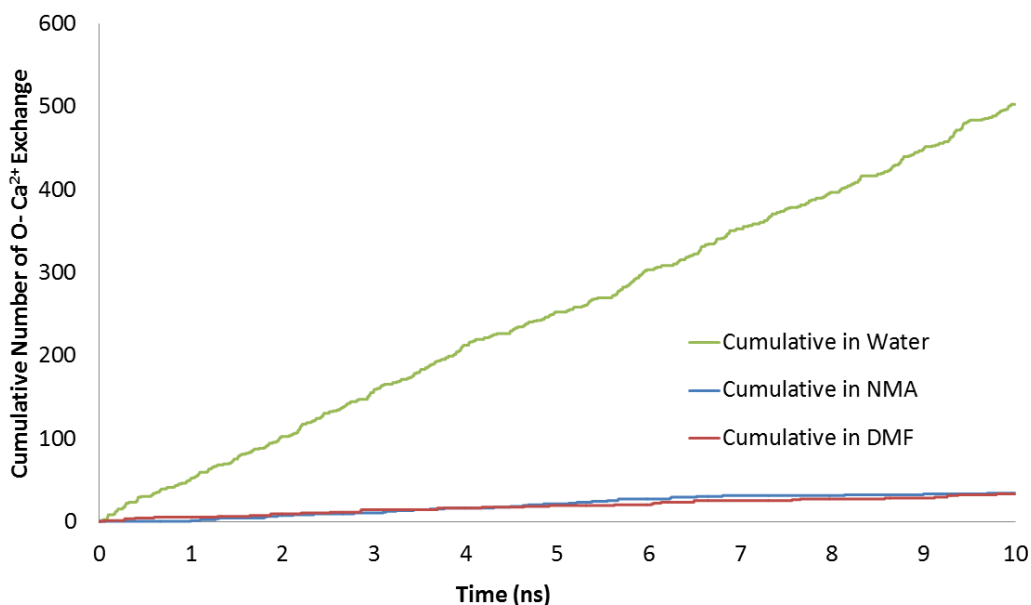


Figure 2.14: Cumulative exchange of water molecules in the first solvation shell of Ca^{2+} . This is obtained by counting for every picosecond whether there was a change in the molecules present in the first solvation shell of Ca^{2+} .

integral of the RDF shows how many molecules surround the ion given a specific distance from it. Notice that it is six for Mg^{2+} and eight for Ca^{2+} .

The exchange of the first solvation shell in bulk water was simulated using AMBER force field by monitoring how often each water molecule was exchanged in the first solvation shell. The exchange for Ca^{2+} was 50 per nanosecond, giving an exchange rate of $5 \times 10^{10} \text{ s}^{-1}$ and the exchange for Mg^{2+} was zero in the time of the simulation. The simulations with Mg^{2+} were extended for over 100 ns, and still no exchange was observed. Experimental values of rate of exchange $6.2 \times 10^5 \text{ s}^{-1}$ (Bleuzen et al., 1997; Neely and Connick, 1970) and bigger than 10^9 s^{-1} (Helm and Merbach, 2005) for Mg^{2+} and Ca^{2+} in water respectively. The rate of exchange for Ca^{2+} was closer to experimental values than for Mg^{2+} .

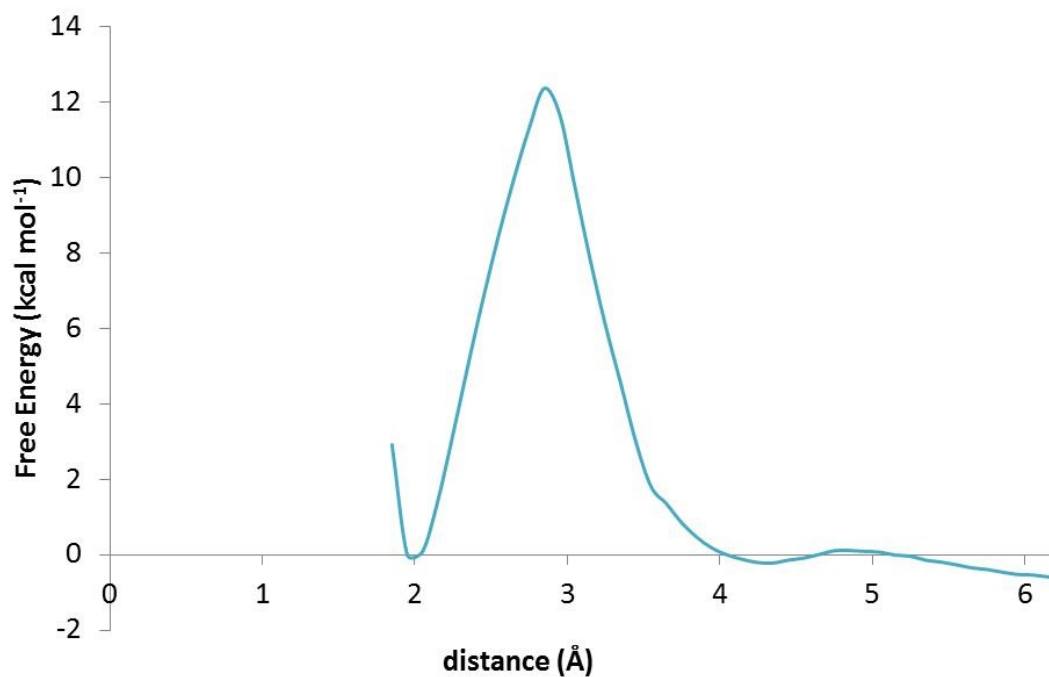


Figure 2.15: Potential of mean force of the exchange of a water molecule from the first solvation shell of Mg^{2+} . The x-axis corresponds to the distance in Å between the restrained water molecule and Mg^{2+} . This water molecule was gradually pulled from the first solvation shell. This distance was increased by applying harmonic restraints between the leaving molecule and the ion.

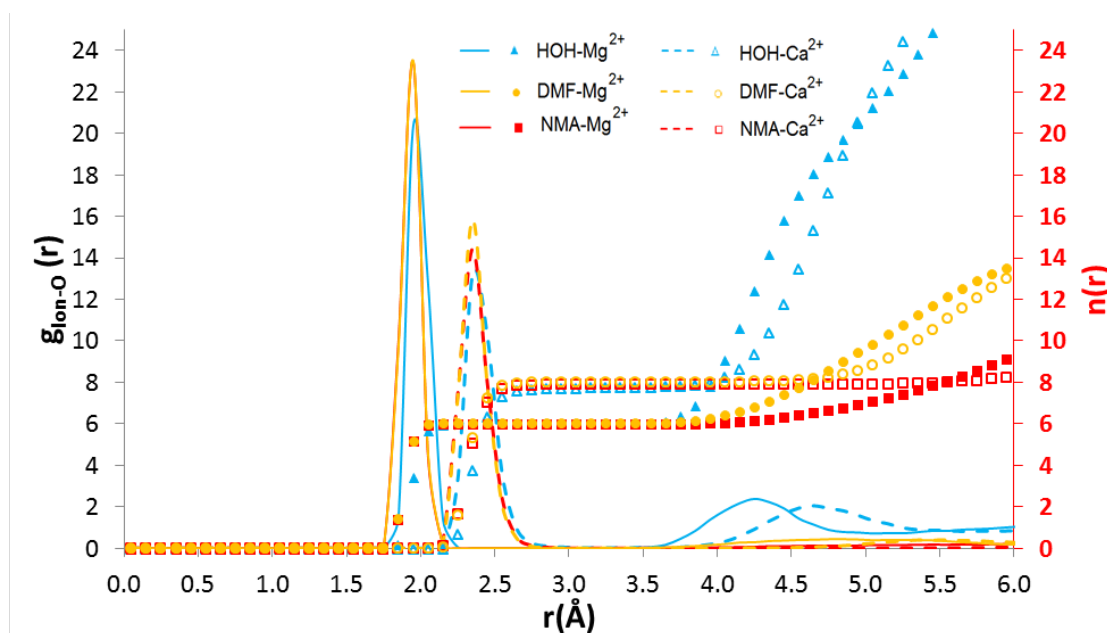


Figure 2.16: Radial distribution function of oxygen from water, NMA, and DMF with Mg^{2+} and Ca^{2+} .

Because we did not observe exchange for Mg^{2+} for any of the solvents during over 100 ns of simulation, we calculated the transition energy and rate of exchange calculated using umbrella sampling (US) (Kästner, 2011; Torrie and Valleau, 1977) unbiased by the weighted histogram analysis method (WHAM) (Chipot and Pohorille, 2007; Kumar et al., 1992, 1995; Souaille and Roux, 2001). After correcting the entropic contribution, the ΔG^\ddagger free energy barrier was 12.37 kcal/mol. Using the Equation 2.9 with the pre-exponential factor of $1.3 \times 10^{13} \text{s}^{-1}$ (Allnér et al., 2012), the rate of exchange was 1.25×10^4 - which means that the energy barrier was higher than the expected experimental one - see table 2.6.

Table 2.6: Divalent ion properties in bulk solvent.

Ion	method	ΔG^\ddagger (kcal/mol)	$k(\text{s}^{-1})$	r_1 (Å)	CN
Mg^{2+}	Standard MD	infinite		1.98	6
	Umbrella S.	12.37	1.25×10^4	1.95	
	experimental	10.0	6.7×10^5	2.07^\ddagger – 2.11^\ddagger	6^\ddagger
Ca^{2+}	Standard MD		$5 \times 10^{10}\S$	2.42	7.6
			$1.43 \times 10^{10}\P$		
	experimental		$> 10^9$	2.39 – 2.44^\ddagger	7^\ddagger

2.4 CONCLUSION

In this chapter, we discussed that polarizability is an important ion property which should be included in the calculation of properties of Mg^{2+} and Ca^{2+} . On the other hand, the molecular dynamic simulations using empirical force fields

† Ohtaki and Radnai (1993)

‡ Caminiti et al. (1979)

§ Direct count in the MD simulations

¶ Average using ptraj tool from AMBER

|| Helm and Merbach (2005)

yield reasonable free energy results. One explanation is that a total free energy calculation is not a dynamic one-to-one exchange; it averages all exchanges which makes the results more nearly reliable.

Therefore we conclude that the calculation of free energies using TI and standard force fields in bigger systems such as our NMDAR model result in reliable values. We did not find as good agreement for the rate of exchange for Mg^{2+} in water as we found for the total solvation free energy which confirms that the dynamic exchange mechanism needs a correction. We will explore possible corrections in a future paper.

The smaller size of Mg^{2+} when compared to Ca^{2+} results in stronger electrostatic interactions. We believe that this influences the NMDAR permeation model, in which the faster exchange of ligands and the more flexible coordination number in the coordination shell of Ca^{2+} compared to Mg^{2+} allows the permeation of Ca^{2+} .

MODELING NMDA RECEPTORS

3.1 INTRODUCTION

In the previous chapter, we discussed our findings on how Ca^{2+} and Mg^{2+} interact with an environment similar to what these ions encounter when crossing an NMDAR channel. Although this discussion sheds some light on the NMDAR permeation mechanism, accurately simulating the actual channel environment is crucial for a fuller understanding of the selectivity between Ca^{2+} and Mg^{2+} . To simulate an ion in the channel, it is best to work from the complete all-atom protein structure. However, the detailed atomic architecture of an intact NMDAR is currently unknown. This chapter focuses on the non-trivial task of creating a realistic model of the domain of the protein that controls ion permeation: the transmembrane domain (TMD).

AMPA and NaK are possible Templates for NMDAR Model

In order to build an atomic model of the NMDAR TMD, we used *Homology modeling*, a tool for 3D model prediction. Homology modeling is widely used when the crystal structure of a protein is not available (Becker et al., 2001). A calculated 3D model can be obtained by comparing an unknown structure (the

target) with one or more related proteins with known structures (the *templates*). First, this comparison begins by aligning similar residues within the two or more primary structures. Then, once the corresponding residues are aligned, the 3D model of the target is obtained by minimizing the difference between the spatial position of these residues in the target and the template(s).

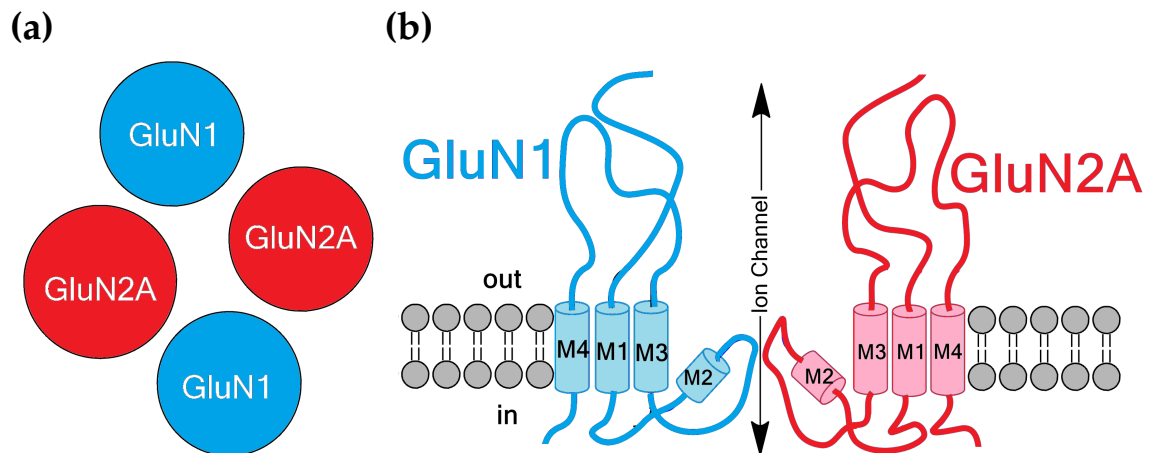


Figure 3.1: Schematic representation of the NMDAR transmembrane domain subunits. (a) An schematic top view of the four subunits arranged as GluN₁-2A-1-2a is represented. (b) Two of the NMDAR subunits, GluN₁ and GluN_{2A}, are represented. The regions M₁, M₂, M₃, and M₄ are represented.

Proteins that are likely evolutionarily related are *homologous*. The shared evolutionary ancestors usually reflect structural similarity (Becker et al., 2001). Therefore, a homologous protein with known structure may act as a template for 3D structure modeling of an unknown structure. Among iGluR subfamilies, an x-ray AMPAR structure published by Sobolevsky et al. (2009) is available and could be used as a template to NMDAR model. These two iGluR subfamilies share a common structural design: both have four subunits, each one with at least four domains. One of these domains is the transmembrane domain (TMD), that has four transmembrane helices (M₁, part of M₂, M₃ and M₄ –see Fig. 3.1). The extended region that lines the pore is the non-helical por-

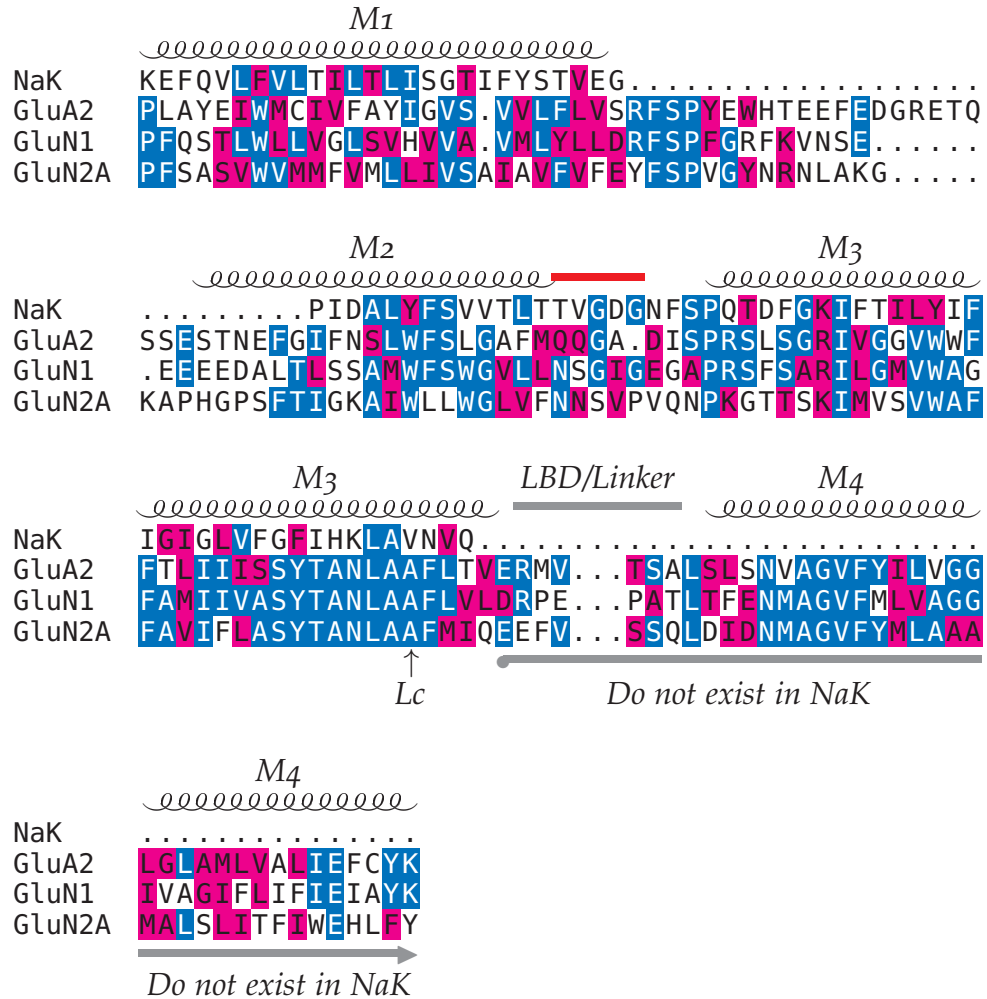


Figure 3.2: Alignment of NaK channel, AMPAR (GluA), and NMDAR (GluN₁ and GluN_{2A}) transmembrane domains. Identical residues are blue shaded and similar but not identical are red shaded. M₁, M₂, M₃, and M₄ are marked. The non-helical part of M₂ is marked as a red bar. The position of the Lurcher mutation discussed in this thesis is marked with an up arrow. NaK channel does not have the equivalent of M₄. The ligand binding domain (LDB) and linker residues are between M₃ and M₄. LDB and linker are not listed in this figure.

tion of M₂. AMPAR subunits (such as GluA) form functional homotetramers, whereas NMDARs are obligate heterotetramers: they form channels containing two glycine-binding GluN₁ subunits and two other subunits, either from the glutamate-binding GluN₂ (2A, 2B, 2C, 2D) or the glycine-binding GluN₃ (3A

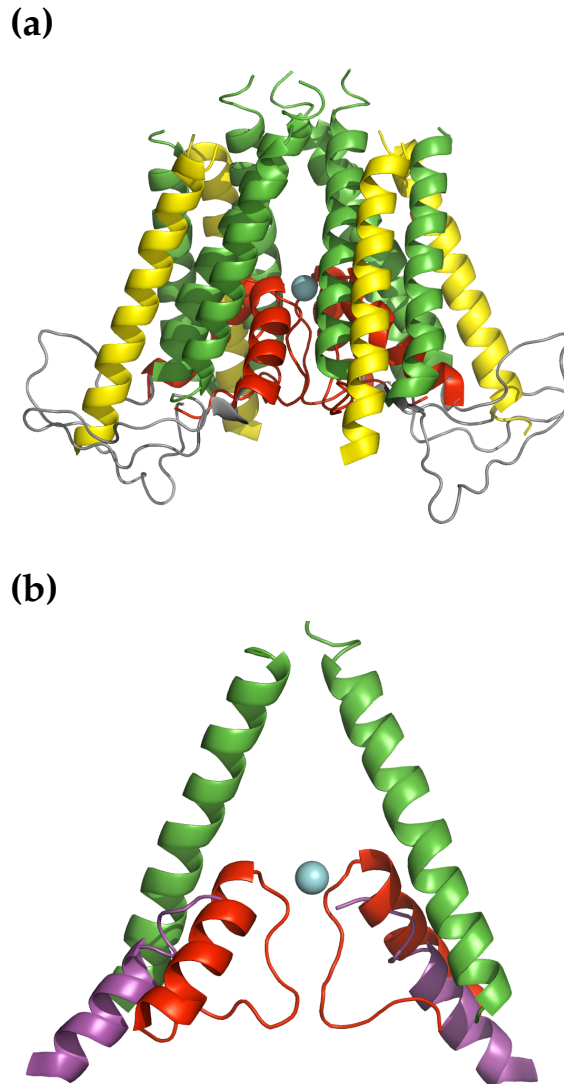


Figure 3.3: The overall NMDAR model color coded according to how the model overlaps NaK and AMPAR templates. An ion is represented in the core of the protein as a cyan sphere. (a) Green corresponds to the regions that exist in the three structures and were well resolved in AMPAR and NaK structures, yellow to the regions that exist only in NMDAR and AMPAR, red to the regions that exist in the three structures but were not well resolved in AMPAR published crystal structure (Sobolevsky et al., 2009). The gray loops were not based in any template. (b) This figure shows the M3 and M2s of GluN1 only. The magenta regions are the M2s from the AMPAR published crystal structure after the M3s from AMPAR and NMDAR model were superimposed. Notice that the selectivity filter is missing and how the M2s would be lower in space compared to the M2s in red. The positioning represented in magenta does not allow the selectivity filter to form a binding cage that can surround an ion.

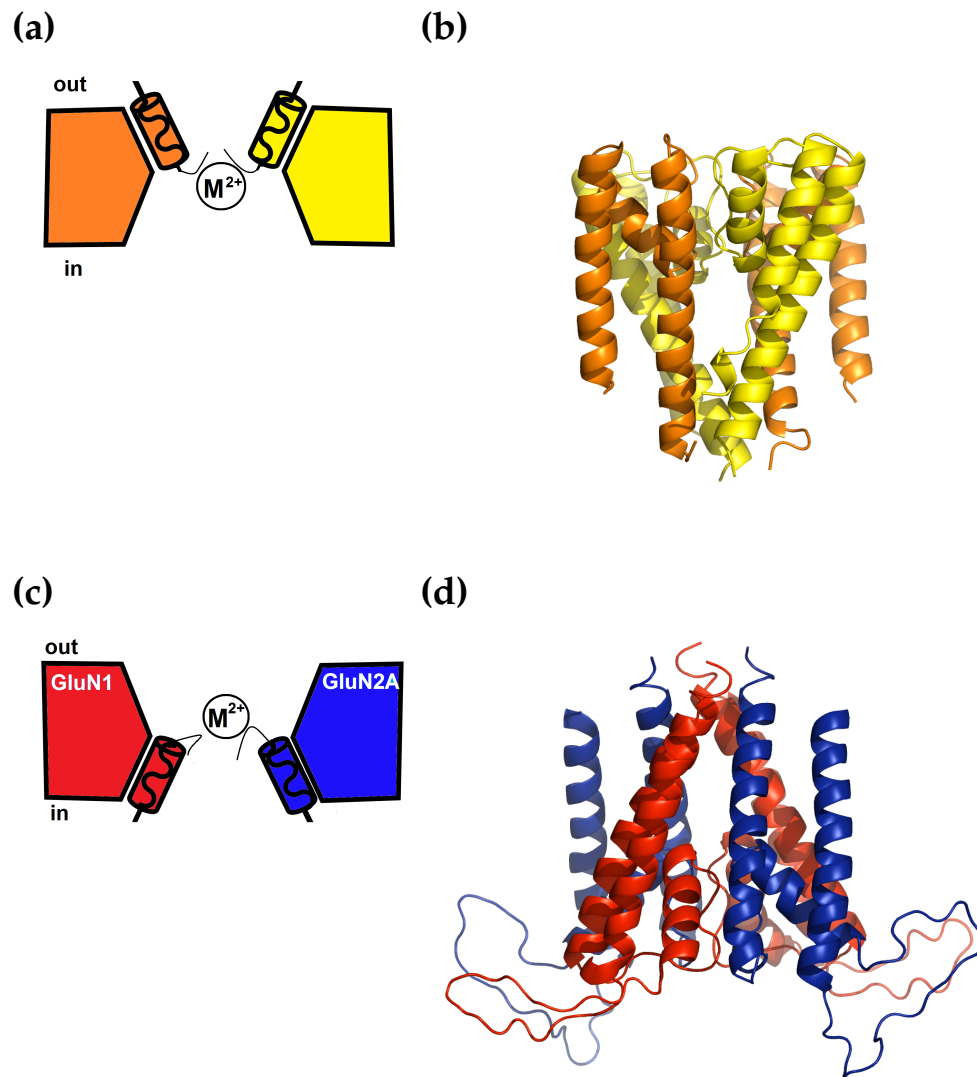


Figure 3.4: NaK and NMDAR equivalent helices. (a) A cartoon that represents the narrowest part of a NaK channel. A generic divalent ion M^{2+} is represented in the center of the figure. (b) The side view of NaK is equivalent of an inverted NMDAR. (c) A cartoon that represents the narrowest part of a NMDAR channel. A generic divalent ion M^{2+} is represented in the center of the figure. (d) Representation of the NMDAR overall structure side view without the M_4 s.

Table 3.1: Percentage of similarity and identity between NaK channel, AMPAR (GluA), and NMDAR (GluN₁ and GluN_{2A}). The identity percentages correspond to the proportion of identical residues identified in Figure 3.2 and the similarity percentage corresponds to the residues identified as similar in the same alignment.

	NaK	GluA2	GluN ₁	GluN _{2A}	
NaK	—	41.0	41.7	32.5	% simil.
GluA2	15.3	—	61.5	54.2	
GluN ₁	17.7	37.6	—	59.7	
GluN _{2A}	12.5	29.2	29.4	—	

% identity

or 3B) subfamilies. Despite their difference in terms of being homomeric or heteromeric, the residue similarity is sufficient for modeling the TMD region. The TMD of GluA2 is about 62% and about 54% similar with GluN₁ and GluN_{2A}, respectively – see the alignment in Fig. 3.2 and the percentages in Table 3. See also reviews about AMPAR, NMDAR, and other iGluRs by [Dingledine et al. \(1999\)](#); [Traynelis et al. \(2010\)](#). The alignments presented here were discussed by [Sobolevsky et al. \(2009\)](#) and [Retchless et al. \(2012\)](#).

Despite AMPAR and NMDAR sequence similarities, part of the available AMPAR crystal structure is poorly resolved and thus this region is unreliable to be used as a template for our NMDAR 3D modeling. The poorly resolved region corresponds to M2 helix and selectivity filter. *Selectivity filter* is the ion channel region in which ion selection happens. In NMDARs, the selectivity filter corresponds to the loops that connect M2 and M3 helices - see Fig. 3.1. The helical region of M2 AMPAR crystal structure ([Sobolevsky et al., 2009](#)) had a weak electronic density and perhaps an incorrect positioning ([Retchless](#)

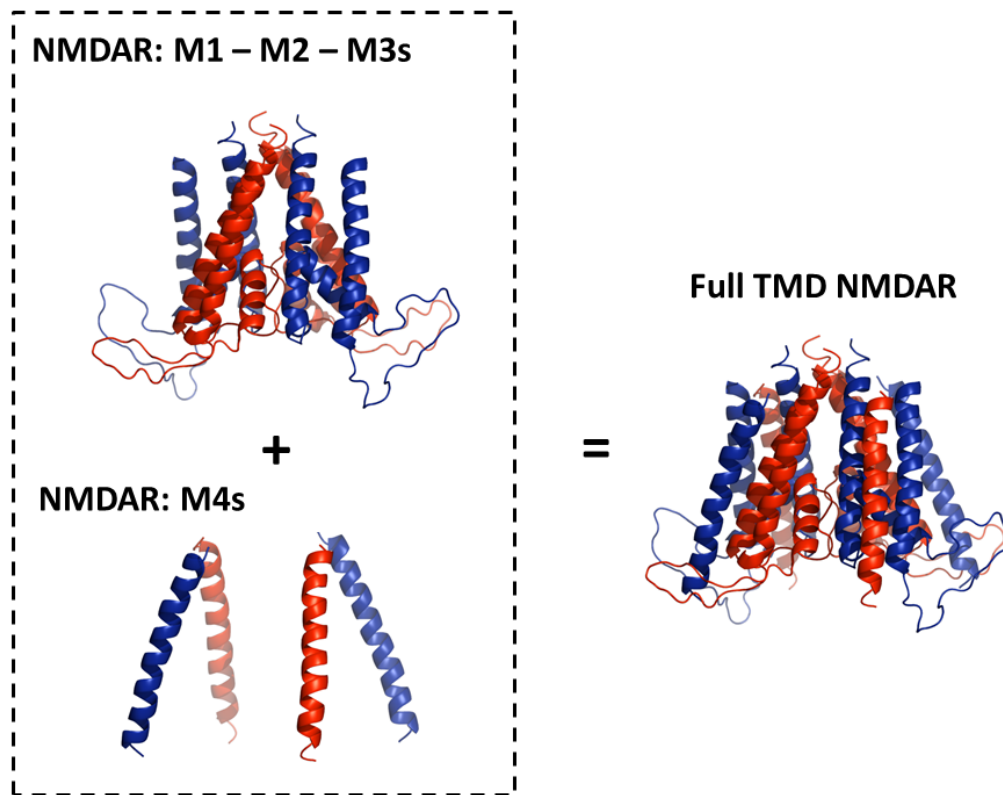


Figure 3.5: The addition of the M4s to the modelled M1 -M2 -M3 structure provides a full transmembrane domain model.

et al., 2012). More importantly, the extended region of M2, which lines to pore, was not resolved at all. The M2 unreliable placement means that even if one models the selectivity filter loops using available software, these loops would be questionably placed due to their position being based on an uncertain M2 helical positioning. Although a recent work has used AMPAR as the NMDAR template (Dai and Zhou, 2013), the overall goal of that work was to simulate the gating mechanism, and not to carefully model the ion channel selectivity region as it is in our work. On the other hand, in order to study the physiology of the channel, we needed to build a TMD NMDAR model that agrees with

experimental results for the positioning of the region involved in the selectivity mechanism.

An alternative that we used was to search for another template from another family of ion channels. Cyclic nucleotide-gated channel and potassium channels (that from now on will be referred as non-iGluR) have an overall TMD structure which is very similar to an inverted iGluR: the side of the NMDARs where the M2 enters and exits the membrane faces the inside of the cell, while equivalent site in the K⁺ and cyclic nucleotide-gated channel's pore face the outer part of the cell, as an inverted tepee or an upside-down NMDAR (Doyle et al. (1998) – see Fig. 3.4). These structural similarities occur because these non-iGluR channels are probably evolutionary related to iGluRs (Kuner et al., 2003; Shi et al., 2006; Wood et al., 1995). The previous discussed non-iGluR channels are less similar to NMDARs than among iGluRs (Table 3.1) and correspond to M₁, M₂, and M₃s only, with no correspondent M₄. Nevertheless, one of the non-iGluR subfamilies stand out: NaK is permeable to Ca²⁺, and thus the most similar to NDMAR in terms of permeation features (Alam et al., 2007). Moreover, NaK has a well-resolved crystal structure (at 2.8 Å resolution - Shi et al. (2006)). The overall structure and functional similarities make the NaK channel a reasonable alternative basis for the template of M₁, M₂, and M₃, while using AMPAR for the M₄s – see Fig. 3.5.

SYTANLAAF is an Important Conserved iGluR Motif

An important iGluR region in our homology model that also deserves careful attention is a conserved sequence of residues: SYTANLAAF. This motif is located at the extracellular region of M₃, and is involved in gating (Murthy et al., 2012). When studying this motif or nearby residues, a convention is to

number the residues relative to the initial motif residue (S). For example, the first alanine in the SYTANLAAF motif is A+3, the second is A+6, and the third is A+7. In this motif, there is a mix of polar and non-polar residues, whereas most of the TMD NMDAR residues are hydrophobic. This larger proportion of hydrophilic residues on the extracellular region of M₃s is expected because this is a region that is exposed to the hydrophilic aqueous environment.

Lurcher Mutations Shift Equilibrium Toward Open State

Multiple studies show the effect of mutations in the SYTANLAAF conserved motif in different iGluR subfamilies (Blanke and VanDongen, 2008; Jones et al., 2002; Kohda et al., 2000; Murthy et al., 2012; Yuan et al., 2005). These mutations are called *Lurcher mutations* (Jones et al., 2002). When A+7 is mutated to a residue that adds a bulky side chain, the channel equilibrium shifts toward an open state (Kohda et al., 2000; Murthy et al., 2012; Taverna et al., 2000). For example, when A+7 is mutated from alanine to tyrosine (Zuo et al., 1997), the side chains are changed from hydrophobic to a bulkier uncharged polar (hydrophilic) side chain. This observation was key to resolving stability problems within our TMD NMDAR model, which will be discussed later. The site A+7 corresponds to the sites A635 in GluN1 and A632 in GluN2A when the residues are numbered from the first aminoacid in the full protein (see Traynelis et al. (2010) for a review on iGluRs including their numbering).

This chapter focuses on the simulation approach used to reproduce this realistic standalone TMD NMDAR model and its equilibration in the presence of explicit membrane and water. In Chapter 4, we use this model to study the behavior of Ca²⁺ and Mg²⁺ in the channel.

3.2 METHODOLOGY

In summary, first, M₁, M₂, and M₃ regions of NMDAR were previously modeled using a combination of experimental studies and homology modeling (Retchless et al., 2012). Then, M₄s were built and added to the M₁-M₂-M₃ model. Finally, this full TMD NMDAR model was inserted in membrane and water. The protein was then mutated in a position that guaranteed the stability of the model without affecting the ion binding site. The details of each step are described in the following subsections.

3.2.1 Modeling the Transmembrane Domain

The Initial M₁-M₂-M₃ TMD NMDAR Homology Model was Based on NaK

A structural homology model of the NMDAR M₁-M₂-M₃ region was created by Retchless et al. (2012) based on the crystal structure of a closed NaK channel (PDB: 2AHY - Shi et al. 2006). Their primary sequence alignment agreed with previous published alignments (Beck et al. (1999); Panchenko et al. (2001); Tikhonov (2007); Tikhonov et al. (2002) – see Fig. 3.2). That model had a GluN₁-2A-1-2A subunit arrangement, in agreement with the most recent literature (Sobolevsky et al., 2009).

For further modeling, we used HARLEM (Kurnikov, 1999) using AMBER 10 force field (Li and Brüschweiler, 2010; Lindorff-Larsen et al., 2010). For equilibration and production runs we used the same force field in the AMBER 12 package (Case et al., 2012) using the GPU accelerated code (Gootz et al., 2012; Salomon-Ferrer et al., 2013).

M4s Based on AMPAR Were Added to Our Initial NMDAR Model

The Mg^{2+} was positioned among the asparagines from the selectivity filter with the same distance between ion and each side chain oxygen. These distances were constrained to reproduce the 2 Å Mg^{2+} -oxygen donor distance obtained in Chapter 2.

We minimized the energy of this initial Mg^{2+} -homology model without M4 helices to find a stable structure. The M4 region was then modeled based on the published alignment and structure of the AMPAR (Sobolevsky et al., 2009), using HARLEM (Kurnikov, 1999). The M4 backbone positions corresponded to the ones in AMPAR (3KG2 pdb file). Each M4 AMPAR residue side chain was regrown to the ones in GluN1 and GluN2A, creating 2 different targets. An energy minimization followed every three residue change.

To position the M4s, AMPAR and NMDAR helices were overlapped following Sobolevsky et al. (2009) suggestions: A/C AMPAR chains are equivalent to GluN1s and B/D to GluN2As. M1 and M3 helices were used to 3D overlap AMPAR and the NMDAR model and then M4s were positioned. We minimized the energy of the complete model from 10,000 steps to remove any bad contacts between residue side chains. Thereafter we ran 1.2 ns of MD simulation while restraining the α -carbon using harmonic potential $V(\vec{r}) = \frac{1}{2}k(\vec{r} - \vec{r}_{eq})^2$ with force constant 2 kcal.mol⁻¹Å⁻². After this procedure was performed, we confirmed the stability and equilibration of the full TMD NMDAR model by checking the values for root mean square fluctuation (RMSF) and root mean square deviation (RMSD). Both measure the average distance between selected atoms and a reference model. For RMSF, the reference is the average position of each residue. For RMSD, the reference structure was the full TMD NMDAR homology model.

The Full TMD NMDAR Model was Placed in Membrane and Water

This full, wild-type, TMD NMDAR model was placed in a well-equilibrated lipid membrane and in water. The parameters for the membrane lipids (Berendsen and Tieleman, 1998; Kukol, 2009) were obtained from GROMACS force field. These parameters were recomputed in our group to be used in AMBER force field. A patch of water molecules was added to the cavity of the NMDAR model. Any membrane or water molecules that overlapped the protein were erased. After placement, 300,000 steps of energy minimization and no more than 2 ns of constant pressure MD simulations were carried out in which the water molecules and protein backbone were harmonically restrained with a force constant of $20 \text{ kcal.mol}^{-1}\text{\AA}^{-2}$. The final full system had 10159 water molecules, 108 DMPC membrane lipids, and 534 protein residues.

3.2.2 Equilibration and Production Run

Any further simulations in this chapter and in Chapter 4 were all-atom molecular dynamics simulations in explicit TIP3P water solvent (Jorgensen et al., 1983), using AMBER 10 force field (Li and Brüschweiler, 2010; Lindorff-Larsen et al., 2010) in the AMBER 12 package (Case et al., 2012). We performed these simulations using the GPU accelerated code (Gootz et al., 2012; Salomon-Ferrer et al., 2013) with an integration time step of 1 fs with all temperatures maintained at 300K by a Langevin thermostat (Adelman and Doll, 1976). Periodic boundary conditions and all atom wrapping were also imposed for all simulations. Long range electrostatics were calculated with Particle Mesh Ewald (PME) (Darden et al., 1993). The Van der Waals cutoff distance was 12 Å.

The initial equilibration attempt was of the wild-type TMD NMDAR model acquired from previous section steps. To equilibrate this model, the hydrogen

bonds and the dihedral angles of the helices were harmonically restrained with a force constant of $20 \text{ kcal.mol}^{-1}\text{\AA}^{-2}$ for 25 ns. The strength of the restraints was gradually reduced to $6 \text{ kcal.mol}^{-1}\text{\AA}^{-2}$ for 25 ns, and $2 \text{ kcal.mol}^{-1}\text{\AA}^{-2}$ for 100 ns. The production run was performed without restraints for 100 ns. Therefore, a total of 250 ns of constant pressure and temperature simulations were performed. See Fig. 3.6 for a pictorial representation of the restrained distances and angles, and Appendix B for the restraining scripts for AMBER.

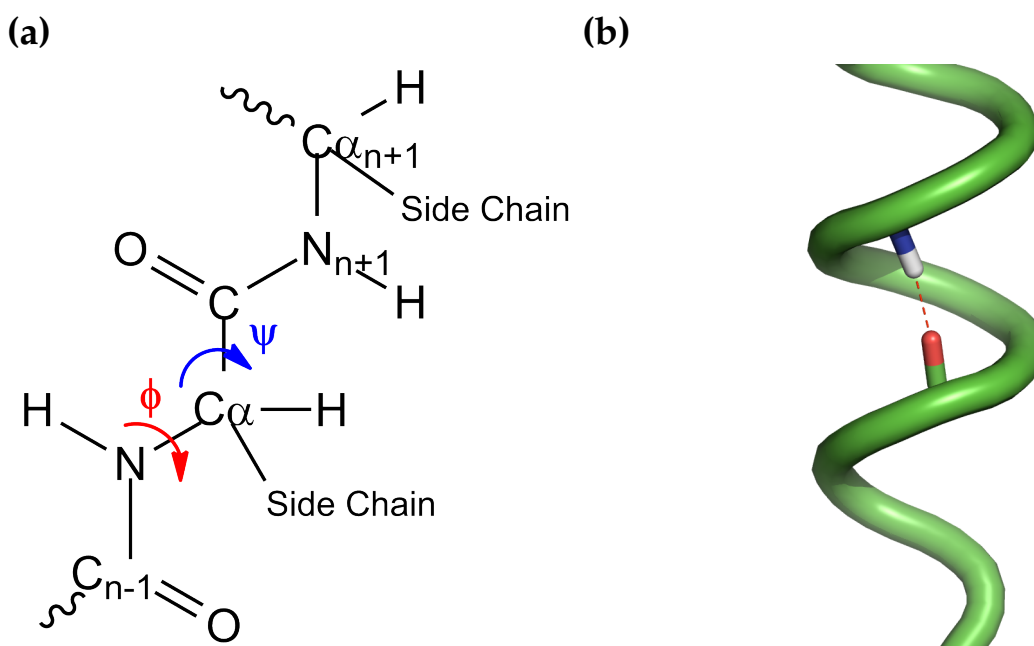


Figure 3.6: A pictorial representation of the restrained distances and angles. (a) The ψ and ϕ dihedral angles were harmonically restrained. (b) The h-bonds were also restrained in the helical regions of the TMD NMDAR model. Here an h-bond is represented as a red dotted line.

This initial model of the wild type of GluN₁/GluN_{2A} simulation unfolded after 200 ns of simulation. This happened very likely because the model does not have the ligand binding domain that stabilizes the M₃ regions as it does in nature. Due to the remaining hydrophobic residues on the extracellular region

of the M₃s, these helices bent because they were in direct contact with water with no upper structure to stabilize them, leading the protein to unfold.

This issue led us to use a Lurcher mutation that changes the residues to hydrophilic ones, and hence stops the collapse of the simulation. The A+7 residues were mutated in all subunits to tyrosine to decrease the hydrophobicity in the extracellular region of the M₃s. This Lurcher mutation increases probability of the channel to be in open state, allowing ions to permeate. If the M₃ part of the TMD structure strongly depends on the ligand binding domain, by making the mutant we obtained a more stable structure. The mutant NMDAR is functional. See Fig. 3.8 for a visualization of the hydrophobic/hydrophilic regions on the extracellular region of the M₃s after the mutation.

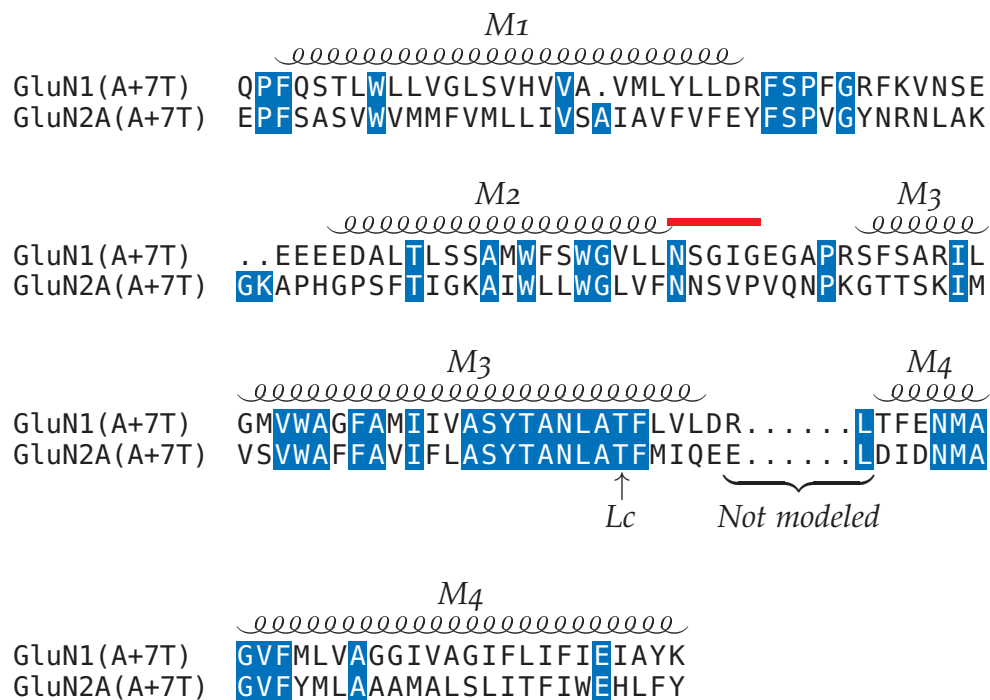


Figure 3.7: Alignment of the residues present in our TMD NMDAR model. Identical residues are blue shaded. The Lurcher mutation A+7T is marked by an up arrow.

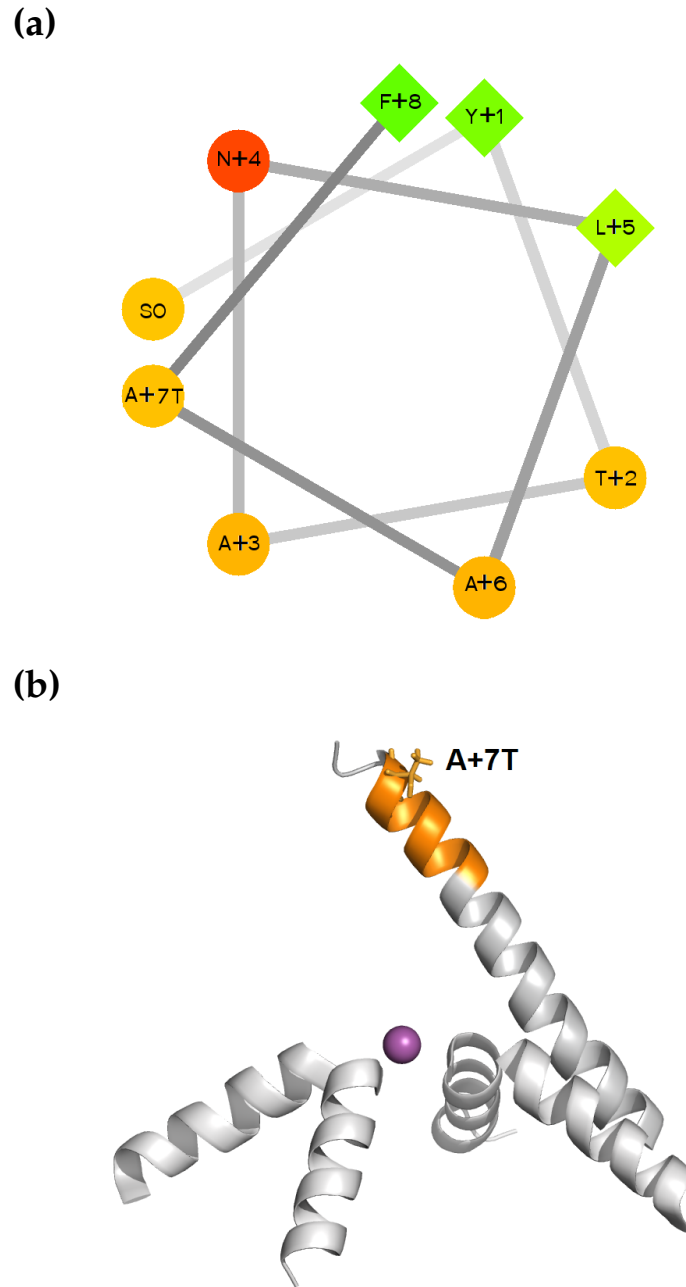
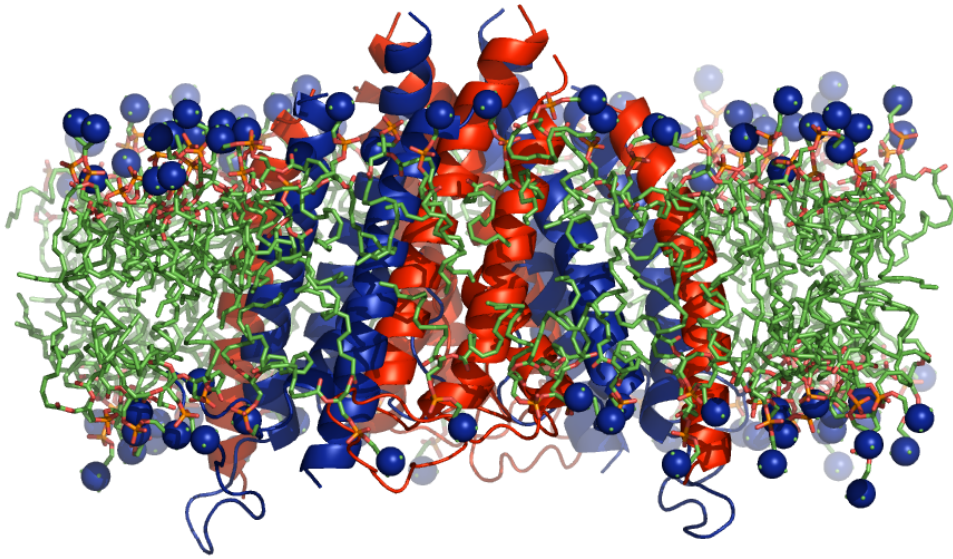


Figure 3.8: Representations of the conserved SYTANLAAF motif mutated to A+7T. (a) In this wheel representation, hydrophilic residues are circles and hydrophobic residues are diamonds. Hydrophobic residues are green, and the amount of green is decreasing proportionally to the hydrophobicity, with zero hydrophobicity coded as orange, and pure red being the most uncharged hydrophilic residue. (b) One of the M₃ helices and the four M₂ helices are represented as cartoon. The purple circle is the ion placed relative to these helices in the selectivity filter. The SYTANLA(A+7T)F motif is the orange portion of the represented M₃ helix. The mutated A+7T residue is marked.

(a)



(b)

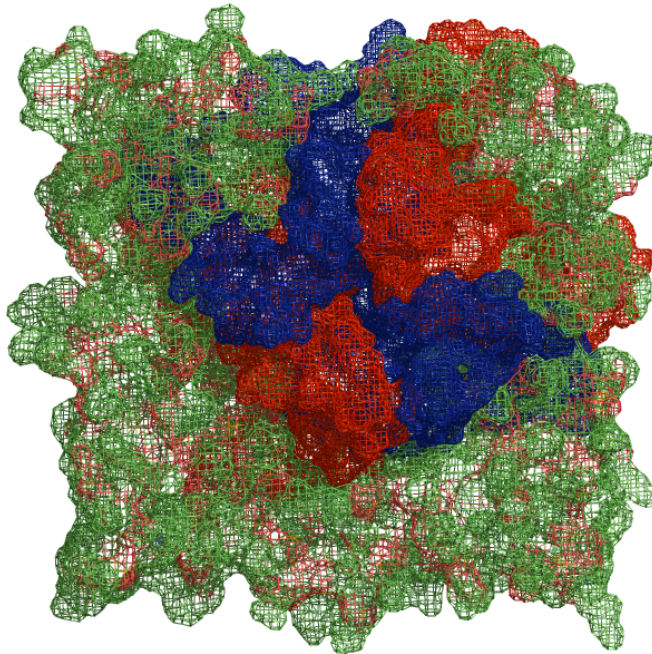


Figure 3.9: The NMDAR model placed in the membrane and water. Here the water is not represented. (a) The side view of our TMD NMDAR model in the membrane shows the position of the protein model with respect to the membrane. The nitrogen atoms in the lipid molecules are represented as dark blue spheres. (b) The mesh representation of the top view of our system. GluN1s are represented in red, GluN2As in blue, and everything else is the membrane. This figure corresponds to the last snapshot at 250 ns of simulations and shows that our model was well-packed against the membrane.

Two structures of the mutated TMD NMDAR model with either Mg^{2+} or Ca^{2+} were equilibrated following the same protocol described for the wild-type model. The overall size of the resulting systems was approximately $90 \text{ \AA} \times 70 \text{ \AA} \times 90 \text{ \AA}$.

To analyze the structure fluctuation during the MD simulations and assess the relative mobility of the residues we computed the RMSF for the α -carbons for each residue. We also computed the RMSD with respect to the α -carbon position in our initial non-equilibrated homology. RMSDs show how a structure evolves and changes in time, and hence whether the equilibration of the protein was achieved. Additionally, we computed the *helicity* of the NMDAR helices. Helicity is a percentage of the residues in the helical regions that stayed as helices throughout the simulation. In summary, RMSD, RMSF, and helicity show the stability of the model and allow for comparison of the protein behavior with the different ions in its core, as it will be discussed in the next section.

3.3 RESULTS AND DISCUSSION

3.3.1 TMD NMDAR Model in Vacuum

We first ran a short equilibration of the standalone TMD NMDAR model in order to avoid over-equilibration of the system in vacuum, but still eliminate steric clashes due to the positioning of M4s. These simulations were analyzed using root mean square deviation (RMSD) with respect to the initial step, as well as root mean square fluctuation (RMSF). The calculated RMSF shows that the simulated TMD NMDAR model has a higher flexibility average on the loops and on the terminal residues, as expected. This flexibility is shown in

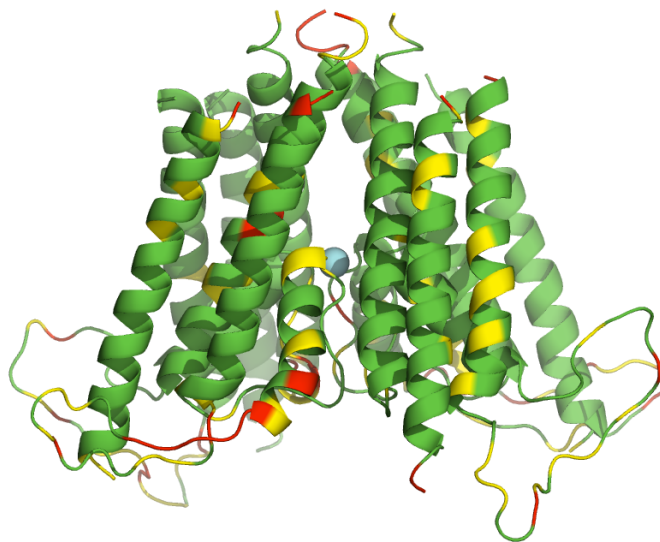
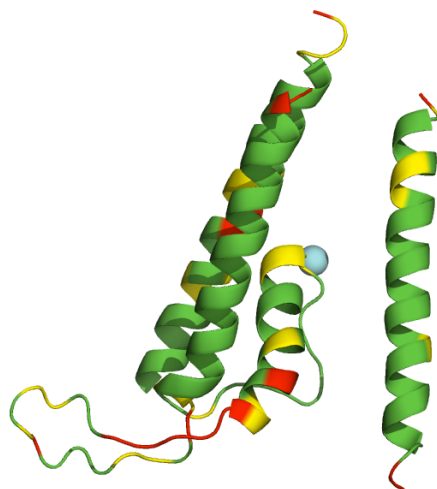
(a)**(b)**

Figure 3.10: NMDAR RMSF for the equilibration in vacuum. The backbone is colored according to RMSF value: green is for $\text{RMSF} < 1.0\text{\AA}$, yellow is for $1.0\text{\AA} < \text{RMSF} < 2.0\text{\AA}$, and red is for $\text{RMSF} > 2.0\text{\AA}$. **(a)** NMDAR **(b)** Chain D of NMDAR

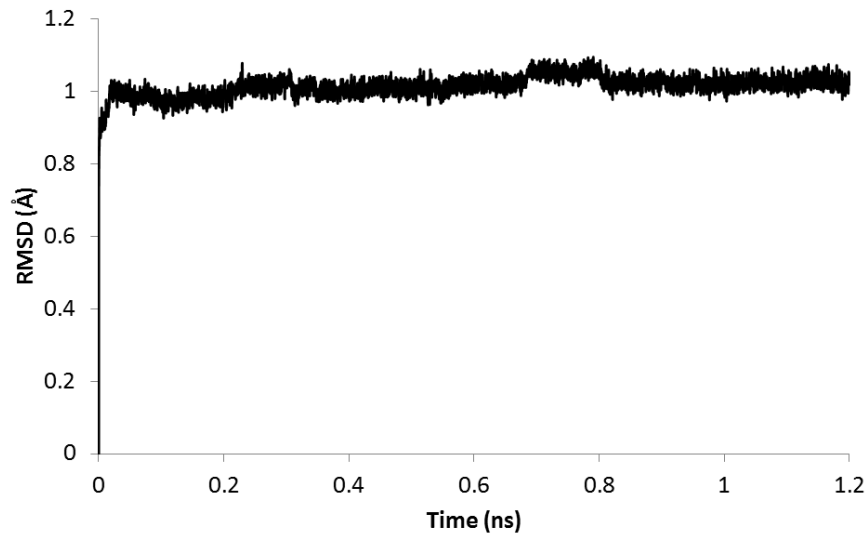


Figure 3.11: RMSD for 1.2 ns of equilibration of the homology NMDAR model in vacuum.

Figure 3.10, where the protein backbone is colored according to the degree of the exhibited motion. The RMSD, shown in Figure 3.11, indicates that the deviation of the structure from its initial configuration during the vacuum simulation is not extreme, being at most 1 Å. Therefore the RMSF and RMSD of the TMD NMDAR model, before being inserted in the membrane and water, indicate that the model is stable.

3.3.2 TMD NMDAR Model in Membrane and Water

Stability of the Model

In this section we discuss the simulations on the full TMD NMDAR model placed in membrane and water. The total α -carbon RMSDs evaluate how much the full structure with either Ca^{2+} or Mg^{2+} in its binding site deviates from the initial homology model in each time step. They indicate that the initial full TMD NMDAR model placed in the membrane and water deviates from the initial homology model by 1.4 Å (Fig. 3.12). This total RMSD increases up to

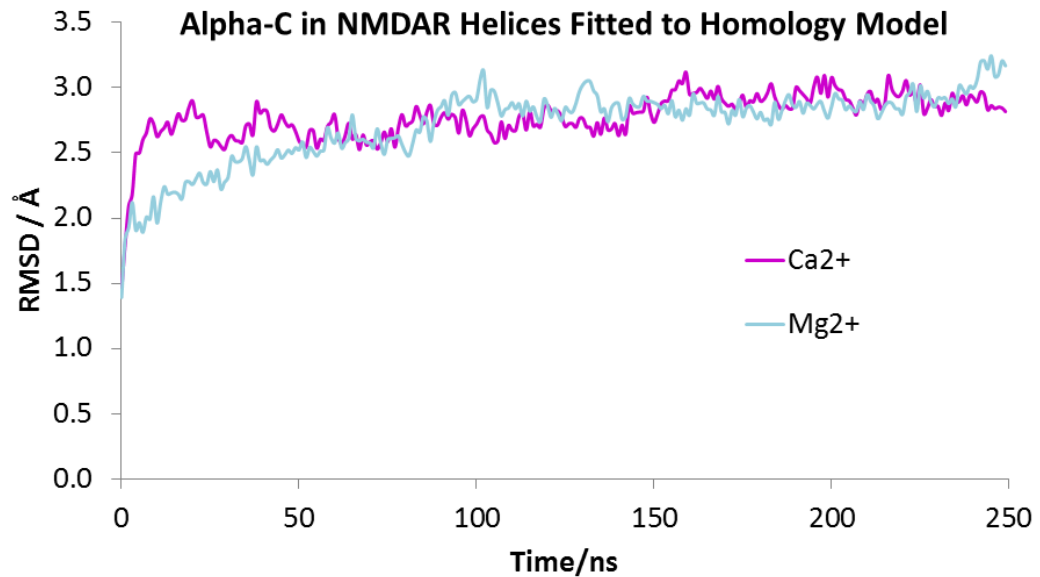


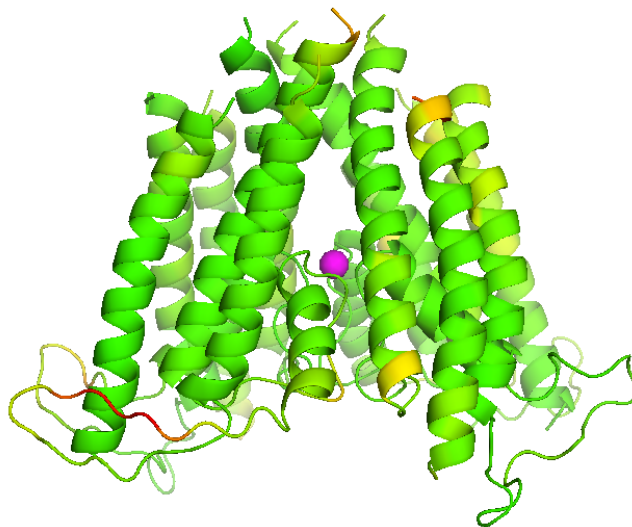
Figure 3.12: Total RMSD

at most 3 Å, becoming stable with only a few fluctuations. Therefore, the data show that the initial structure changes, but it quickly becomes stable. Figure 3.14 shows the average RMSD compared to the homology model conformation before any equilibration. This figure confirms the overall stability of the structure, and the deviation of about an Å.

The RMSFs in Figure 3.13 show the motion of each residue within an average position in the last 100 ns of simulations. As in the case of the equilibration in vacuum, the RMSFs indicate that the loops and the terminal residues of the structure exhibit greater average flexibility than the other residues. The RMSFs also indicate a very stable structure for each of the subunits, in each of the simulations with different divalent ions.

In the simulation where Ca^{2+} is present in the channel binding site, we also observe a faster conformational change of the protein model when compared to the simulation with Mg^{2+} . However, both simulations achieved the same overall final RMSD (3 Å– see Figure 3.12). Thus the data indicate a faster

(a) Ca^{2+} in the core of the model



(b) Mg^{2+} in the core of the model

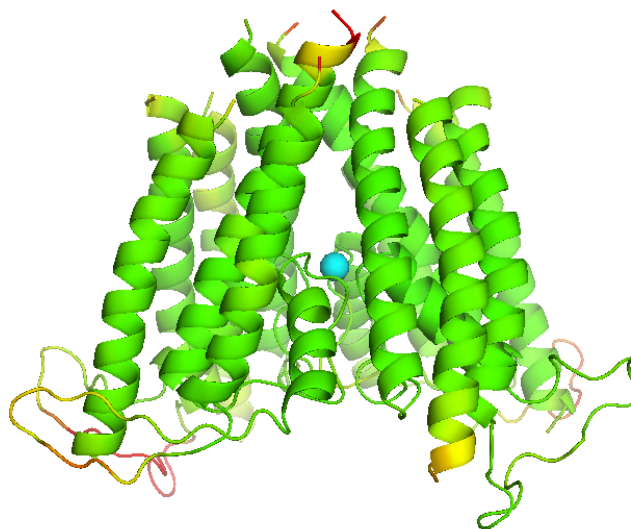
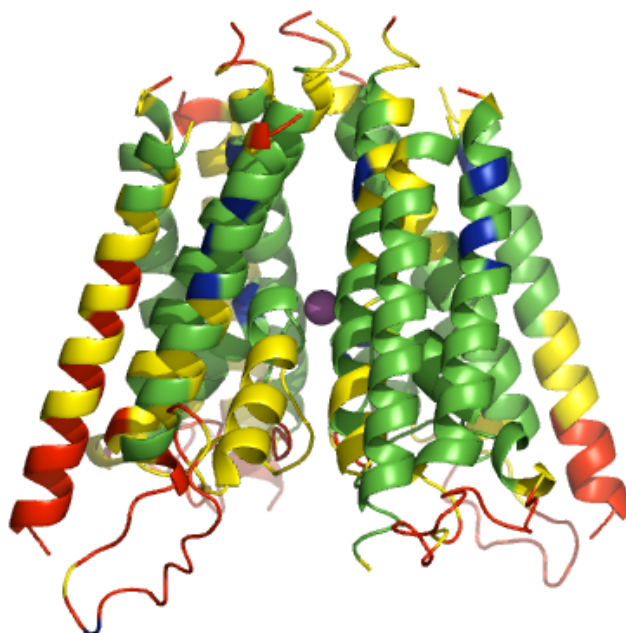


Figure 3.13: NMDAR RMSF for the production run in the membrane and water. The backbone is colored according to RMSF value: green is for $\text{RMSF} < 1.0\text{\AA}$, yellow is for $1.0\text{\AA} < \text{RMSF} < 2.0\text{\AA}$, and red is for $\text{RMSF} > 2.0\text{\AA}$.

(a) Ca^{2+} in the core of the model



(b) Mg^{2+} in the core of the model

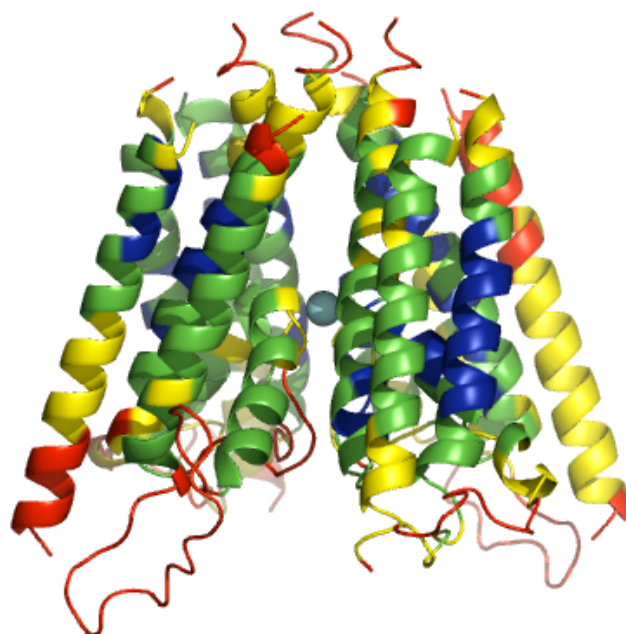


Figure 3.14: Average RMSD per residue for 250 ns of the simulations. The residues are colored according to the degree of motion: blue for smaller or equal than 1.5 Å, green for between 1.5 Å and 3 Å, yellow between 3 Å and 5 Å, red for bigger than 5 Å

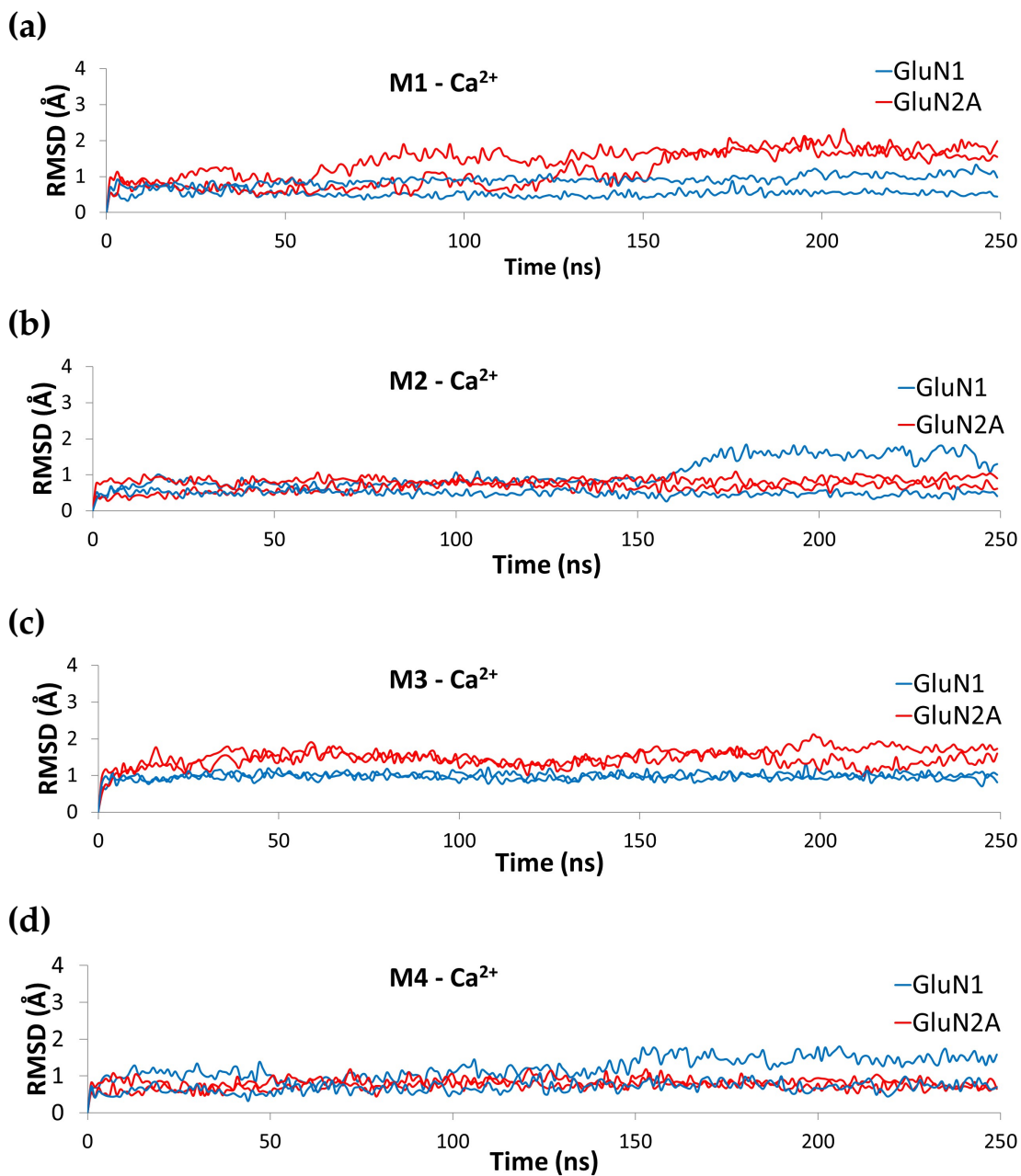


Figure 3.15: RMSDs for α -carbons of the helices in the simulation in which Ca^{2+} was in the core of the NMDAR model. The blue curves indicate GluN1 and the red curves indicate GluN2A. (a) RMSD for M1 α -carbons. (b) RMSD for M2 α -carbons. (c) RMSD for M3 α -carbons. (d) RMSD for M4 α -carbons.

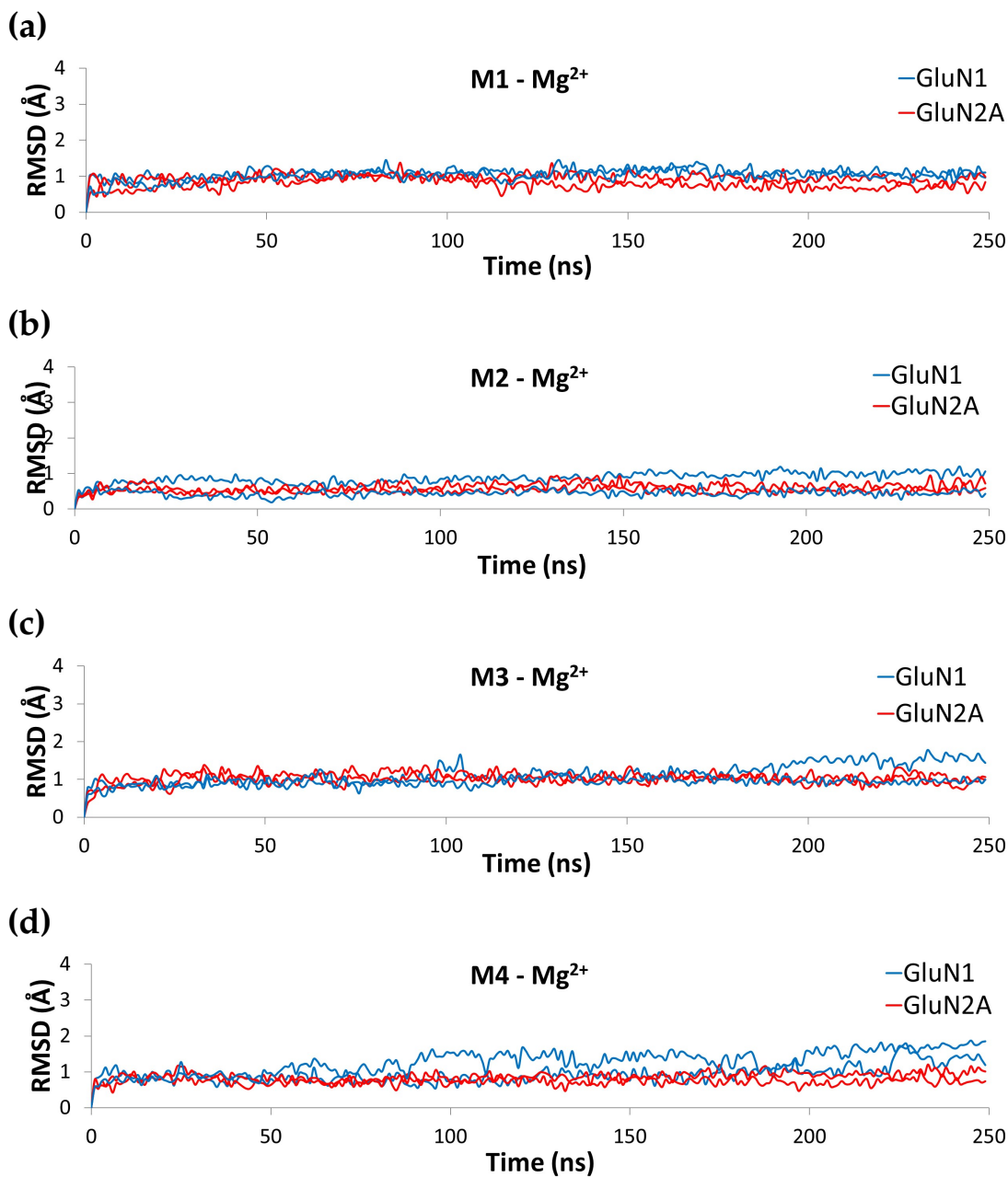


Figure 3.16: RMSDs for the α -carbons of the helices in the simulation in which Mg^{2+} was in the core of the NMDAR model. The blue curves indicate GluN1 and the red curves indicate GluN2A. (a) RMSD for M1 α -carbons. (b) RMSD for M2 α -carbons. (c) RMSD for M3 α -carbons. (d) RMSD for M4 α -carbons.

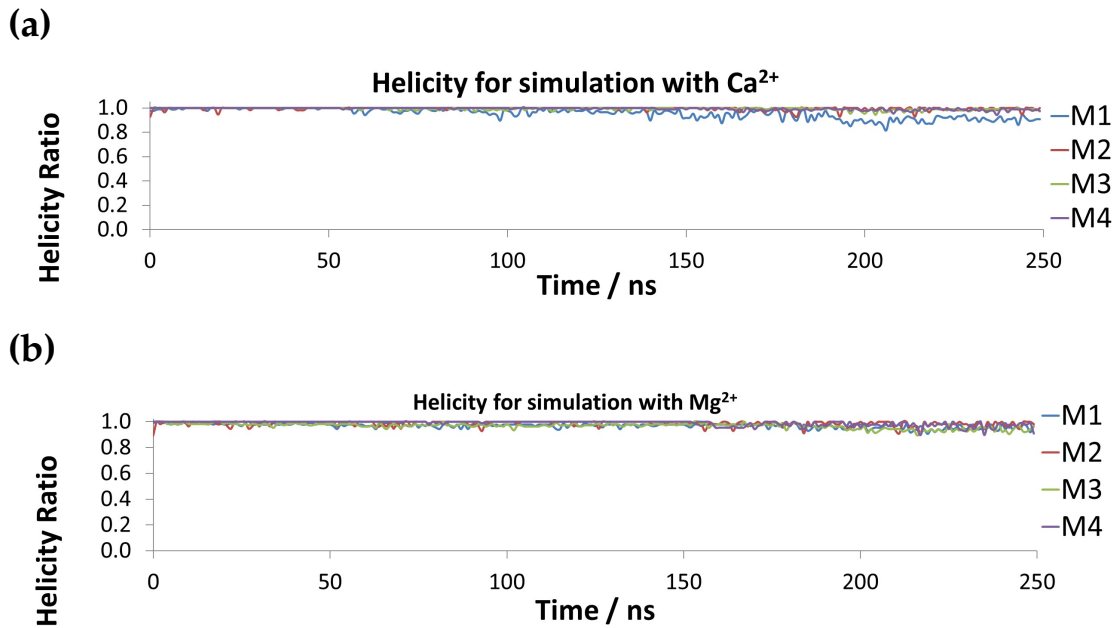


Figure 3.17: Helicity ratio for each set of 250 ns of simulations. (a) Helicity ratio for the helices in the simulations in with Ca^{2+} was in the pore. (b) Helicity ratio for the helices in the simulations in with Mg^{2+} was in the pore.

relaxation time of the protein model with Ca^{2+} than for the model with Mg^{2+} . This is possibly because Ca^{2+} has a higher ligand rate of exchange than Mg^{2+} (as discussed in Chapter 2) and thus the presence of Ca^{2+} leads the structure to move more and achieve equilibration faster than when Mg^{2+} is in the protein.

Figure 3.15 and Figure 3.16 show the RMSDs for the α -carbons in each of the individual helices. These graphs show that the two types of subunit relax differently in the simulations with Ca^{2+} in the binding site: GluN1s are more stable than GluN2As for M1, M2, and M3 helices. This is probably because the selectivity filter of NaK is more similar to GluN1s than to GluN2As (see alignment in Fig. 3.2). Hence NaK is perhaps a better template for GluN1 than for GluN2A. Both subunits behave similarly when Mg^{2+} is in the model binding site, which suggests that the presence of Mg^{2+} attenuates drastic conformational changes. In the case of M4 helices, for both ions in the core of the

protein, we observe a greater stability of GluN2A when compared to GluN1. Once again the similarity between subunits and the chosen template is perhaps the explanation for this phenomenon: the M4 helices of AMPAR are more similar to GluN2A than to GluN1.

The stability of the secondary structure is shown in the calculation of the helicity of M1, helical part of M2, M3, and M4 as a function of time (Fig. 3.17). There are only minor changes in the secondary structure. During the simulation, the alpha and 3-10 helices maintained a helicity greater than 90%.

Pore Shape and water in the Pore Show that the Channel is Well-formed

Figure 3.18 shows the pore for the NMDAR model simulations with Ca^{2+} and Mg^{2+} in the channel. In this figure, the asparagines fill the region surrounding each ion. The asparagine oxygens form a cage that surrounds each ion, and thus these asparagines provide the ideal environment that function like branches that capture the ions.

Our Model Agree with Experimental Data

Another approach for checking the quality of the model is to compare its properties with known experimental data. According to experiments from (Retchless et al., 2012), GluN2A(S632) is likely near GluN1(W608). Figure 3.21 shows that our simulations endorse this proximity by having these residues at an average distance shorter than 5 Å for the simulations in which Ca^{2+} is in the core of the protein, and on average shorter than 3.6 Å for the simulations in which Mg^{2+} was in the core of the protein model. Then distances were measured from an oxygen in the serines to a carbon in the cycle in the tryptophans. Retchless et al. (2012) also discuss the distance between GluN2A(S632) and GluN1(W611), however their results are inconclusive. In our simulation in which Ca^{2+} is in the core of the protein we observe a distance smaller than 4.6 Å, while for that

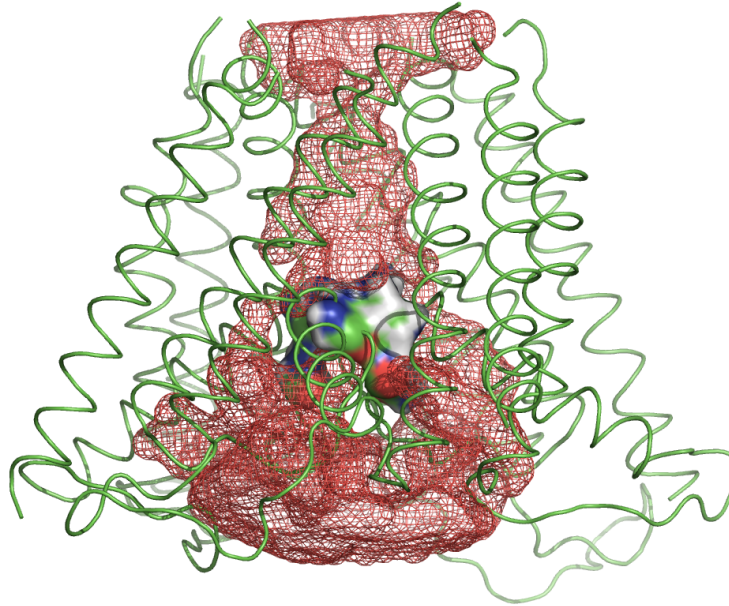
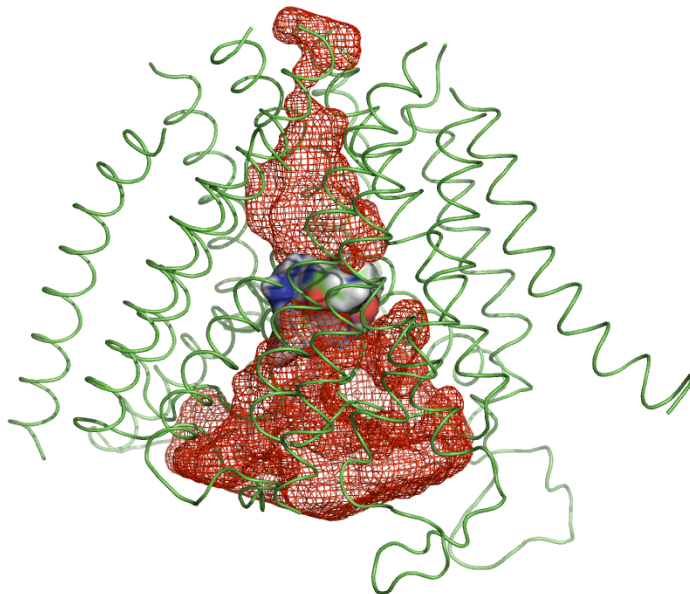
(a)**(b)**

Figure 3.18: Pore at 150 ns of simulation. The meshed red regions correspond to the pore volume. The protein is the green spring. The asparagines are represented as space filling atoms in the center of each figure, surrounding each ion. (a) Ca^{2+} is in the center of the protein. (b) Mg^{2+} is in the center of the protein.

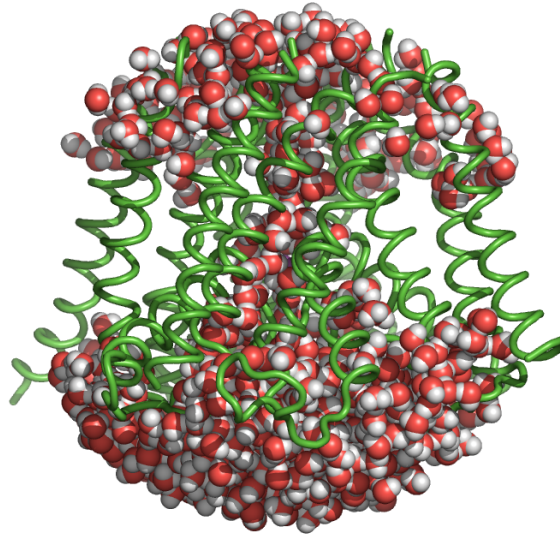


Figure 3.19: Water in the cavity of the simulated TMD NMDAR model.

in which Mg^{2+} is in the core of the protein the distance is on average 4.2 Å for one of the subunit pairs, but around 6 Å for the other one. The consistently close pairs in the simulation in which Ca^{2+} was present indicates that perhaps the intersubunit interact would also be confirmed for all four distances in the simulation in which Mg^{2+} if we allow a longer simulation. The distances of equivalent residues in AMPAR structure (see Fig. 3.2) were of the order of 20 Å or higher, which corroborates the good choice of NaK as the template for the M2-M3 regions.

3.4 CONCLUSION

We used homology modeling to develop structural models of a mutated TMD GluN1/GluN2A receptor based on NaK channels for the M1, M2, M3 regions and AMPAR for the M4 helices. This model was first equilibrated in

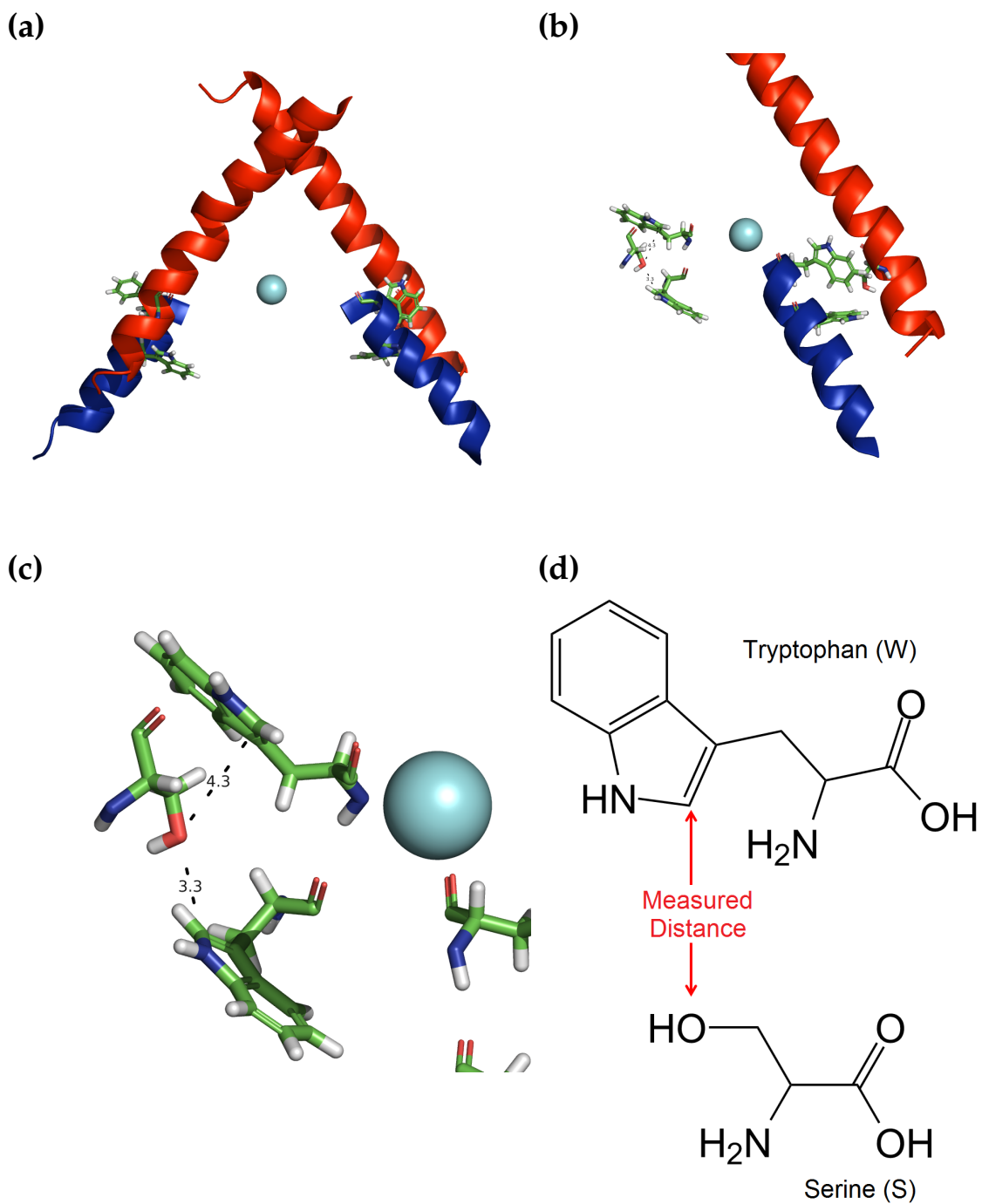


Figure 3.20: Distances measured from an oxygen in the serines GluN2A(S632) to a carbon in the cycle in the tryptophans GluN1(W608) and GluN1(W611). (a) GluN1 M2 (blue) and GluN2A M3 (red) are represented. (b) Two of the helices are hidden for a better visualization. The serine and tryptophans are represented as sticks. (c) The serine and tryptophans are zoomed in. (d) The measured distances are shown in red.

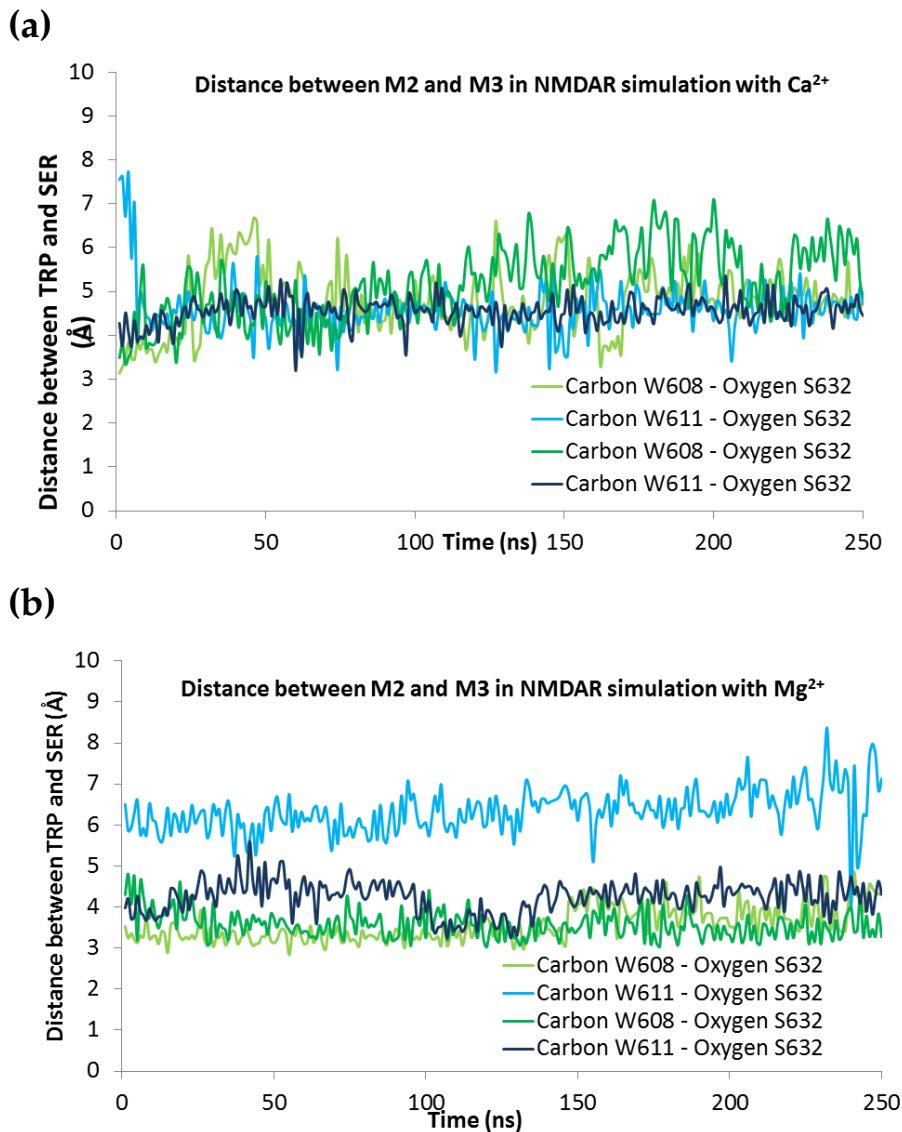


Figure 3.21: Distances measured during 250 ns of simulations from the oxygen side chain in the serines to a carbon in the cycle in the tryptophans GluN1(W608) and GluN1(W611). See Fig. 3.20 for a description of the atoms used for the comparative distance. (a) Simulation in which Ca^{2+} was present. (b) Simulation in which Mg^{2+} was present.

vacuum. Thereafter two structures of the mutated TMD NMDAR model with either Ca^{2+} or Mg^{2+} in a protein binding site were equilibrated in membrane and water. The model with Ca^{2+} has a greater initial change in the overall structure, but both sets of simulations achieved the same overall change from the initial homology model to the final equilibrated structure. GluN2A was the least homologous to the NaK channel, and thus has a greater contribution to the overall change in the backbone RMSD than the GluN1 subunits for the M1, M2, and M3 helices. Experimental observations such as the distance between M2 (GluN1(W608) or GluN1(W611)) and M3 GluN2A(S632) are in agreement with our model. Therefore, our analyses showed our TMD NMDAR model is stable and is consistent with experimental data.

SIMULATING DIVALENT ION INTERACTIONS IN TRANSMEMBRANE DOMAIN OF NMDAR

4.1 INTRODUCTION

In Chapter 3, we developed a well-behaved TMD NMDAR model. In the present chapter, we perform simulations using this model to study ion interactions through protein environment. An important facet of understanding Ca^{2+} permeation and Mg^{2+} block of NMDAR is accurately calculating how the free energy changes when each ion interacts with the protein binding site, as well as the free energy barrier along the permeation coordinate.

As discussed in Chapter 2 and Chapter 3, the selectivity filter of a NMDAR is the extended region of the reentrant loop where the divalent ion permeation is mainly controlled (Dingledine et al. (1999); Traynelis et al. (2010) - see also Fig. 2.1). In the top part of the NMDAR selectivity filter there are six asparagines. It is believed that the interaction between these six asparagine residues and each divalent ion plays a critical role in the permeation because this is the most likely ionic binding site (Burnashev et al., 1992; Dingledine et al., 1999; Kuner et al., 1996; Wollmuth et al., 1998b).

In this chapter, we use umbrella sampling and thermodynamic integration to model the free energy involved in Mg^{2+} and Ca^{2+} explicit behaviors in the channel. Both methods have been successfully used to understand ion permeation in other ion channels (Allen et al., 2006), as well as to calculate other ion channel properties and ion binding sites (Jiao et al., 2008; Kumar and Mayer, 2013; Mamonov, 2006; Mamonova and Kurnikova, 2006; Yonkunas, 2010).

4.2 METHODOLOGY

All simulations described in this chapter are all-atom molecular dynamics simulations in explicit TIP3P water solvent (Jorgensen et al., 1983), using AMBER 10 force field (Li and Brüschweiler, 2010; Lindorff-Larsen et al., 2010) in the AMBER 12 package (Case et al., 2012). The integration time step was 1 fs with the temperatures maintained at 300K by a Langevin thermostat (Adelman and Doll, 1976). Periodic boundary conditions and all atom wrapping were also imposed for all simulations. Long range electrostatics were calculated with Particle Mesh Ewald (PME) (Darden et al., 1993). The Van der Waals cutoff distance was 12 Å. Except for the thermodynamic integration calculations, we performed these simulations using the GPU accelerated code (Gootz et al., 2012; Salomon-Ferrer et al., 2013). We performed the TI calculations in this chapter using HARLEM (Kurnikov, 1999).

4.2.1 *Number of Oxygen Ligands*

The frequency of exchange of oxygen atoms within 2.5Å of each ion was recorded for every ns of the 250 ns of each simulation from the previous chapter.

4.2.2 Free Energy of Ca^{2+} in the Binding Site Compared to Mg^{2+}

The equilibrated full TMD NMDAR model in membrane and water was used to calculate the free energy difference between Mg^{2+} and Ca^{2+} placed in the protein binding site. This free energy was calculated using TI (see Chapter 2 for more details). Three independent set of TI MD simulations were performed: for the gradual substitution of Mg^{2+} by Ca^{2+} , sets of three and five λ -values were used, and for the substitution of Ca^{2+} by Mg^{2+} the total number of λ -values was three. The time of the MD simulation for each λ -value was 500 ps.

4.2.3 Permeation of Each Divalent Ion: Exchange Between Water and Protein Residues

We calculated the PMF using umbrella sampling (Kästner, 2011; Torrie and Valleau, 1977). MD-PMF simulations with standard empirical force fields have been successfully used in the literature to study ion channels and predict properties in agreement with experimental data (Allen et al., 2006). In this study, we use a similar approach to study NMDAR with Ca^{2+} or Mg^{2+} . We used our realistic mutated NMDAR-membrane-water system and chose a reaction coordinate that captures the permeation process.

We used harmonic umbrella potentials $V(\vec{r}) = \frac{1}{2}k(\vec{r} - \vec{r}_{\text{eq}})^2$ with force constant to gradually increase the distance from the vicinity of the binding site and ion at 0.25 Å increments from -10.0 Å to $+10$ Å along the y-axis (Fig. 4.1). Thus the ion was moved throughout the channel until the cavity in the protein, that is filled with water. The harmonic potentials had a force constant of 6 kcal.mol⁻¹Å⁻² and 20 kcal.mol⁻¹Å⁻² for the simulations in which Ca^{2+} was in the core of the protein, and a force constant of 20 kcal.mol⁻¹Å⁻² and 60 kcal.mol⁻¹Å⁻² for the simulations using Mg^{2+} . The force constants were chosen to ensure overlap of neighboring windows. We plotted the PMF for

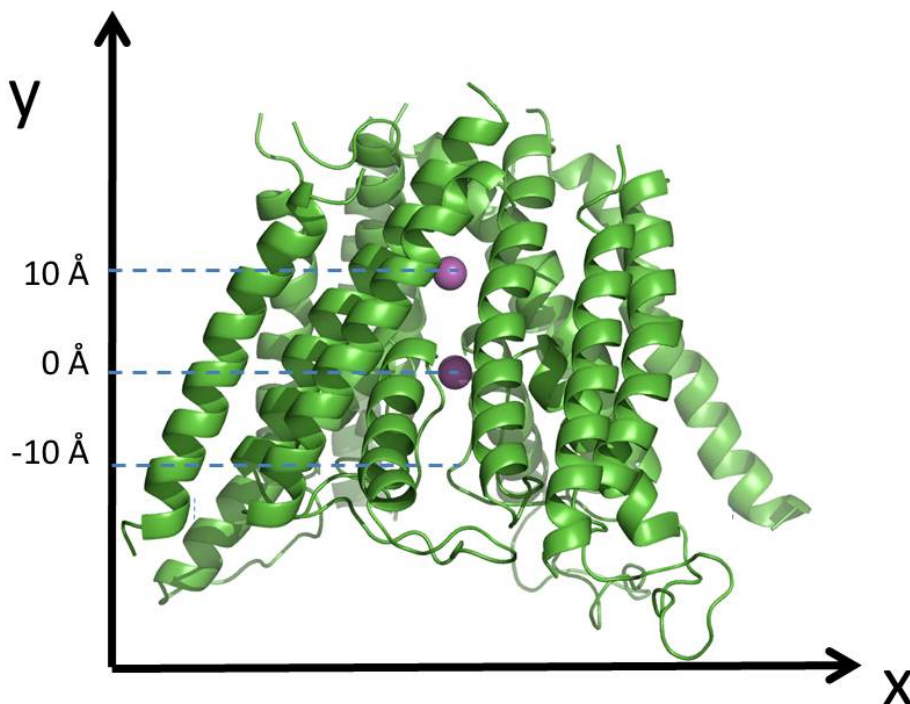


Figure 4.1: Representation of the calculated umbrellas for chosen reaction coordinate. The positioning of the ion (in magenta) is represented relative to our model. Each divalent ion was gradually moved across the channel in the y direction.

this y coordinate (see Fig. 4.1). For each of the windows, minimization was performed for 400,000 steps before at least 2 ns of trajectory generation. The set of windows were unbiased using the weighted histogram analysis method (WHAM) (Chipot and Pohorille, 2007; Kumar et al., 1992, 1995; Souaille and Roux, 2001), which consists of solving coupled equations for the optimal estimate for distribution of states.

4.3 RESULTS AND DISCUSSION

4.3.1 Water and ASN exchange in the Protein Environment

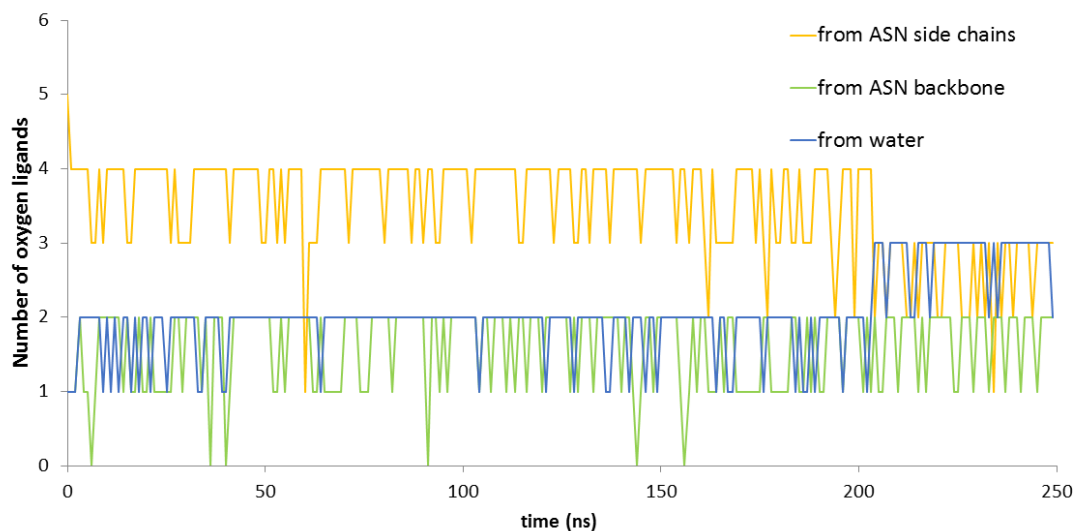


Figure 4.2: Total number of oxygen ligands around Ca^{2+} for the time of the simulation. The total number from asparagine side chains, from asparagine backbones, and from water are in yellow, green, and blue, respectively.

In Chapter 3 we started the full homology model with a symmetric formation of the oxygens around the Mg^{2+} in the binding site, equilibrated with fixed distances from side chain oxygens to Mg^{2+} . Then, we removed these restraints in the full protein-membrane-water system. After that, we allowed the protein to find its energy minimum, regardless of symmetry. In this chapter, the analyses of the simulations show that after the Mg^{2+} -oxygen restraints were released, the structure was persistently non-symmetric. Moreover, this asymmetry was an arrangement of with five oxygen donors from asparagines and one from water around Mg^{2+} . The presence of a persistent arrangement around Mg^{2+} indicated that the exchange of ligands around Mg^{2+} requires more energy and thus is more likely to be dissociative than associative. For the simulation in

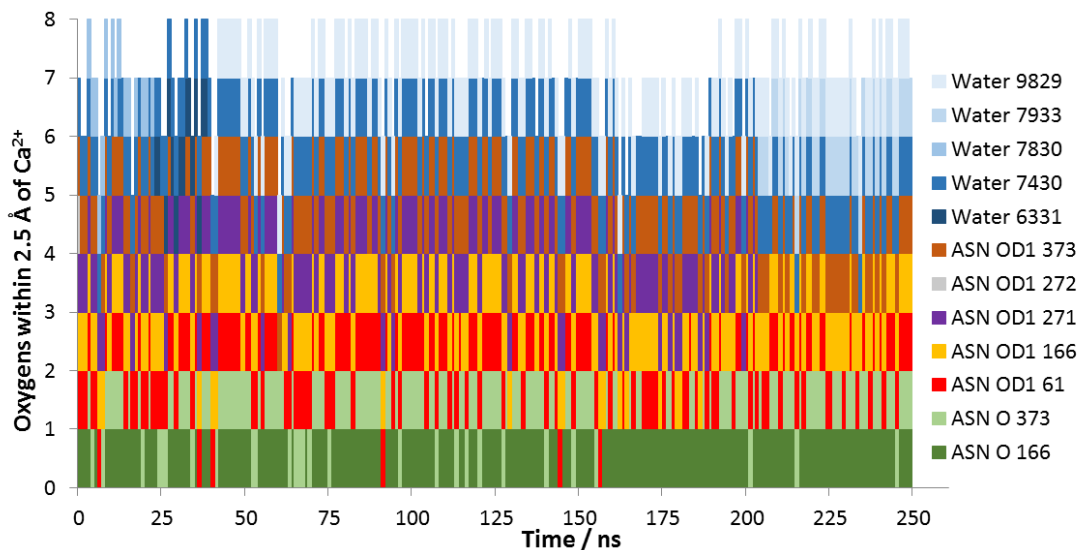


Figure 4.3: Each oxygen ligand around Ca^{2+} for the time of the simulation. OD1 and O are the atom names in asparagine simulation model for oxygen in its side chain or its backbone, respectively. The water molecules are represented in blue.

which Ca^{2+} was in the core of the protein, we calculated a changing number of oxygen donor ligands surrounding this divalent ions. This simulation with Ca^{2+} had mostly from six to eight oxygen ligands, rarely five (Table 4.1). This indicates an associative mechanism for Ca^{2+} , because there is an increased number of ligands for the simulation with Ca^{2+} when compared to the arrangement of six ligands around Mg^{2+} . Figure 4.2 and 4.3 show that the ligands are oxygens that vary from asparagine backbone, asparagine side chain, and water molecules.

There may exist other arrangements for Mg^{2+} besides the one we found. Overall these results show that Ca^{2+} is more permissive than Mg^{2+} to exchange ligands in the protein, which is also the case in solvent simulations.

Table 4.1: Number of oxygen ligands in the solvation shell of Ca^{2+} in 250 ns of simulation.

Number of oxygen-ligands	Total	From ASN	From water
1			13.2
2			71.2
3		2.0	15.6
4		21.2	
5	2.8	41.2	
6	17.2	35.6	
7	44.4		
8	35.6		
	100%	100%	100%

4.3.2 Free Energy Cycle

The divalent ions change their oxygen donor interactions when they move from solution into the channel and then back to solution. By studying how the free energy for these interactions change, we can better understand the NMDAR selectivity mechanism (Fig. 4.4).

Table 4.2: Free energy (in kcal/mol) calculated from Mg^{2+} to Ca^{2+} using three λ -values. These are calculations for ions at binding site in the channel.

λ_i	0.11271	0.50000	0.88729	
w_i	0.27777	0.44444	0.27777	
$\langle \frac{\partial V}{\partial \lambda} \rangle_\lambda$ (500 ps)	161.45	53.69	31.17	
$\langle \frac{\partial V}{\partial \lambda} \rangle_\lambda$ (last 400 ps)	161.22	52.75	30.67	
$\langle \frac{\partial V}{\partial \lambda} \rangle_\lambda$ (last 300 ps)	161.45	52.39	30.55	
$\lambda_i \times w_i$ (400 ps)	44.78	23.44	8.52	$\Delta G = 76.75$
$\lambda_i \times w_i$ (300 ps)	44.85	23.29	8.49	$\Delta G = 76.62$

Table 4.3: Free energy (in kcal/mol) calculated from Ca^{2+} to Mg^{2+} using three λ -values. These are calculations for ions at binding site in the channel.

λ_i	0.11271	0.50000	0.88729	
w_i	0.27777	0.44444	0.27777	
$\langle \frac{\partial V}{\partial \lambda} \rangle_\lambda$ (500 ps)	-33.43	-52.05	-164.22	
$\langle \frac{\partial V}{\partial \lambda} \rangle_\lambda$ (last 400 ps)	-33.50	-51.80	-163.80	
$\langle \frac{\partial V}{\partial \lambda} \rangle_\lambda$ (last 300 ps)	-33.53	-51.29	-163.65	
$\lambda_i \times w_i$ (400 ps)	-9.30	-23.02	-45.50	$\Delta G = -77.82$
$\lambda_i \times w_i$ (300 ps)	-9.31	-22.80	-45.46	$\Delta G = -77.57$

Table 4.4: Free energy (in kcal/mol) calculated from Mg^{2+} to Ca^{2+} using five λ -values. These are calculations for ions at binding site in the channel.

λ_i	0.04691	0.23076	0.50000	0.76923	0.95308	
w_i	0.11846	0.23931	0.28444	0.23931	0.11846	
$\langle \frac{\partial V}{\partial \lambda} \rangle_\lambda$ (500 ps)	210.43	112.21	52.44	37.45	31.01	
$\langle \frac{\partial V}{\partial \lambda} \rangle_\lambda$ (last 400 ps)	210.00	112.16	52.10	37.49	31.00	
$\langle \frac{\partial V}{\partial \lambda} \rangle_\lambda$ (last 300 ps):	209.47	112.06	52.27	37.39	31.01	
$\lambda_i \times w_i$ (400 ps)	24.88	26.84	14.82	8.97	3.67	$\Delta G = 79.18$
$\lambda_i \times w_i$ (300 ps)	24.81	26.82	14.87	8.95	3.67	$\Delta G = 79.12$

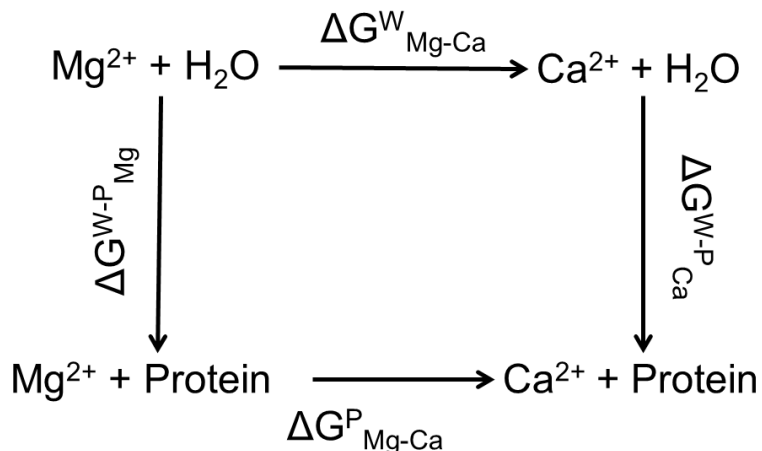


Figure 4.4: Free energy cycle.

We ran three different TIs for the protein. TI is very time-consuming, hence we simulated each λ for no more than 500 ps (Fig. 4.5). During the simulation time, the values are reasonably stable.

The TI solvation free energy difference from Ca^{2+} to Mg^{2+} in water and protein are very similar. The difference in free energy between substituting divalent ions shows a higher stability for Mg^{2+} when compared to Ca^{2+} in the likely binding site. This agrees with the discussion in Chapter 2, in which we concluded that Mg^{2+} is more stable than Ca^{2+} in an amide-like environment.

The solvation free energy shows whether the channel residues bind to Mg^{2+} more strongly than Ca^{2+} , it is a static energy. It does not give information on the energy necessary for each ion to cross the channel. Nevertheless, although we do not know the independently $\Delta G_{\text{Mg}}^{(P-W)}$ and $\Delta G_{\text{Ca}}^{(P-W)}$, we can conclude from the energy cycle calculation that the difference in binding energy in the core of the channel compared to the one in water indicates is also small when comparing Ca^{2+} and Mg^{2+} , and thus that the asparagines provide a similar

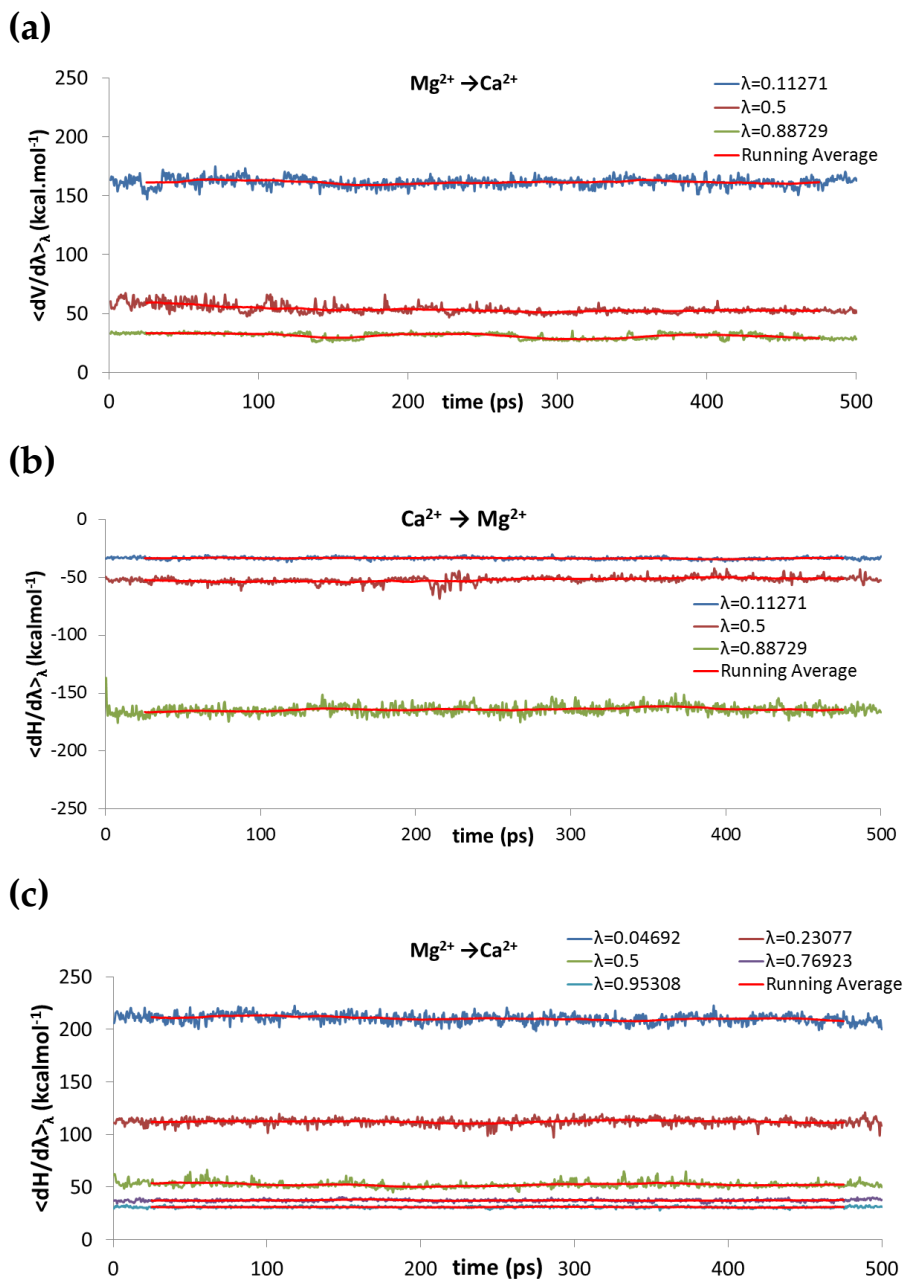


Figure 4.5: $\langle \frac{\partial V}{\partial \lambda} \rangle_\lambda$ at each time step for the exchange between Ca^{2+} and Mg^{2+} in a binding site of the TMD NMDAR model. Each point in the running average (the red line in the graphs) corresponds to the average of $\langle \frac{\partial V}{\partial \lambda} \rangle_\lambda$ of 50 ps of vicinal points of each time step. (a) The ΔG is calculated from Ca^{2+} to Mg^{2+} using 3 λ -values. The final ΔG value is -77.60 kcal/mol when we use only the last 300 ps and -77.8 kcal/mol when we use only the last 400 ps. (b) The ΔG is calculated from Mg^{2+} to Ca^{2+} using 3 λ -values. The final ΔG value is 76.62 kcal/mol when we use only the last 300 ps and 76.74 kcal/mol when we use only the last 400 ps. (c) The ΔG is calculated from Mg^{2+} to Ca^{2+} using 5 λ -values. The final ΔG value is 79.12 kcal/mol when we use only the last 300 ps and 79.18 kcal/mol when we use only the last 400 ps.

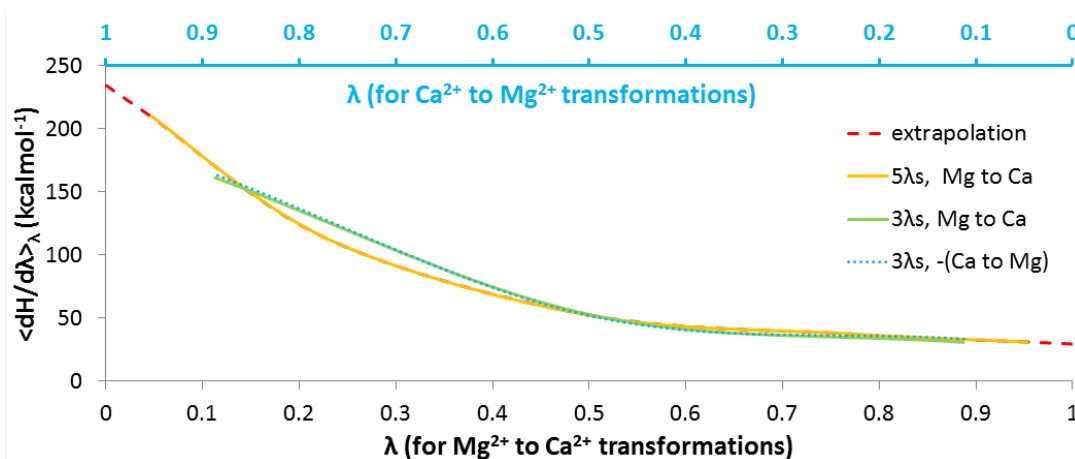


Figure 4.6: Ensemble average $\langle \frac{\partial V}{\partial \lambda} \rangle_\lambda$ versus λ -values to calculate free energy results using thermodynamic integration. The upper x-axes correspond to the λ -values for the transformation from Ca^{2+} to Mg^{2+} and the lower x-axes correspond to the opposite transformation. The results for the transformation from Ca^{2+} to Mg^{2+} were multiplied by -1 to show that for all simulations the final calculated free energy corresponds to almost the same value. The value for the solvation free energy is calculated by integrating the area under the extrapolated graph.

water environment for these divalent ions (see Eq. 4.1). This is likely due to the similarity in reaction fields between water and the binding site of the protein. Water has a high dielectric constant, leading to a high reaction field. Though the protein is overall hydrophobic because of its presence in the lipid membrane, the likely binding site consists of asparagines, which are hydrophilic, and therefore raise the local dielectric. This in turn increases the reaction field, in the binding site, to a level comparable to that of water.

$$\begin{aligned}
 \Delta\Delta G &= \Delta G_{\text{Mg}}^{(W-P)} - \Delta G_{\text{Ca}}^{(W-P)} = \\
 &= \Delta G_{\text{Mg-Ca}}^{(W)} - \Delta G_{\text{Mg-Ca}}^{(P)} = \\
 &= 79.8 - 79.2 = \\
 &= -0.6 \text{ kcal/mol}
 \end{aligned} \tag{4.1}$$

In summary, based on the energy cycle of Fig. 4.4, we can get the value for $\Delta\Delta G$ (see Eq. 4.1), and thereby conclude that the energy difference between being in water on the outside of the channel and being at the binding site is about the same for Mg^{2+} and Ca^{2+} even though we cannot calculate the actual energy difference for either one independently using TI.

Potential of Mean Force (PMF)

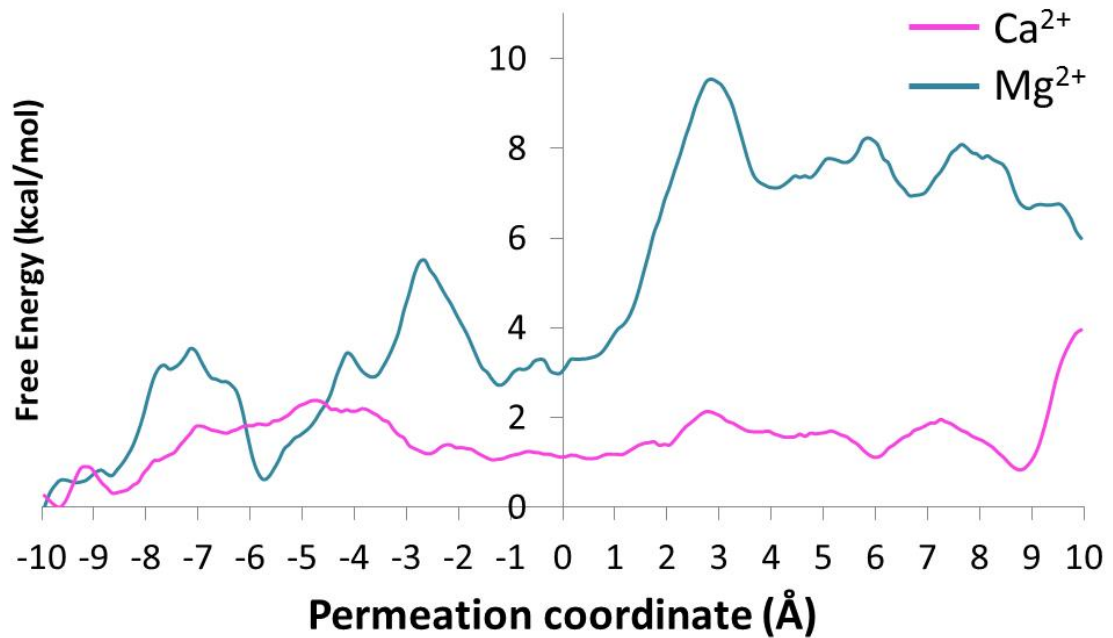


Figure 4.7: Potential of mean force for each divalent ion being placed along the permeation reaction coordinate.

Figure 4.7 shows the PMF results. Here we can see the minima as a function of the positions in which each of the asparagines detached the ion. Overall the PMF is flat for Ca^{2+} and it shows a higher barrier for Mg^{2+} . The multiple local minima show the kinetic effect, and confirms the trend in the exchange reaction, in which for each minimum each ion has at least one less oxygen donor from asparagines. One should be careful when interpreting this graph

though: there are limitations intrinsic to the slow substitution of exchange in the first solvation shell of Mg^{2+} . The energy profile is not complete until all possible configurations around Mg^{2+} are sampled for each simulated position, but in the case of the presented graph, only one configuration was found per position.

4.4 CONCLUSION

Our study shows the subtle differences between the NMDAR model when Ca^{2+} and Mg^{2+} are in its core. Energetically, Mg^{2+} is more stable in the core of the protein than Ca^{2+} , as expected from our results in Chapter 2, in which Mg^{2+} was more stable in amides than Ca^{2+} as well. The binding free energy in the channel is at the same order of magnitude of the binding free energy in water, showing that the water environment for each ion is similar to the protein environment for the same ions.

The comparison between the exchange of ligands for Mg^{2+} and Ca^{2+} in our NMDAR model, as well as the local and global conformation changes discussed here and in the previous chapter, indicates that different ions will accommodate different local arrangements. Nevertheless, the RMSDs calculated in Chapter 3 suggested that both models converged to the same structure. In this chapter we reproduced a permeation path for each of the ions. For both ions, the channels represent a similar type of cage, but Mg^{2+} accommodates the six-ligands more strongly than Ca^{2+} does. Moreover, Ca^{2+} exchanged ligands in water and in the channel, while for Mg^{2+} no exchange was observed.

For the simulation in which Mg^{2+} was in the core of the protein, we found a persistent arrangement of six oxygen atoms in the ion coordination shell: one from a water molecule, four from asparagine side chains, and one from a as-

paragine backbone. For the simulation of the model with Ca^{2+} in its core, the number of oxygen ligands varied from six to eight, and they were a mix of oxygen from water molecules, and from asparagine side chains and backbones. This indicates that the exchange of ligands in the solvation shell of Ca^{2+} happens more often than for the solvation shell of Mg^{2+} in the protein, as it is also true in a solvent environment such as water and amides.

Mg^{2+} exchanges its ligands at a slower rate than Ca^{2+} , and we believe this leads Mg^{2+} to block the channel and allows Ca^{2+} to cross it. The binding site is not rigid, and not all six asparagines bind the ions at the same time. Moreover, the channel is narrow enough to have oxygens from the asparagine backbones and side chains involved in the binding cage in the presence of the ions. These asparagines provide the ideal environment that functions like branches that capture the ions.

The PMF results confirm that Ca^{2+} crosses the channel with more ease than Mg^{2+} . PMF also confirmed that there is not a well defined binding site for Ca^{2+} in the selectivity filter region (Premkumar and Auerbach, 1996; Watanabe et al., 2002). PMF indicates an overall interpretation of how the ion moves through the selectivity filter. The region of the binding site is inferred based on experimental data, because if asparagines in the selectivity filter are mutated, the channel loses the ability to be blocked by Mg^{2+} . However the exact position of the binding site is unknown. Nevertheless, our free energy profile allows the characterization of possible binding sites, gives a semi-quantitative interpretation, and reproduces the permeation trend correctly.

CONCLUSIONS AND FUTURE WORK

In this thesis, we showed how computational chemistry methods can be used to give insights into a poorly understood complex biological system, the divalent ion selectivity in NMDARs. This goal was achieved by (i) using solvents to mimic the protein environment, (ii) building a realistic model of a TMD NMDAR in membrane and water, and (iii) using this model to predict the mechanisms of Mg^{2+} block and Ca^{2+} permeation in NMDARs.

Amide Solvents Reasonably Mimic Asparagine Interactions

The number of oxygen donors surrounding each divalent ion is an indication of the mechanism by which Ca^{2+} permeates NMDARs while Mg^{2+} blocks the channel. We used different solvents to mimic how the divalent ions interact with oxygen donors while these ions cross the channel. In this study, we performed a series of *ab initio* calculations of Ca^{2+} and Mg^{2+} in water to evaluate the mechanism of exchange of oxygen donor ligands with these divalent ions. We also performed MD simulations using water, and the amides NMA and DMF. This was done to mimic how the interactions of each ion with water are replaced by interactions with asparagines.

The *ab initio* calculations showed a higher barrier for solvation shell exchange in Mg^{2+} when compared to Ca^{2+} . The calculations of the total solvation free energy in solution yield accurate results. These results show the higher stability of Ca^{2+} and Mg^{2+} in NMA and DMF when compared to water, a trend that confirms the higher stability of these divalent ions in the core of the protein compared to the solvation of water.

The MD simulations using amide and water solvents reasonably reproduce experimental data for energy calculations, as well for the kinetic barrier calculations for Ca^{2+} . Hence these calculations can be used in the protein simulations. The kinetic barrier calculations for Mg^{2+} are not in complete agreement with experimental results, but the simulation is able to reproduce the barrier energy trend. The kinetic studies can provide a semi-quantitative interpretation of the mechanisms involving Ca^{2+} and Mg^{2+} .

We Developed an Equilibrated TMD NMDAR Model

We used homology modeling to develop a TMD NMDAR model. The templates we used for it consisted of available structures of NaK and AMPAR channels (Shi et al., 2006; Sobolevsky et al., 2009). We used a combination of these templates, in which the helices were chosen so as to give the positioning of residues that best agrees with experimental data. We also mutated four residues in the top of the model to guarantee its stability. The mutant A+7T NMDAR is functional.

We equilibrated the systems and performed two sets of simulations. In each of them we placed either Ca^{2+} or Mg^{2+} in the core of the mutated protein model. The protein models were placed in membrane and water. The analyses

of the equilibration and production runs confirmed that the models were stable and in agreement with experimental data.

Asparagines Function as Branches that Capture Divalent Ions

We calculated the free energy difference between Ca^{2+} and Mg^{2+} in the core of our protein model. This calculation showed a lower energy of Mg^{2+} in the binding site when compared to Ca^{2+} .

Moreover, we calculated the free energy of moving each divalent ion along the y-reaction coordinate, that captures the permeation process. The results show an overall flatter profile for moving Ca^{2+} across the channel, and thus suggest that there is not a binding site with a deep well, as must be the case to permit fast permeation. For the calculations with Mg^{2+} , the PMF graphs indicate we chose a reasonable region for the binding site to place this divalent ion as this position corresponds to a local minimum in the PMF profile.

By calculating the frequency of exchange of solvation shell ligands in the core of the protein, we were able to confirm that the oxygen donor exchange is associative for Ca^{2+} , and dissociative for Mg^{2+} . For the simulation in which Mg^{2+} was in the core of the model, we found a persistent arrangement of six oxygen atoms in the ion coordination shell: one from a water molecule, five from four asparagines. However, there may exist other arrangements for Mg^{2+} besides the one we found. For the simulation of the model with Ca^{2+} in its core, the number of oxygen ligands varied mostly from six to eight (rarely five), and they were a mix of oxygen from water molecules, and from asparagine side chains and backbones. This indicates that Ca^{2+} is more permissive than Mg^{2+} to exchanging ligands in the protein, which is also the case in solvent simulations.

The selectivity filter has a very small pore when either Ca^{2+} or Mg^{2+} are present. This is because the asparagines in this region create a cage that surrounds each divalent ion. This explains how the pore is able to distinguish between Ca^{2+} and Mg^{2+} : these asparagines provide the ideal environment that functions like branches that capture the ions.

In summary, we were able to build a well equilibrated model, and have a better understanding of the TMD NMDAR selectivity mechanism. We believe that this is an important step toward providing a basis for rational drug design.

5.1 FUTURE WORK

Several additional computational studies of NMDARs can be done. For example, one may mutate the model presented in this work to compare model predictions to data. Furthermore, simulation of models with *in silico* mutations would allow prediction of the effect of these alterations in the permeation of ions. Also, a new model in which the subunits are other than GluN₁ and GluN_{2A} may contribute to a better understanding of subtle differences in their functional properties, and thus contribute to rational drug design by targeting different receptor subtypes (Hardingham, 2009; Kiss et al., 2012).

Also, as discussed in Chapter 2, standard force fields reproduce most of the empirical data related to quantifying divalent interaction properties, but not all. One of the missing features in the standard force fields is polarizability, that once taken into account may overcome these issues. Thus using polarizable force fields in the simulations is a natural next step, which we will explore in a forthcoming paper.

A

GAUSSIAN QUADRATURE POINTS AND WEIGHTS

To calculate L , a defined integral from 0 to 1 of a function I that depends on λ , represented as:

$$L = \int_0^1 I(\lambda) d\lambda \quad (\text{A.1})$$

one can use the gaussian quadrature method. To calculate the above integral, this method uses weighted sum:

$$L = \sum_i w_i I(\lambda_i) \quad (\text{A.2})$$

where w_i are the weights chosen according to the λ quadrature points. Without further details, some of the possible sets of λ and weights are listed in the Table [A.1](#).

Table A.1: Sets of λ and weights in the gaussian quadrature method for a total of n number of λ s.

n	λ_i	$1 - \lambda_i$	w_i
1	0.5		1
2	0.21132	0.78867	0.5
3	0.1127	0.88729	0.27777
	0.5		0.44444
5	0.04691	0.95308	0.11846
	0.23076	0.76923	0.23931
	0.5		0.28444
7	0.02544	0.97455	0.06474
	0.12923	0.87076	0.13985
	0.29707	0.70292	0.19091
	0.5		0.20897
9	0.01592	0.98408	0.04064
	0.08198	0.91802	0.09032
	0.19331	0.80669	0.13031
	0.33787	0.66213	0.15617
	0.5		0.16512
12	0.00922	0.99078	0.02359
	0.04794	0.95206	0.05347
	0.11505	0.88495	0.08004
	0.20634	0.79366	0.10158
	0.31608	0.68392	0.11675
	0.43738	0.56262	0.12457

B

COMMAND LINES AND SCRIPTS

B.1 GAUSSIAN AND ANTECHAMBER

The command line in GAUSSIAN for optimization of the geometry is:

```
# P X/6-31G* opt pop=MK
```

and the command for ESP grid calculation is

```
# P X/6-31G* SCF=Tight Pop=MK IOp(6/33=2,6/41=10,6/42=17)Density=current,
```

where X is the level of calculation in both command lines.

The Antechamber command for an output file from the previous calculation is:

```
antechamber -i file.out -fi gout -o res_ dmf.ac -fo ac -c resp
```

```
1 %chk=MGH0H6.chk
  #p MP2/6-31++G** OPT=z-mat SCF=TIGHT

  MG(HOH)6 + HOH exchange rxn, rM06=2.2 (fixed), rM07=3.8

6 2 1
  Mg
  0 1 rM01
  H 2 rOH11 1 aM0H1
  H 2 rOH12 3 aH0H1 1 dMHOH1
11 (...)
```

```

0      1      rM06      2      aOM06      3      dOM0H6
H      17      rOH61      1      aMOH6      2      dHOM06
H      17      rOH62      18     aHOH6      1      dMHOH6
O      1      rM07      2      aOM07      3      dOMOH7
16 H      20      rOH71      1      aMOH7      2      dHOM07
H      20      rOH72      21     aHOH7      1      dMHOH7

rM01      2.1
rOH11      0.9
21 (...)
rOH61      0.9
rOH62      0.9
aMOH6     123.2
aHOH6     106.6
26 dMHOH6    -175.0
aOM06      89.3
dOMOH6     94.8
dHOM06     -1.8
rOH71      0.9
31 rOH72      0.9
aMOH7     129.2
aHOH7     105.3
dMHOH7    -179.0
aOM07     136.1
36 dOMOH7    -94.5
dHOM07     97.7
rM07       3.9

rM06       2.2

```

B.2 AMBER: SAMPLE OF A RESTRAINT INPUT FILE

```

DIHEDRAL RESTRAINT INPUT FILE
# Example of alpha helix phi for residue 21

&rst
iat(1) = 20      , iat(2) = 21      ,
5 iat(3) = 21      , iat(4) = 21      ,
atnam(1) = 'C'   , atnam(2) = 'N'   , atnam(3) = 'CA' ,
atnam(4) = 'C'   , iresid = 1,
r1 = -80.0 , r2 = -70.0 , r3 = -50.0 , r4 = -40.0,

```

```
rk2 = 1.0 , rk3 = 1.0
10 &end
# Example of alpha helix psi for residue 21
&rst
iat(1) = 21      , iat(2) = 21      ,
iat(3) = 21      , iat(4) = 22      ,
15 atnam(1) = 'N  ' , atnam(2) = 'CA  ' , atnam(3) = 'C  ' ,
atnam(4) = 'N  ' , iresid = 1,
r1 = -60.0 , r2 = -50.0 , r3 = -30.0 , r4 = -20.0,
rk2 = 1.0 , rk3 = 1.0
&end
20 # Example of alpha helical h-bond restraint for residue 21
&rst
iat(1) = 21      , iat(2) = 25      ,
atnam(1) = 'O  ' , atnam(2) = 'H  ' ,
iresid = 1,
25 r1 = 1.75 , r2 = 1.80 , r3 = 1.85 , r4 = 2.05,
rk2 = 1.0 , rk3 = 1.0
&end
```

BIBLIOGRAPHY

- Aakesson, Ralf, Pettersson, Lars GM, Sandstroem, Magnus, and Wahlgren, Ulf. Ligand field effects in the hydrated divalent and trivalent metal ions of the first and second transition periods. Journal of the American Chemical Society, 116(19):8691–8704, 1994.
- Aaqvist, Johan. Ion-water interaction potentials derived from free energy perturbation simulations. Journal of Physical Chemistry, 94(21):8021–8024, 1990.
- Abraham, Wickliffe C and Williams, Joanna M. Properties and mechanisms of ltp maintenance. The Neuroscientist, 9(6):463–474, 2003.
- Adelman, SA and Doll, JD. Generalized langevin equation approach for atom/solid-surface scattering: General formulation for classical scattering off harmonic solids. The Journal of Chemical Physics, 64(6):2375–2388, 1976.
- Akesson, Ralf, Pettersson, LG, Sandstrom, Magnus, and Wahlgren, Ulf. Theoretical-study on water-exchange reactions of the divalent and trivalent metal ions of the first transition period. Journal of the American Chemical Society, 116(19):8705–8713, 1994.
- Alam, Amer, Shi, Ning, and Jiang, Youxing. Structural insight into Ca^{2+} specificity in tetrameric cation channels. Proceedings of the National Academy of Sciences, 104(39):15334–15339, 2007.

- Albensi, Benedict C, Igoechi, Chiazor, Janigro, Damir, and Ilkanich, Erin. Why do many NMDA antagonists fail, while others are safe and effective at blocking excitotoxicity associated with dementia and acute injury? American journal of Alzheimer's disease and other dementias, 19(5):269–274, 2004.
- Allen, Toby W, Andersen, Olaf S, and Roux, Benoit. Ion permeation through a narrow channel: using gramicidin to ascertain all-atom molecular dynamics potential of mean force methodology and biomolecular force fields. Biophysical journal, 90(10):3447–3468, 2006.
- Allnér, Olof, Nilsson, Lennart, and Villa, Alessandra. Magnesium ion–water coordination and exchange in biomolecular simulations. Journal of Chemical Theory and Computation, 8(4):1493–1502, 2012.
- Beck, C, Wollmuth, LP, Seeburg, PH, Sakmann, B, and Kuner, T. NMDAr channel segments forming the extracellular vestibule inferred from the accessibility of substituted cysteines. Neuron, 22(3):559–570, 1999.
- Becker, Oren M, MacKerell Jr, Alexander D, Roux, Benoit, and Watanabe, Masakatsu. Computational Biochemistry and Biophysics. CRC Press, 2001.
- Berendsen, Herman JC and Tieleman, D Peter. Molecular dynamics: studies of lipid bilayers. Encyclopedia of computational chemistry, 3:1639–1650, 1998.
- Blanke, Marie L and VanDongen, Antonius MJ. The NR1 M3 domain mediates allosteric coupling in the n-methyl-d-aspartate receptor. Molecular pharmacology, 74(2):454–465, 2008.
- Bleuzen, Anne, Pittet, Pierre-André, Helm, Lothar, and Merbach, André E. Water exchange on magnesium (II) in aqueous solution: a variable temperature

- and pressure ^{17}O NMR study. Magnetic resonance in chemistry, 35(11):765–773, 1997.
- Bock, Charles W and Glusker, Jenny P. Organization of water around a beryllium cation. Inorganic Chemistry, 32(7):1242–1250, 1993.
- Bock, Charles W, Kaufman, Amy, and Glusker, Jenny P. Coordination of water to magnesium cations. Inorganic Chemistry, 33(3):419–427, 1994.
- Bostick, David L and Brooks, Charles L. Selectivity in K^+ channels is due to topological control of the permeant ion's coordinated state. Proceedings of the National Academy of Sciences, 104(22):9260–9265, 2007.
- Brancato, Giuseppe and Barone, Vincenzo. Free energy landscapes of ion coordination in aqueous solution. The Journal of Physical Chemistry B, 115(44):12875–12878, 2011.
- Burnashev, Nail, Schoepfer, Ralf, Monyer, Hannah, Ruppersberg, J Peter, Gunther, Willy, Seeburg, Peter H, and Sakmann, Bert. Control by asparagine residues of calcium permeability and magnesium blockade in the NMDA receptor. Science, 257(5075):1415–1419, 1992.
- Caminiti, R, Licheri, G, Piccaluga, G, and Pinna, G. X-ray diffraction study of mgcl_2 aqueous solutions. Journal of Applied Crystallography, 12(1):34–38, 1979.
- Case, DA, Darden, TA, Cheatham III, TE, Simmerling, CL, Wang, J, Duke, RE, Luo, R, Walker, RC, Zhang, W, Merz, KM, et al. Amber 12. University of California, San Francisco, 2012.

- Chipot, Christophe and Pohorille, Andrew. Free energy calculations: theory and applications in chemistry and biology, volume 86. Springer, 2nd edition, 2007.
- Cooke, SF and Bliss, TVP. Plasticity in the human central nervous system. Brain, 129(7):1659–1673, 2006.
- Cornell, Wendy D, Cieplak, Piotr, Bayly, Christopher I, Gould, Ian R, Merz, Kenneth M, Ferguson, David M, Spellmeyer, David C, Fox, Thomas, Caldwell, James W, and Kollman, Peter A. A second generation force field for the simulation of proteins, nucleic acids, and organic molecules. Journal of the American Chemical Society, 117(19):5179–5197, 1995.
- Corry, Ben. Understanding ion channel selectivity and gating and their role in cellular signalling. Molecular Biosystems, 2(11):527–535, 2006.
- Cowan, W Maxwell, Südhof, Thomas C, and Stevens, Charles F. Synapses. JHU Press, 2001.
- Curtis, DoR, Phillis, JW, and Watkins, JC. The chemical excitation of spinal neurones by certain acidic amino acids. The Journal of physiology, 150(3): 656–682, 1960.
- Curtis, DR, Phillis, JW, and Watkins, JC. Chemical excitation of spinal neurones. Nature, 183(4661):611–612, 1959.
- Dai, Jian and Zhou, Huan-Xiang. An NMDA receptor gating mechanism developed from md simulations reveals molecular details underlying subunit-specific contributions. Biophysical journal, 104(10):2170–2181, 2013.

- Darden, Tom, York, Darrin, and Pedersen, Lee. Particle mesh ewald: An nlog(n) method for ewald sums in large systems. The Journal of chemical physics, 98(12):10089–10092, 1993.
- Dingledine, Raymond, Borges, Karin, Bowie, Derek, and Traynelis, Stephen F. The glutamate receptor ion channels. Pharmacological reviews, 51(1):7–62, 1999.
- Doyle, Declan A, Cabral, Joao Morais, Pfuetzner, Richard A, Kuo, Anling, Gulbis, Jacqueline M, Cohen, Steven L, Chait, Brian T, and MacKinnon, Roderick. The structure of the potassium channel: molecular basis of K⁺ conduction and selectivity. science, 280(5360):69–77, 1998.
- Doyle, Kristian P, Simon, Roger P, and Stenzel-Poore, Mary P. Mechanisms of ischemic brain damage. Neuropharmacology, 55(3):310–318, 2008.
- Dudev, Todor, Cowan, JA, and Lim, Carmay. Competitive binding in magnesium coordination chemistry: water versus ligands of biological interest. Journal of the American Chemical Society, 121(33):7665–7673, 1999.
- Frisch, M. J., Trucks, G. W., Schlegel, H. B., Scuseria, G. E., Robb, M. A., Cheeseman, J. R., Montgomery, J. A., Jr., Vreven, T., Kudin, K. N., Burant, J. C., Millam, J. M., Iyengar, S. S., Tomasi, J., Barone, V., Mennucci, B., Cossi, M., Scalmani, G., Rega, N., Petersson, G. A., Nakatsuji, H., Hada, M., Ehara, M., Toyota, K., Fukuda, R., Hasegawa, J., Ishida, M., Nakajima, T., Honda, Y., Kitao, O., Nakai, H., Klene, M., Li, X., Knox, J. E., Hratchian, H. P., Cross, J. B., Bakken, V., Adamo, C., Jaramillo, J., Gomperts, R., Stratmann, R. E., Yazyev, O., Austin, A. J., Cammi, R., Pomelli, C., Ochterski, J. W., Ayala, P. Y., Morokuma, K., Voth, G. A., Salvador, P., Dannenberg, J. J., Zakrzewski, V. G., Dapprich, S., Daniels, A. D., Strain, M. C., Farkas, O., Malick, D. K., Rabuck,

A. D., Raghavachari, K., Foresman, J. B., Ortiz, J. V., Cui, Q., Baboul, A. G., Clifford, S., Cioslowski, J., Stefanov, B. B., Liu, G., Liashenko, A., Piskorz, P., Komaromi, I., Martin, R. L., Fox, D. J., Keith, T., Al-Laham, M. A., Peng, C. Y., Nanayakkara, A., Challacombe, M., Gill, P. M. W., Johnson, B., Chen, W., Wong, M. W., Gonzalez, C., and Pople, J. A. Gaussian 03, Revision C.02, 2003. Gaussian, Inc., Wallingford, CT, 2004.

Frisch, M J, Trucks, G W, Schlegel, H B, Scuseria, G E, Robb, M A, Cheeseman, J R, Scalmani, G, Barone, V, Mennucci, B, Petersson, G A, Nakatsuji, H, Caricato, M, Li, X, Hratchian, H P, Izmaylov, A F, Bloino, J, Zheng, G, Sonnenberg, J L, Hada, M, Ehara, M, Toyota, K, Fukuda, R, Hasegawa, J, Ishida, M, Nakajima, T, Honda, Y, Kitao, O, Nakai, H, Vreven, T, Montgomery Jr., J A, Peralta, J E, Ogliaro, F, Bearpark, M, Heyd, J J, Brothers, E, Kudin, K N, Staroverov, V N, Kobayashi, R, Normand, J, Raghavachari, K, Rendell, A, Burant, J C, Iyengar, S S, Tomasi, J, Cossi, M, Rega, N, Millam, J M, Klene, M, Knox, J E, Cross, J B, Bakken, V, Adamo, C, Jaramillo, J, Gomperts, R, Stratmann, R E, Yazyev, O, Austin, A J, Cammi, R, Pomelli, C, Ochterski, J W, Martin, R L, Morokuma, K, Zakrzewski, V G, Voth, G A, Salvador, P, Dannenberg, J J, Dapprich, S, Daniels, A D, Farkas, Ö, Foresman, J B, Ortiz, J V, Cioslowski, J, and Fox, D J. Gaussian~09 {R}evision {A}.1, 2009.

Gilson, Michael K. Theory of electrostatic interactions in macromolecules. Current opinion in structural biology, 5(2):216–223, 1995.

Go, Alan S, Mozaffarian, Dariush, Roger, Véronique L, Benjamin, Emelia J, Berry, Jarett D, Borden, William B, Bravata, Dawn M, Dai, Shifan, Ford, Earl S, Fox, Caroline S, et al. Heart disease and stroke statistics–2013 update: a report from the american heart association. Circulation, 127(1):e6, 2013.

- Gomer, R and Tryson, G. An experimental determination of absolute half-cell emf's and single ion free energies of solvation. The Journal of Chemical Physics, 66(10):4413–4424, 2008.
- Gootz, Andreas W, Williamson, Mark J, Xu, Dong, Poole, Duncan, Le Grand, Scott, and Walker, Ross C. Routine microsecond molecular dynamics simulations with amber on gpus. 1. generalized born. Journal of chemical theory and computation, 8(5):1542–1555, 2012.
- Grossfield, Alan. Wham: the weighted histogram analysis method. Version 2.02 Downloaded at <http://membrane.urmc.rochester.edu/content/wham>, 2012.
- Hardingham, Giles E. Coupling of the NMDA receptor to neuroprotective and neurodestructive events. Biochemical Society Transactions, 37(Pt 6):1147, 2009.
- Helm, L and Merbach, AE. Water exchange on metal ions: experiments and simulations. Coordination chemistry reviews, 187(1):151–181, 1999.
- Helm, Lothar and Merbach, André E. Inorganic and bioinorganic solvent exchange mechanisms. Chemical reviews, 105(6):1923–1960, 2005.
- Hille, Bertil. Ion channels of excitable membranes, volume 507. Sinauer Sunderland, MA, 2001.
- Hoyte, L, Barber, PA, Buchan, AM, and Hill, MD. The rise and fall of NMDA antagonists for ischemic stroke. Current molecular medicine, 4(2):131–136, 2004.
- Ikeda, Takashi, Boero, Mauro, and Terakura, Kiyoyuki. Hydration properties of magnesium and calcium ions from constrained first principles molecular dynamics. The Journal of chemical physics, 127(7):074503, 2007.

- Janardhan, Vallabh and Qureshi, Adnan I. Mechanisms of ischemic brain injury. Current cardiology reports, 6(2):117–123, 2004.
- Javitt, DC. Glutamate as a therapeutic target in psychiatric disorders. Molecular psychiatry, 9(11):984–997, 2004.
- Jiao, Dian, Golubkov, Pavel A, Darden, Thomas A, and Ren, Pengyu. Calculation of protein–ligand binding free energy by using a polarizable potential. Proceedings of the National Academy of Sciences, 105(17):6290–6295, 2008.
- Jones, Kevin S, VanDongen, Hendrika MA, and VanDongen, Antonius MJ. The NMDA receptor M₃ segment is a conserved transduction element coupling ligand binding to channel opening. The Journal of neuroscience, 22(6):2044–2053, 2002.
- Jorgensen, William L and Tirado-Rives, Julian. The opls [optimized potentials for liquid simulations] potential functions for proteins, energy minimizations for crystals of cyclic peptides and crambin. Journal of the American Chemical Society, 110(6):1657–1666, 1988.
- Jorgensen, William L, Chandrasekhar, Jayaraman, Madura, Jeffry D, Impey, Roger W, and Klein, Michael L. Comparison of simple potential functions for simulating liquid water. The Journal of chemical physics, 79(2):926–935, 1983.
- Káradóttir, Ragnhildur, Cavelier, Pauline, Bergersen, Linda H, and Attwell, David. NMDA receptors are expressed in oligodendrocytes and activated in ischaemia. Nature, 438(7071):1162–1166, 2005.
- Kästner, Johannes. Umbrella sampling. Wiley Interdisciplinary Reviews: Computational Molecular Science, 1(6):932–942, 2011.

- Katz, Amy Kaufman, Glusker, Jenny P, Beebe, Scott A, and Bock, Charles W. Calcium ion coordination: a comparison with that of beryllium, magnesium, and zinc. Journal of the American Chemical Society, 118(24):5752–5763, 1996.
- Kemp, John A and McKernan, Ruth M. NMDA receptor pathways as drug targets. Nature neuroscience, 5:1039–1042, 2002.
- Kiss, Janos P, Szasz, Bernadett K, Fodor, László, Mike, Arpad, Lenkey, Nora, Kurkó, Dalma, Nagy, József, and Vizi, E Sylvester. GluN2B-containing NMDA receptors as possible targets for the neuroprotective and antidepressant effects of fluoxetine. Neurochemistry international, 60(2):170–176, 2012.
- Kohda, Kazuhisa, Wang, Ying, and Yuzaki, Michisuke. Mutation of a glutamate receptor motif reveals its role in gating and $\delta 2$ receptor channel properties. Nature neuroscience, 3(4):315–322, 2000.
- Kollman, Peter. Free energy calculations: applications to chemical and biochemical phenomena. Chemical Reviews, 93(7):2395–2417, 1993.
- Kukul, Andreas. Lipid models for united-atom molecular dynamics simulations of proteins. Journal of Chemical Theory and Computation, 5(3):615–626, 2009.
- Kullmann, DM, Asztely, F, and Walker, MC. The role of mammalian ionotropic receptors in synaptic plasticity: Ltp, ltd and epilepsy. Cellular and Molecular Life Sciences CMLS, 57(11):1551–1561, 2000.
- Kumar, Janesh and Mayer, Mark L. Functional insights from glutamate receptor ion channel structures. Annual review of physiology, 75:313–337, 2013.
- Kumar, Shankar, Rosenberg, John M, Bouzida, Djamel, Swendsen, Robert H, and Kollman, Peter A. The weighted histogram analysis method for free-

- energy calculations on biomolecules. i. the method. Journal of computational chemistry, 13(8):1011–1021, 1992.
- Kumar, Shankar, Rosenberg, John M, Bouzida, Djamel, Swendsen, Robert H, and Kollman, Peter A. Multidimensional free-energy calculations using the weighted histogram analysis method. Journal of Computational Chemistry, 16(11):1339–1350, 1995.
- Kuner, Thomas, Wollmuth, Lonnie P, Karlin, Arthur, Seeburg, Peter H, and Sakmann, Bert. Structure of the NMDA receptor channel M2 segment inferred from the accessibility of substituted cysteines. Neuron, 17(2):343–352, 1996.
- Kuner, Thomas, Seeburg, Peter H, and Robert Guy, H. A common architecture for K^{+} channels and ionotropic glutamate receptors? Trends in neurosciences, 26(1):27–32, 2003.
- Kupper, JURGEN, Ascher, Philippe, and Neyton, Jacques. Probing the pore region of recombinant n-methyl-d-aspartate channels using external and internal magnesium block. Proceedings of the National Academy of Sciences, 93(16):8648–8653, 1996.
- Kupper, Jürgen, Ascher, Philippe, and Neyton, Jacques. Internal Mg^{2+} block of recombinant NMDA channels mutated within the selectivity filter and expressed in xenopus oocytes. The Journal of physiology, 507(1):1–12, 1998.
- Kurnikov, Igor. HARLEM (HAMiltonians to Research Large Molecules). Journal of Chemical Physics, 1999.
- Langford, Cooper H and Gray, Harry B. Ligand substitution processes. WA Benjamin, Inc., 1965.

- Leach, Andrew R. Molecular modelling: principles and applications. Pearson Education, 2001.
- Li, Da-Wei and Brüschweiler, Rafael. Nmr-based protein potentials. Angewandte Chemie, 122(38):6930–6932, 2010.
- Lightstone, Felice C, Schwegler, Eric, Hood, Randolph Q, Gygi, François, and Galli, Giulia. A first principles molecular dynamics simulation of the hydrated magnesium ion. Chemical Physics Letters, 343(5):549–555, 2001.
- Lindorff-Larsen, Kresten, Piana, Stefano, Palmo, Kim, Maragakis, Paul, Klepeis, John L, Dror, Ron O, and Shaw, David E. Improved side-chain torsion potentials for the amber ff99sb protein force field. Proteins: Structure, Function, and Bioinformatics, 78(8):1950–1958, 2010.
- MacKerel Jr., A D, Brooks III, C L, Nilsson, L, Roux, B, Won, Y, and Karplus, M. CHARMM: The Energy Function and Its Parameterization with an Overview of the Program. 1:271–277, 1998.
- Malenka, Robert C and Nicoll, Roger A. Long-term potentiation—a decade of progress? Science, 285(5435):1870–1874, 1999.
- Mamonov, Artem B. Modeling ion and water permeation through narrow biological channels. PhD thesis, University of Pittsburgh, 2006.
- Mamonova, Tatyana and Kurnikova, Maria. Structure and energetics of channel-forming protein-polysaccharide complexes inferred via computational statistical thermodynamics. The Journal of Physical Chemistry B, 110(49):25091–25100, 2006.

- Marcus, Yizhak. Thermodynamics of solvation of ions. part 5. gibbs free energy of hydration at 298.15 k. Journal of the Chemical Society, Faraday Transactions, 87(18):2995–2999, 1991.
- Marcus, Yizhak. The Properties of Solvents. Wiley, 1998.
- Micu, I, Jiang, Q, Coderre, E, Ridsdale, A, Zhang, L, Woulfe, J, Yin, X, Trapp, BD, McRory, JE, Rehak, R, et al. NMDA receptors mediate calcium accumulation in myelin during chemical ischaemia. Nature, 439(7079):988–992, 2006.
- Mullins, LJ. The penetration of some cations into muscle. The Journal of general physiology, 42(4):817–829, 1959.
- Murthy, Swetha E, Shogan, Tamer, Page, Jessica C, Kasperek, Eileen M, and Popescu, Gabriela K. Probing the activation sequence of NMDA receptors with lurcher mutations. The Journal of general physiology, 140(3):267–277, 2012.
- Neely, James and Connick, Robert. Rate of water exchange from hydrated magnesium ion. Journal of the American Chemical Society, 92(11):3476–3478, 1970.
- NIA. National Institute on Aging: Leading the Federal Effort on Aging Research. [\url{http://www.nia.nih.gov/Alzheimers/AlzheimersInformation/Treatment/}](http://www.nia.nih.gov/Alzheimers/AlzheimersInformation/Treatment/), 2011.
- Nowak, L_, Bregestovski, P, Ascher, P, Herbet, A, and Prochiantz, Aa. Magnesium gates glutamate-activated channels in mouse central neurones. Nature, 1984.

- Ohtaki, Hitoshi and Radnai, Tamas. Structure and dynamics of hydrated ions. Chemical Reviews, 93(3):1157–1204, 1993.
- Panchenko, Victor A, Glasser, Carla R, and Mayer, Mark L. Structural similarities between glutamate receptor channels and K^+ channels examined by scanning mutagenesis. The Journal of general physiology, 117(4):345–360, 2001.
- Paoletti, Pierre and Neyton, Jacques. NMDA receptor subunits: function and pharmacology. Current opinion in pharmacology, 7(1):39–47, 2007.
- Paul, Ian A and Skolnick, Phil. Glutamate and depression. Annals of the New York Academy of Sciences, 1003(1):250–272, 2003.
- Pavlov, Maria, Siegbahn, Per EM, and Sandström, Magnus. Hydration of beryllium, magnesium, calcium, and zinc ions using density functional theory. The Journal of Physical Chemistry A, 102(1):219–228, 1998.
- Premkumar, Louis S and Auerbach, Anthony. Identification of a high affinity divalent cation binding site near the entrance of the NMDA receptor channel. Neuron, 16(4):869–880, 1996.
- Premkumar, Louis S, Qin, Feng, and Auerbach, Anthony. Subconductance states of a mutant NMDA receptor channel kinetics, calcium, and voltage dependence. The Journal of general physiology, 109(2):181–189, 1997.
- Rao, J Srinivasa, Dinadayalane, TC, Leszczynski, Jerzy, and Sastry, G Narahari. Comprehensive study on the solvation of mono- and divalent metal cations: Li^+ , Na^+ , K^+ , Be^{2+} , Mg^{2+} and Ca^{2+} . The Journal of Physical Chemistry A, 112(50):12944–12953, 2008.

- Retchless, Beth Siegler, Gao, Wei, and Johnson, Jon W. A single GluN2 subunit residue controls NMDA receptor channel properties via intersubunit interaction. Nature neuroscience, 15(3):406–413, 2012.
- Salomon-Ferrer, Romelia, Gootz, Andreas W, Poole, Duncan, Le Grand, Scott, and Walker, Ross C. Routine microsecond molecular dynamics simulations with amber on GPUs. 2. explicit solvent particle mesh ewald. Journal of Chemical Theory and Computation, 9(9):3878–3888, 2013.
- Salter, Michael G and Fern, Robert. NMDA receptors are expressed in developing oligodendrocyte processes and mediate injury. Nature, 438(7071):1167–1171, 2005.
- Schmid, Roland, Miah, Arzu M, and Sapunov, Valentin N. A new table of the thermodynamic quantities of ionic hydration: values and some applications (enthalpy–entropy compensation and born radii). Phys. Chem. Chem. Phys., 2(1):97–102, 2000.
- Schwenk, Christian F, Rode, Bernd M, et al. Ab initio qm/mm md simulations of the hydrated ca 2+ ion. Pure and applied chemistry, 76(1):37–47, 2004.
- Shi, Ning, Ye, Sheng, Alam, Amer, Chen, Liping, and Jiang, Youxing. Atomic structure of a Na⁺- and K⁺-conducting channel. Nature, 440(7083):570–574, 2006.
- Sobolevsky, Alexander I, Rosconi, Michael P, and Gouaux, Eric. X-ray structure, symmetry and mechanism of an ampa-subtype glutamate receptor. Nature, 462(7274):745–756, 2009.

- Souaille, Marc and Roux, Benoit. Extension to the weighted histogram analysis method: combining umbrella sampling with free energy calculations. Computer physics communications, 135(1):40–57, 2001.
- Taverna, Franco, Xiong, Zhi-gang, Brandes, Lidia, Roder, John C, Salter, Michael W, and MacDonald, John F. The lurcher mutation of an α -amino-3-hydroxy-5-methyl-4-isoxazolepropionic acid receptor subunit enhances potency of glutamate and converts an antagonist to an agonist. Journal of Biological Chemistry, 275(12):8475–8479, 2000.
- Thomas, Michael, Jayatilaka, Dylan, and Corry, Ben. The predominant role of coordination number in potassium channel selectivity. Biophysical journal, 93(8):2635–2643, 2007.
- Tikhonov, Denis B. Ion channels of glutamate receptors: structural modeling. Molecular membrane biology, 24(2):135–147, 2007.
- Tikhonov, Denis B, Mellor, Jan R, Usherwood, Peter NR, and Magazanik, Lev G. Modeling of the pore domain of the *glur1* channel: Homology with K^+ channel and binding of channel blockers. Biophysical journal, 82(4):1884–1893, 2002.
- Torrie, Glenn M and Valleau, John P. Nonphysical sampling distributions in monte carlo free-energy estimation: Umbrella sampling. Journal of Computational Physics, 23(2):187–199, 1977.
- Traynelis, Stephen F, Wollmuth, Lonnie P, McBain, Chris J, Menniti, Frank S, Vance, Katie M, Ogden, Kevin K, Hansen, Kasper B, Yuan, Hongjie, Myers, Scott J, and Dingledine, Ray. Glutamate receptor ion channels: structure, regulation, and function. Pharmacological reviews, 62(3):405–496, 2010.

- Tuckerman, Mark E. Statistical Mechanics and Molecular Simulations. Oxford University Press, 2008.
- Varma, Sameer and Rempe, Susan B. Tuning ion coordination architectures to enable selective partitioning. Biophysical journal, 93(4):1093–1099, 2007.
- Wang, Junmei, Wang, Wei, Kollman, Peter A, and Case, David A. Antechamber: an accessory software package for molecular mechanical calculations. J. Am. Chem. Soc., 222:U403, 2001.
- Watanabe, Junryo, Beck, Christine, Kuner, Thomas, Premkumar, Louis S, and Wollmuth, Lonnie P. Drpeer: a motif in the extracellular vestibule conferring high Ca^{2+} flux rates in NMDA receptor channels. The Journal of neuroscience, 22(23):10209–10216, 2002.
- Wollmuth, Lonnie P, Kuner, Thomas, and Sakmann, Bert. Intracellular Mg^{2+} interacts with structural determinants of the narrow constriction contributed by the NR1-subunit in the NMDA receptor channel. The Journal of physiology, 506(1):33–52, 1998a.
- Wollmuth, Lonnie P, Kuner, Thomas, and Sakmann, Bert. Adjacent asparagines in the NR2-subunit of the NMDA receptor channel control the voltage-dependent block by extracellular Mg^{2+} . The Journal of physiology, 506(1): 13–32, 1998b.
- Wood, Michael W, VanDongen, HM, and VanDongen, AM. Structural conservation of ion conduction pathways in K channels and glutamate receptors. Proceedings of the National Academy of Sciences, 92(11):4882–4886, 1995.
- Yonkunas, Michael J. Theoretical Investigation of Ionotropic Glutamate Receptors Structure and Function. PhD thesis, pages 1–126, 2010.

- Yu, Haibo, Noskov, Sergei Yu, and Roux, Benoît. Hydration number, topological control, and ion selectivity. The Journal of Physical Chemistry B, 113(25): 8725–8730, 2009.
- Yuan, Hongjie, Erreger, Kevin, Dravid, Shashank M, and Traynelis, Stephen F. Conserved structural and functional control of n-methyl-d-aspartate receptor gating by transmembrane domain M₃. Journal of Biological Chemistry, 280(33):29708–29716, 2005.
- Zarei, Masoud M and Dani, John A. Ionic permeability characteristics of the n-methyl-d-aspartate receptor channel. The Journal of general physiology, 103(2):231–248, 1994.
- Zuo, Jian, De Jager, Philip L, Takahashi, Kanji A, Jiang, Weining, Linden, David J, and Heintz, Nathaniel. Neurodegeneration in lurcher mice caused by mutation in $\delta 2$ glutamate receptor gene. Nature, 388(6644):769–773, 1997.